

# On the reduction of nonlinear parameters in the eXtended Pom-Pom differential constitutive model<sup>1</sup>

RADEK PIVOKONSKY<sup>2,4</sup>, PETR FILIP<sup>2</sup>, GRIGORII V. PYSHNOGRAI<sup>3</sup>

**Abstract.** An application of differential constitutive models enables a prediction of rheological characteristics of polymer materials. Apart from two linear parameters (relaxation time and modulus) common for all models, a number of adjustable (non-linear) parameters in the individual constitutive models differ. At present for materials exhibiting strain hardening (sudden increase of elongational viscosity) this number attains two or more. This causes that a total number of all parameters per all modes is not moderate and any reduction may contribute to a non-negligible simplification of applied numerical methods and unambiguity of the nonlinear parameters. The aim of this contribution is to compare efficiency of the proposed modified eXtended Pom-Pom model (one nonlinear parameter only per mode) with the eXtended Pom-Pom model (nominally three parameters) and the modified Leonov model (two parameters). In spite of one nonlinear parameter only, it is shown very good efficiency of the modified XPP model using three different low-density polyethylene materials.

**Key words.** Modified XPP model, XPP model, modified Leonov model, shear flow, elongational flow.

## 1. Introduction

The basic approach in modelling rheological characteristics started in the 20s' of the last century and was based on empirical prediction of—usually—shear viscosity in dependence on shear rate or shear stress (see, e.g., Macosko [1]). The proposed models exhibit simple algebraic forms, moderate number of adjustable parameters and relatively good efficiency for a description of the measured data. Formerly,

---

<sup>1</sup>The authors wish to acknowledge the Grant Agency CR for the financial support of Grant Project No. 17-26808S and the Institutional Research Plan RVO 67985874.

<sup>2</sup>Institute of Hydrodynamics, Czech Academy of Sciences, Prague 166 12, Czech Republic

<sup>3</sup>Faculty of Mathematics and Information Technologies, Altai State University, Barnaul, 656049, Russia

<sup>4</sup>Corresponding author; e-mail: pivokonsky@ih.cas.cz

there were oriented to viscous and viscoplastic materials only. Singularity appearing in the empirical constitutive equations relating shear stress and shear rates was consecutively eliminated in the 80s' (Bercovier and Engelman [2], Lipscomb and Denn [3], Papanastasiou [4]). Generally speaking, a number of adjustable parameters did not exceed five. There were also discussed the differences between viscosity related to shear rate or shear stress (Lomellini and Ferri [5]). The attention was recently also paid to elastoviscoplastic materials (de Souza Mendes and Thompson [6], Saramito [7]). Empirical modelling of nonmonotonous behaviour of viscosity was analysed as well (David and Filip [8], David et al. [9], Galindo-Rosales et al. [10, 11]). There were also consecutively proposed phenomenological models containing an equivalent number of adjustable parameters, however based on more physical reasoning.

Applicability of empirical and/or phenomenological models fails if a prediction of complex rheological behaviour (shear and elongational viscosities, first and second normal stress differences) is necessary. In other words, if there is a demand for simultaneous prediction of more rheological characteristics both in steady and in transient regimes. In this case a usage of differential and/or integral constitutive equations is inevitable.

One of the possibilities how to complete balance equations in the description of polymer melt flow behaviour is represented by so called differential constitutive equations that are usually derived from two distinct approaches known as the network theory and the reptation theory (Larson [12], Doi and Edwards [13], Dealy and Larson [14]). The individual equations differ in the terms they are composed of and thus in preferring qualities the terms represent. Initially the proposed models involved the upper-convected  $\overset{\nabla}{\boldsymbol{\tau}}$  and lower-convected  $\overset{\Delta}{\boldsymbol{\tau}}$  derivatives defined as

$$\begin{aligned}\overset{\nabla}{\boldsymbol{\tau}} &= \frac{\partial \boldsymbol{\tau}}{\partial t} - (\nabla \mathbf{v})^T \boldsymbol{\tau} - \boldsymbol{\tau} (\nabla \mathbf{v}), \\ \overset{\Delta}{\boldsymbol{\tau}} &= \frac{\partial \boldsymbol{\tau}}{\partial t} + (\nabla \mathbf{v}) \boldsymbol{\tau} + \boldsymbol{\tau} (\nabla \mathbf{v})^T,\end{aligned}\tag{1}$$

where  $\mathbf{v}$  is the velocity vector,  $\boldsymbol{\tau}$  is the stress tensor,  $t$  represents time and  $\partial/\partial t$  is the substantial time derivative. Later on the introduced Gordon-Schowalter derivative with non-affine motion parameter  $\xi \in [0, 2]$

$$\overset{\diamond}{\boldsymbol{\tau}} = \left(1 - \frac{\xi}{2}\right) \overset{\nabla}{\boldsymbol{\tau}} + \frac{\xi}{2} \overset{\Delta}{\boldsymbol{\tau}}\tag{2}$$

characterizes the non-affine motion through the slip relating the motion of the network junctions to the motion of the continuum. This derivative overcomes rigidity of some models in evaluating shear thinning.

The importance of the individual terms is also influenced (weighted) by the presence of parameters. These parameters can be divided into two groups: two linear parameters (relaxation time  $\lambda_i$  and shear modulus  $G_i$  generated by Maxwell evaluation and common for all differential constitutive models, and nonlinear parameters

which number varies from one to four in dependence on the used model. The problem is that the total number of parameters (3–6) is possible to apply only to a group of topologically close macromolecules. In practice, due to polydispersity of commercial polymer material (varying from charge to charge) it is necessary to describe simultaneously more groups each of them representing so called mode. Hence, more modes related to different relaxation times and moduli causes substantial increase in a number of parameters. This increase can cause a possibility of mutual influence of the individual parameters between modes during numerical evaluation. Moreover, numerical procedure is much more complex and time consuming. In Maxwell evaluation, an effort to fit theoretical curves to the measured data significantly dominates the physical nature of the whole problem. The resulting modes are characterized by relaxation times and shear moduli mutually differing by many orders and thus less compatible with the real situation. Consequently,  $n$ -tuples of the nonlinear parameters correspond to the individual partially incongruous modes subject rather than to the numerical fitting. It is possible to simplify this process by the reduction of a number of nonlinear adjustable parameters per mode. Such a reduction exhibits two benefits: simplification of the whole numerical procedure and minimization of possible ambiguity of the nonlinear parameters. On the other hand, it is necessary to check whether this simplification does not reflect a worse prediction of rheological characterization. Therefore, an acceptability of the simplified (exhibiting a reduced number of nonlinear parameters) models should be proved across a sufficiently large palette of distinct materials. The acceptability means an adequate prediction of the rheological properties fully comparable with the existing multi-parameter constitutive models.

This stimulates the aim of this contribution. For three different low-density polyethylene materials (Lupolen 1840 - Zatloukal [15], Bralen RB0323 - Pivokonsky et al. [16] and LDPE1 - Stadler et al. [17]) there is compared an efficiency of 3-parameter (only one nonlinear parameter) modified eXtended Pom-Pom model (Pivokonsky and Filip [18]) with the original eXtended Pom-Pom model (Verbeeten et al. [19], where 4 independent parameters are considered) and the 4-parameter modified Leonov model (Zatloukal [15]). It is necessary to remind that—in contrast to the modified XPP model—the original one enables also prediction of the second normal stress difference. The results indicate very good applicability of the modified XPP model for which a number of the nonlinear parameters per mode is absolutely minimized.

## 2. The original and modified XPP models, modified Leonov model

Many differential constitutive equations (as for instance the Upper convective model (UCM), Phan-Tien - Tanner model (PTT), Giesekus model, eXtended Pom-Pom model, Leonov model) suppose the following relation between extra stress tensor  $\boldsymbol{\tau}$  and symmetrical conformation tensor  $\boldsymbol{c}$

$$\boldsymbol{\tau} = G(\boldsymbol{c} - \boldsymbol{I}) , \quad (3)$$

where  $G$  represents the elastic shear modulus and  $\mathbf{I}$  denotes the unit tensor.

In general, the evolution equation of the models can be written in the form

$$\frac{d\mathbf{c}}{dt} - \nabla\mathbf{v} \cdot \mathbf{c} - \mathbf{c} \cdot \nabla\mathbf{v}^T - \frac{\xi}{2}(\dot{\boldsymbol{\gamma}} \cdot \mathbf{c} + \mathbf{c} \cdot \dot{\boldsymbol{\gamma}}) + \frac{1}{\lambda}\mathbf{H}(\mathbf{c}) = 0, \quad (4)$$

where  $\mathbf{v}$  is the velocity,  $\dot{\boldsymbol{\gamma}}$  is the rate of deformation tensor ( $\nabla\mathbf{v} + \nabla\mathbf{v}^T$ ),  $\lambda$  is the relaxation time, and  $\mathbf{H}(\mathbf{c})$  is the dissipative term depending on the conformation tensor  $\mathbf{c}$ . The parameter  $\xi$  is the non-affine motion parameter attaining the limiting values 0 and 2, for which the conformation tensor represents contravariant (upper convected derivative) and covariant (lower convected derivative) forms, respectively. For many polymer systems the parameter  $\xi$  takes the zero value.

The following two reasons lead to a choice  $\xi = 0$ . First, to reduce a number of nonlinear parameters, and second, non-zero value of the parameter  $\xi$  causes unphysical oscillations in transient shear characteristics at high shear rates (see Figs. 8 and 9 in Pivokonsky et al. [16]). On the other hand, a non-zero value of  $\xi$  significantly contributes to more pronounced shear thinning (see Fig. 3 in [16]). The specific forms of the dissipative terms  $\mathbf{H}(\mathbf{c})$  for all three models under consideration (the XPP, modified XPP and modified Leonov differential constitutive models supposing  $\xi = 0$ ) are summarized in Table 1.

Table 1. The dissipative term  $\mathbf{H}(\mathbf{c})$  for the XPP, modified XPP and modified Leonov differential constitutive models (supposing  $\xi = 0$ )

Model	Dissipative term $\mathbf{H}(\mathbf{c})$	Number of parameters (including linear $\lambda, G$ )	Nonlinear parameters
XPP [19]	$\alpha(\mathbf{c} - \mathbf{I})^2 + F_{\text{XPP}}\mathbf{c} - \mathbf{I}$	5	$\lambda_s, q, \alpha$
modified XPP [18]	$F_{\text{mXPP}}\mathbf{c} - \mathbf{I}$	3	$\beta$
modified Leonov [15]	$\frac{b}{2} \left( \mathbf{c}^2 - \frac{\text{tr}\mathbf{c} - \text{tr}\mathbf{c}^{-1}}{3} \mathbf{c} - \mathbf{I} \right)$	4	$\zeta, \nu$

Here,

$$F_{\text{XPP}} = 2 \frac{\lambda}{\lambda_s} \exp \left[ \frac{2}{q} (\Lambda - 1) \right] \left( 1 - \frac{1}{\Lambda} \right) + \frac{1}{\Lambda^2} \left[ 1 - \alpha - \frac{\alpha}{3} \text{tr}(\mathbf{c}^2 - 2\mathbf{c}) \right],$$

$$F_{\text{mXPP}} = \left( 2 - \frac{1}{\sqrt{\Lambda}} \right) \exp [\beta (\Lambda - 1)],$$

$$\Lambda = \sqrt{\frac{\text{tr}\mathbf{c}}{3}},$$

$$b = \exp \left[ -\zeta \sqrt{\text{tr}\mathbf{c} - 3} \right] + \frac{\sinh [\nu(\text{tr}\mathbf{c} - 3)]}{\nu(\text{tr}\mathbf{c} - 3) + 1}.$$

An influence of the reduction of parameters between the XPP and modified XPP

models is presented in Figs. 1 and 2, where the selected one mode courses of the first normal conformation tensor difference and the shear component of conformation tensor are depicted in dependence on the Weissenberg number. This reduction is also beneficial from the viewpoint of a numerical procedure. For the determination of the Maxwell parameters, the least squares method is used. However, the nonlinear parameters were optimized manually. In the case of the modified XPP model, the way to find the optimum parameters is not complicated due to one nonlinear parameter per relaxation time.

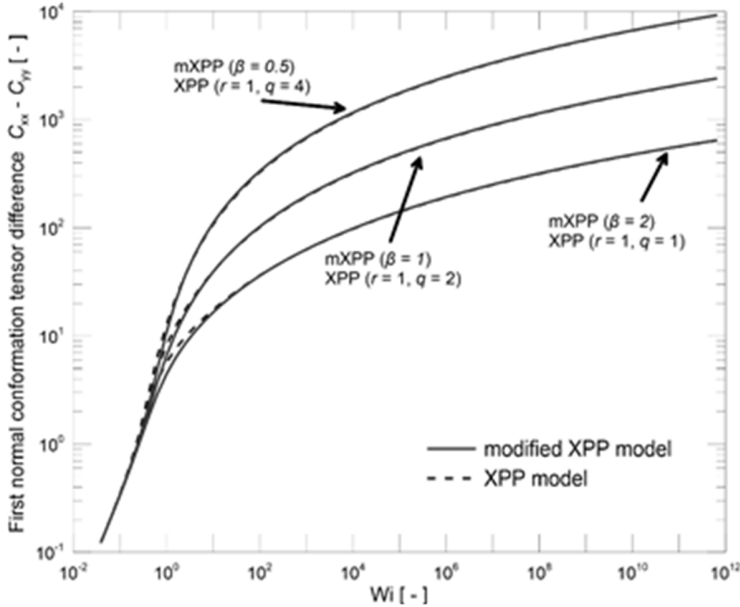


Fig. 1. Comparison of the original XPP and modified XPP models ability to predict first normal difference of conformation tensor  $c$  calculated for uniaxial extensional flow

### 3. Results and discussion

Determination of the parameters appearing in the individual models was based on usage of the MATLAB software, specifically the ode15s variable order multistep solver based on the numerical differentiation formulas was applied. This solver is based on the backward differentiation formulas (also known as Gear's method).

For all three LDPE materials, the Giesekus parameter  $\alpha$  in the XPP model has been taken as the ratio of  $0.1/q$ , i.e., the nominal number of five parameters in the XPP model was reduced by this choice to four only (more details on the reasons for choosing this value for  $\alpha$  are introduced in Verbeeten et al. [19]).

The data of three materials introduced below are taken as presented in the respective references. Preference of any subregions (correlated e.g. with respect to

long time and high rates tending to appearance of slip or edge fracture) is beyond the scope of this contribution.

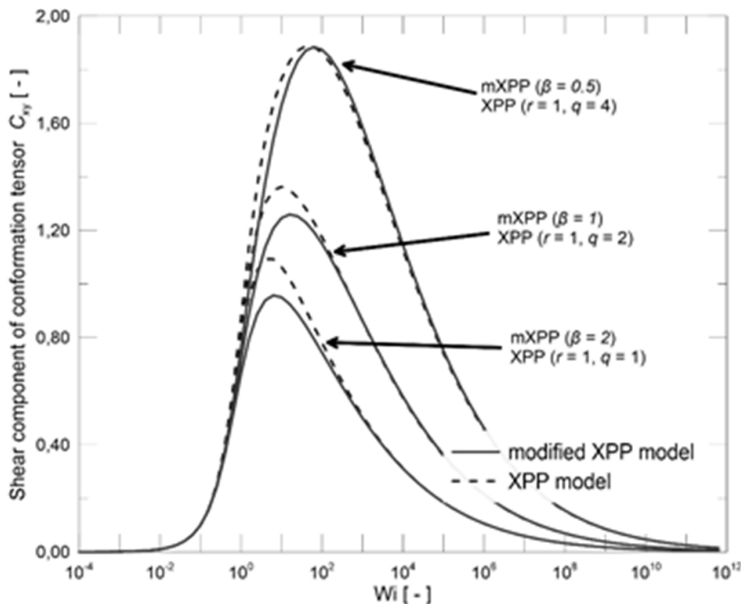


Fig. 2. Comparison of the original XPP and modified XPP models ability to predict shear component of conformation tensor  $c$  calculated for shear flow

### 3.1. LDPE material: Basell Lupolen 1840

The experimental data for LDPE Lupolen 1840 (Zatloukal [15]) was applied. The nonlinear parameters of the modified ( $\beta$ ) and original ( $r = \lambda/\lambda_s$  and  $q$ ) XPP models and the modified ( $\zeta$  and  $\nu$ ) Leonov model have been estimated based on fitting the steady uniaxial extensional viscosity. As mentioned above, the Giesekus parameter  $\alpha$  in the XPP model is set to  $0.1/q$ . The estimated values of the models' parameters are summarized in Table 2. A non-systematic change of the nonlinear model parameters for the XPP and modified XPP models (mode 6) and for the modified Leonov model (mode 5) is caused by an abrupt change of curvature (dominating those for other two materials) of uniaxial extensional viscosity for the respective values of extensional rate. As can be seen from Fig. 3, all three models fit very well in both the steady uniaxial extensional viscosity and the shear viscosity equivalently; however, spurious oscillations are apparent as an accompanying attribute of the modified Leonov model. The same is valid for a prediction of the first normal stress coefficient in steady state (see Fig. 4).

Table 2. Relaxation spectrum and estimated values of the parameters of the original XPP, modified XPP and modified Leonov models for LDPE Basell Lupolen 1840 at 180 °C

<i>i</i>	Maxwell parameters		modified XPP	XPP			modified Leonov	
	$\lambda$ (s)	$G$ (Pa)		$\beta$ (-)	$\frac{\lambda}{\lambda_s}$ (-)	$q$ (-)	$\alpha = \frac{1}{q}$ (-)	$\zeta$ (-)
1	0.0018	108260	1.0	2.0	1	0.1	0	0.2
2	0.0073	28028.6	1.2	3.0	1	0.1	0	0.2
3	0.0295	23336.4	1.5	4.0	1	0.1	0	0.2
4	0.1196	11290.2	1.8	5.0	1	0.1	0.05	0.05
5	0.4841	5856.42	2.0	6.0	2	0.05	0.7	0.012
6	1.9592	2322.13	0.32	1.35	6	0.0167	0.2	0.01
7	7.9291	695.625	1.5	5.0	7	0.0143	0	0.01
8	32.091	128.05	4.0	5.0	7	0.0143	0	0.001
9	129.88	0.56853	7.0	6.0	8	0.0125	0	0.001

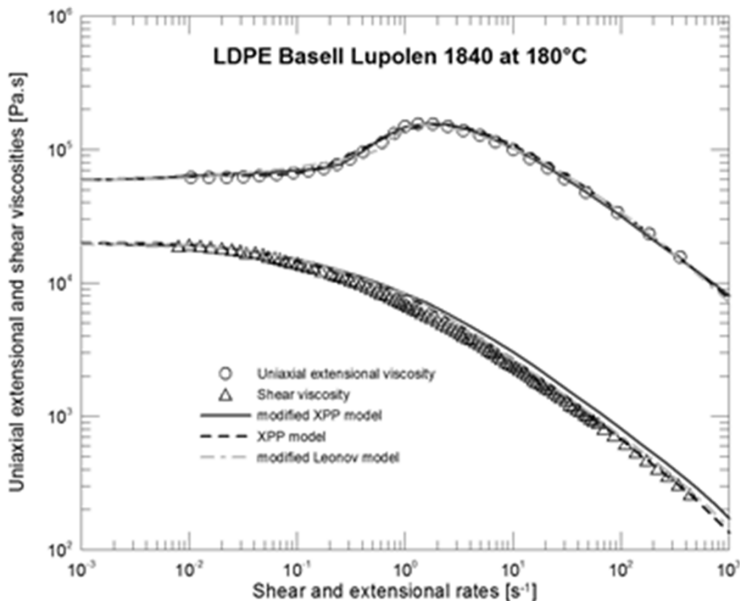


Fig. 3. Comparison between measured steady shear and uniaxial extensional viscosity data and fits/predictions of the original XPP, modified XPP and modified Leonov models for LDPE Lupolen 1840 at 180 °C

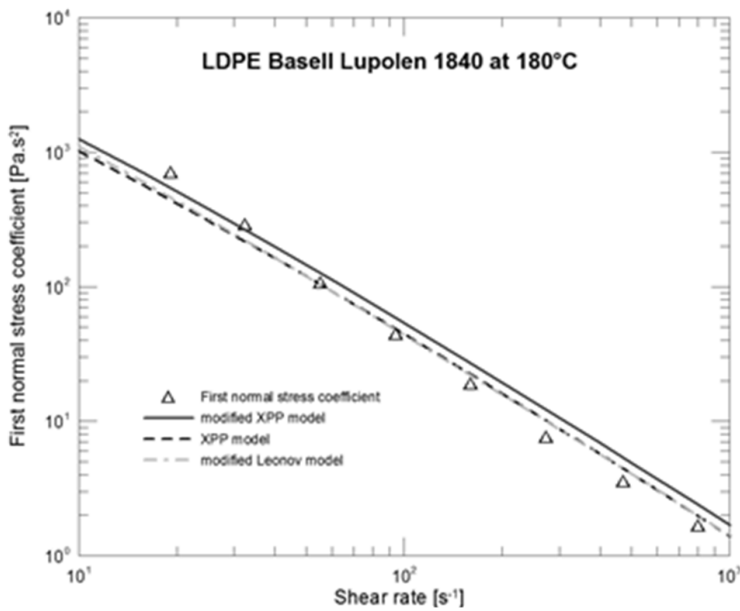


Fig. 4. Comparison between measured steady first normal stress coefficient and fits/predictions of the original XPP, modified XPP and modified Leonov models for LDPE Lupolen 1840 at 180 °C

### 3.2. LDPE material: Bralen RB 0323

The experimental data for LDPE Bralen RB 0323 in Pivokonsky et al. [16] was applied. The corresponding parameters of the models are introduced in Table 3. The steady uniaxial extensional viscosity is fitted by all three models comparably (Fig. 5); however, the modified Leonov model exhibits spurious oscillatory behaviour for lower values of extensional rates. The modified XPP model exhibits stronger shear thinning at lower strain rates compared to the original XPP model, although the steady uniaxial extensional viscosity at that region is fitted equally (Figs. 5 and 6). The best modelling is achieved by the modified Leonov model. The transient uniaxial extensional and shear viscosities, and first normal stress coefficient are shown in Figs. 7–9. The modified XPP model has generally a tendency to exhibit a slightly higher overshoot in the transient shear viscosity in comparison to the XPP model, while the modified Leonov model underpredicts both transient shear viscosity and first normal stress coefficient.

Table 3. Relaxation spectrum and estimated values of the parameters of the original XPP, modified XPP and modified Leonov models for LDPE Bralen RB 0323 at 200 °C

<i>i</i>	Maxwell parameters		modified XPP	XPP			modified Leonov	
	$\lambda$ (s)	$G$ (Pa)		$\beta$ (-)	$\frac{\lambda}{\lambda_s}$ (-)	$q$ (-)	$\alpha = \frac{1}{q}$ (-)	$\zeta$ (-)
1	0.00134	121440	0.7	3.4	1	0.1	0	0.01
2	0.00520	35292.2	0.65	2.8	1	0.1	0	0.01
3	0.02015	33442.9	0.6	2.6	2	0.05	0	0.01
4	0.07804	19480.3	0.55	1.8	3	0.0333	0	0.01
5	0.30230	11923.4	0.43	1.8	5	0.02	0	0.01
6	1.1710	5763.63	0.4	1.3	7	0.0143	0.34	0.0009
7	4.5363	2574.63	0.265	1.3	8	0.0125	0.34	0.0009
8	17.572	800.865	0.255	1.2	9	0.0111	0.33	0.0009
9	68.070	213.412	0.255	1.1	9	0.0111	0.33	0.0009
10	263.68	34.6864	0.25	1.1	9	0.0111	0.325	0.0009

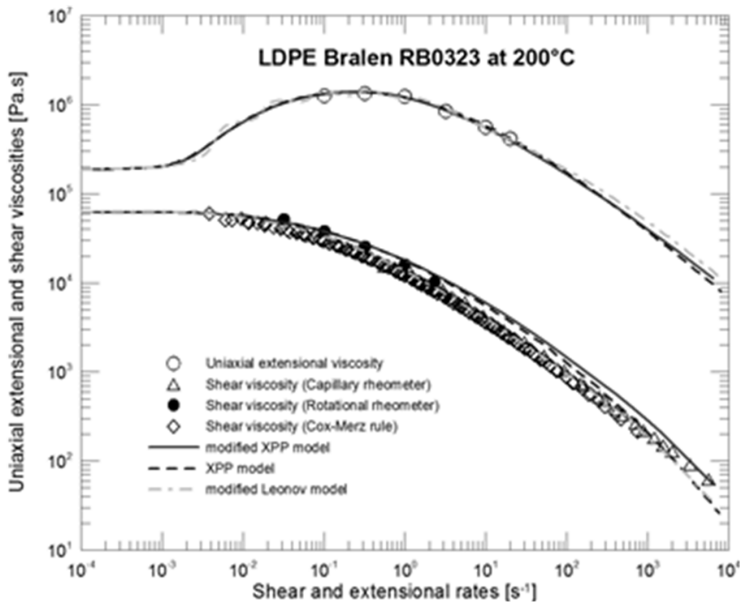


Fig. 5. Comparison between measured steady shear and uniaxial extensional viscosity data and fits/predictions of the original XPP, modified XPP and modified Leonov models for LDPE Bralen RB0323 at 200 °C

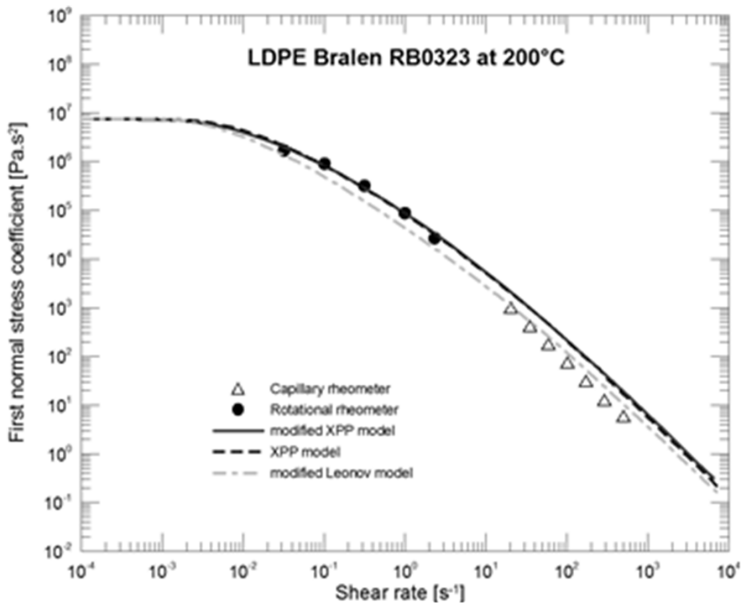


Fig. 6. Comparison between measured steady first normal stress coefficient and fits/predictions of the original XPP, modified XPP and modified Leonov models for LDPE Bralen RB0323 at 200 °C

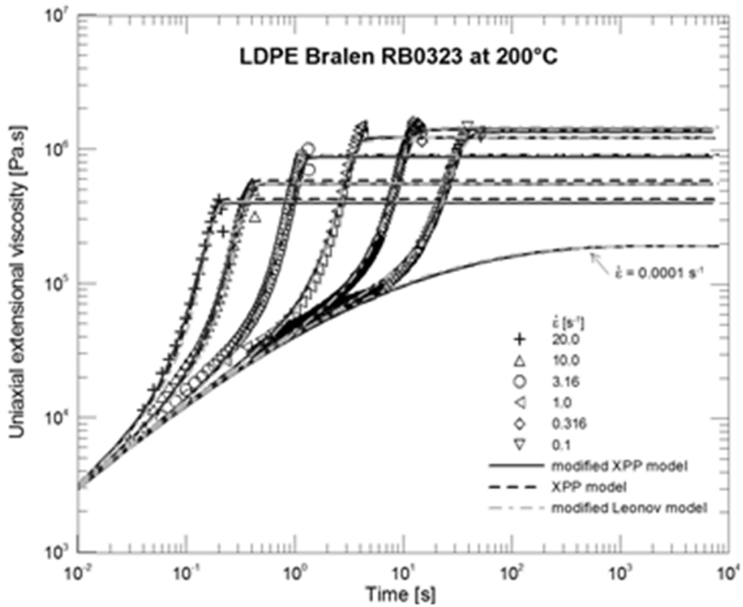


Fig. 7. Comparison between measured transient uniaxial extensional viscosity data and fits/predictions of the original XPP, modified XPP and modified Leonov models for LDPE Bralen RB0323 at 200 °C

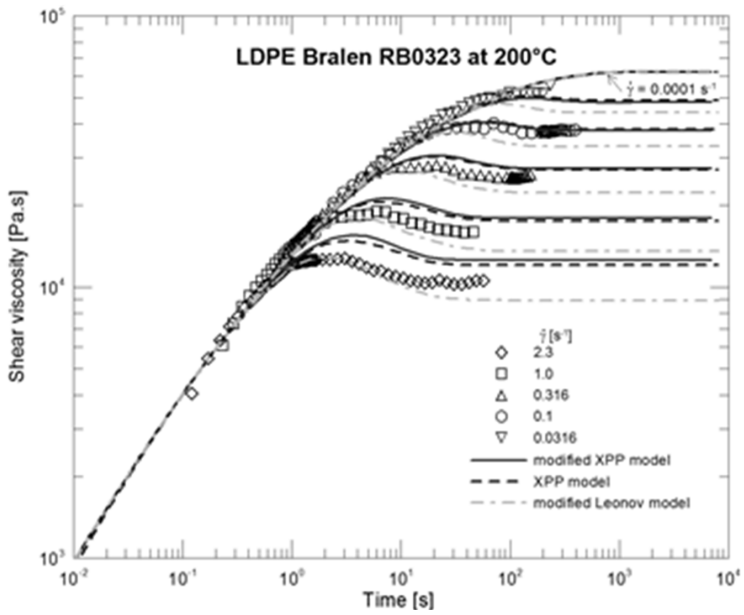


Fig. 8. Comparison between measured transient shear viscosity data and fits/predictions of the original XPP, modified XPP and modified Leonov models for LDPE Bralen RB0323 at 200°C

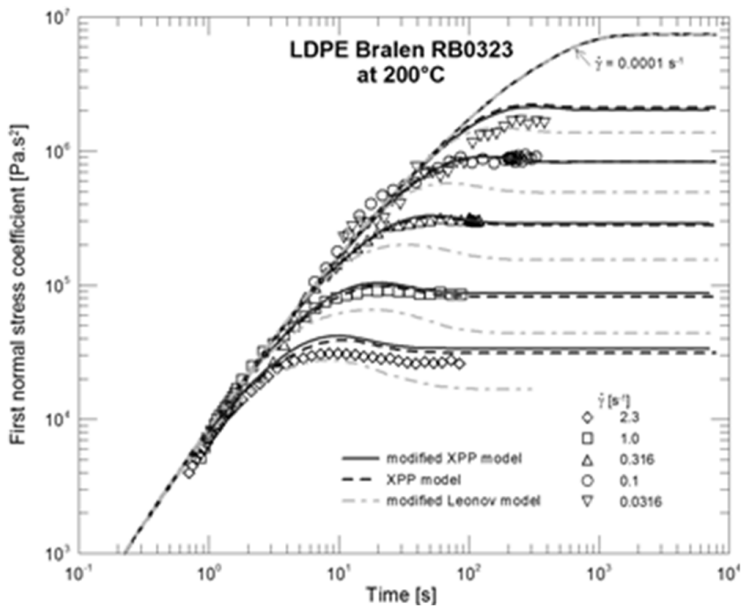


Fig. 9. Comparison between measured transient first normal stress coefficient and fits/predictions of the original XPP, modified XPP and modified Leonov models for LDPE Bralen RB0323 at 200°C

### 3.3. LDPE material: LDPE 1

The last modelled LDPE material was measured in Stadler et al. [17], due to the better figures resolution, the data was taken from Abbasi et al. [20]. The values of the parameters of the individual models are summarized in Table 4.

Table 4. Relaxation spectrum and estimated values of the parameters of the original XPP, modified XPP and modified Leonov models for LDPE 1 at 150 °C

$i$	Maxwell parameters		modified XPP	XPP			modified Leonov	
	$\lambda$ (s)	$G$ (Pa)		$\beta$ (-)	$\frac{\lambda}{\lambda_s}$ (-)	$q$ (-)	$\alpha = \frac{1}{q}$ (-)	$\zeta$ (-)
1	0.00001212	1650000	1.2	3.0	1	0.1	0.001	0.05
2	0.0000768	826000	1.2	2.0	1	0.1	0.001	0.05
3	0.0003911	165000	1.2	1.5	1	0.1	0.001	0.05
4	0.0612	72900	1.2	1.3	1	0.1	0.001	0.05
5	0.9988	21500	1.2	1.2	2	0.05	0.001	0.05
6	8.488	6150	1.2	1.1	2	0.05	0.001	0.4
7	31.73	3160	0.7	1.1	3	0.0333	0.1	1
8	492.7	1040	0.4	1.1	5	0.02	0.47	0.002

The measured uniaxial extensional viscosity at strain rate  $0.001 \text{ s}^{-1}$  is depicted but not taken into the fitting procedure due to the unexpectedly high value (see Fig. 10). This property is fitted well by all three models. The steady shear viscosity is fitted better by the modified XPP model than by the original one. In both steady shear viscosity fits the viscosity characteristics are a little bit curved at high shear rates. The best fitting is exhibited -as in the case of the preceding material- by the modified Leonov model. The transient uniaxial extensional viscosity is fitted by all the models with the same quality (Fig. 11).

## 4. Conclusion

A reduction of nonlinear adjustable parameters in differential constitutive equations exhibits two benefits. First, mutual influence of the parameters is minimized or (as in the case of only one nonlinear parameter) completely eliminated. Second, the whole numerical procedure is substantially simplified which has a positive impact on the application of the models in practice, i.e. in polymer processing. Simultaneously it was shown that a reduction of nonlinear parameters has not to be accompanied with worse prediction of polymer melt flow behaviour. The presented cases document that an application of the modified XPP model involving only one nonlinear adjustable parameter provide a very good prediction within the tolerances

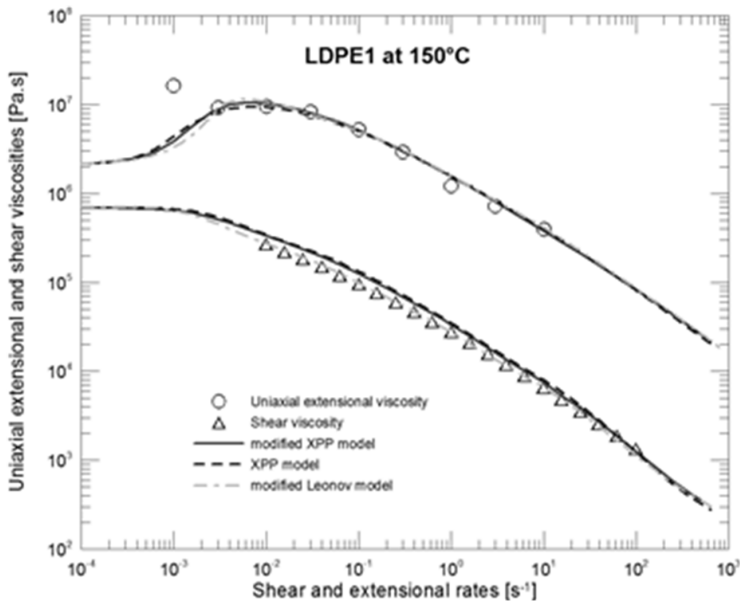


Fig. 10. Comparison between measured steady shear and uniaxial extensional viscosity data and fits/predictions of the original XPP, modified XPP and modified Leonov models for LDPE 1 at 150 °C

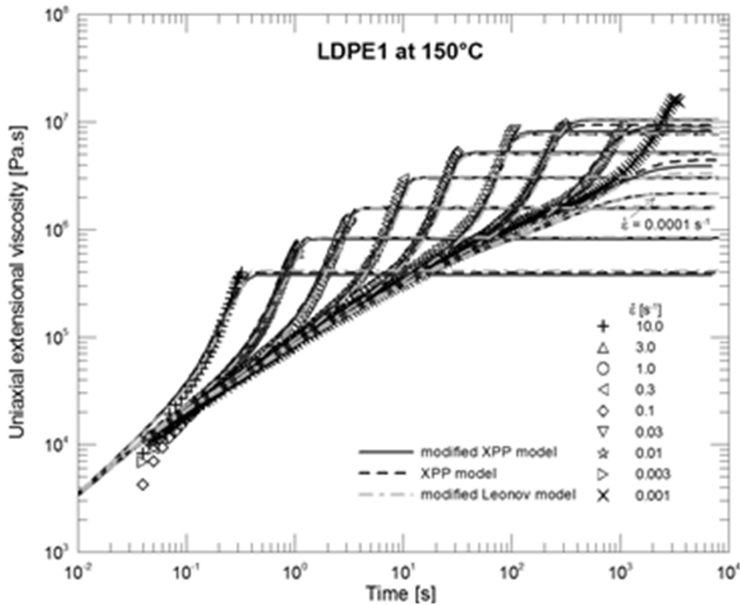


Fig. 11. Comparison between measured transient uniaxial extensional viscosity data and fits/predictions of the original XPP, modified XPP and modified Leonov models for LDPE 1 at 150 °C

given by the measurements of the rheological characteristics and among other things substantially reduces complexity of data processing and computational time.

## References

- [1] C. W. MACOSKO: *Rheology—principles, measurements, and applications*. VCH, New York, USA (1994).
- [2] M. BERCOVIER, M. ENGELMAN: *A finite-element method for incompressible non-Newtonian flows*. *Journal of Computational Physics* 26 (1980), No. 3, 313–326.
- [3] G. G. LIPSCOMB, M. M. DENN: *Flow of Bingham fluids in complex geometries*. *Journal of Non-Newtonian Fluid Mechanics* 14 (1984), 337–346.
- [4] T. C. PAPANASTASIOU: *Flows of materials with yield*. *Journal of Rheology* 31 (1987), No. 5, 385–404.
- [5] P. LOMELLINI, D. FERRI: *Polymer melt rheology versus shear rate or versus shear stress?*. Proc. 13th International Congress on Rheology, 20–25 August 2000, Cambridge, England, UK, Vol. 1, 118–120 (2000).
- [6] P. DE SOUZA MENDES, R. L. THOMPSON: *A critical overview of elasto-viscoplastic thixotropic modeling*. *Journal of Non-Newtonian Fluid Mechanics* 187–188 (2012), 8–15.
- [7] P. SARAMITO: *A new elastoviscoplastic model based on the Herschel–Bulkley viscoplastic model*. *Journal of Non-Newtonian Fluid Mechanics* 158 (2009), Nos. 1–3, 154–161.
- [8] J. DAVID, P. FILIP: *Phenomenological modelling of non-monotonous shear viscosity functions*. *Applied Rheology* 14 (2004), No. 2, 82–88.
- [9] J. DAVID, P. FILIP, A. A. KHARLAMOV: *Empirical modelling of nonmonotonous behaviour of shear viscosity*. *Advances in Materials Science and Engineering* (2013), article ID 658187.
- [10] F. J. GALINDO-ROSALES, F. J. RUBIO-HERNÁNDEZ, A. SEVILLA: *An apparent viscosity function for shear thickening fluids*. *Journal of Non-Newtonian Fluid Mechanics* 166 (2011), Nos. 5–6, 321–325.
- [11] F. J. GALINDO-ROSALES, F. J. RUBIO-HERNÁNDEZ, A. SEVILLA, R. H. EWOLDT: *How Dr. Malcolm M. Cross may have tackled the development of ‘an apparent viscosity function for shear thickening fluids’*. *Journal of Non-Newtonian Fluid Mechanics* 166 (2011), Nos. 23–24, 1421–1424.
- [12] R. G. LARSON: *Constitutive equations for polymer melts and solutions*. Butterworth Publisher, Stoneham, USA (1988).
- [13] M. DOI, S. EDWARDS: *The theory of polymer dynamics*. Oxford University Press, Oxford, UK (1986).
- [14] J. M. DEALY, R. G. LARSON: *Structure and rheology of molten polymers*. Carl Hanser Verlag, Munich, Germany (2006).
- [15] M. ZATLOUKAL: *Differential viscoelastic constitutive equations for polymer melts in steady shear and elongational flows*. *Journal of Non-Newtonian Fluid Mechanics* 113 (2003), Nos. 2–3, 209–227.
- [16] R. PIVOKONSKY, M. ZATLOUKAL, P. FILIP: *On the predictive/fitting capabilities of the advanced differential constitutive equations for branched LDPE melts*. *Journal of Non-Newtonian Fluid Mechanics* 135 (2006), No. 1, 58–67.
- [17] F. J. STADLER, J. KASCHTA, H. MÜNSTEDT, F. BECKER, M. BUBACK: *Influence of molar mass distribution and long-chain branching on strain hardening of low density polyethylene*. *Rheologica Acta* 48 (2009), No. 5, 479–490.
- [18] R. PIVOKONSKY, P. FILIP: *Predictive/fitting capabilities of differential constitutive models for polymer melts—reduction of nonlinear parameters in the eXtended Pom-Pom model*. *Colloid and Polymer Science* 292 (2014), No. 11, 2753–2763.

- [19] W. M. H. VERBEETEN, G. W. M. PETERS, F. P. T. BAAIJENS: *Differential constitutive equations for polymer melts: the extended Pom–Pom model*. *Journal of Rheology* 45 (2001), No. 4, 823–843.
- [20] M. ABBASI, N. G. EBRAHIMI, M. NADALI, M. K. ESFAHANI: *longational viscosity of LDPE with various structures: employing a new evolution equation in MSF theory*. *Rheologica Acta* 51 (2012), No. 2, 163–177.

Received May 15, 2018



# Analysis and identification of ways to improve efficiency of martensitic engines of various schemes

TAMAZ MORCHADZE<sup>1,3</sup>, NUNU RUSADZE<sup>1</sup>,  
ALEKSANDRE SHERMAZANASHVILI<sup>2</sup>

**Abstract.** The principle of operation of a martensitic converter is shown by the authors. The analysis of perspective schemes and designs of working elements of the martensitic converter is given, for optimization of their work with the purpose of obtaining the greatest power. In particular, problems of expediency of application of various variants of working elements are considered: wire, tape, spring. Combined chains with ring and plate spring elements are proposed. An approximate calculation of the torque of a perspective rotational thermomechanical converter is given. There are represented graphically the models of the specimens of martensitic engines tested in operation with a working medium in the form of a spring made of nitinol wire, which have been developed at the Raphiel Dvali Institute of Machines Mechanics. The models are represented as images, and various versions of the perspective recurrent circuits of martensitic converters are described. The essence of the martensitic conversion is described. At the end of this paper, there is proposed a spring-actuated plate element which, when inserted into the working circuit, enables to substantially increase the weight of a working medium, and thereby increase the amount of energy to be converted, i.e., the power.

**Key words.** Martensite, austenite, nitinol, working body, shape memory effect.

## 1. Introduction

The development of natural energy resources is a significant additional source of energy. Special attention in the country should be attached to the existing resources of geothermal waters. Their reserves throughout the world are estimated at up to 10 times all the organic thermal resources taken together.

The total heat delivery capacity of geothermal heat resources in 58 countries of

---

<sup>1</sup>Faculty of Technical Engineering, Akaki Tsereteli State University, 59 Tamara Mepe, Kutaisi, 4600 Georgia

<sup>2</sup>Institute of Machine Mechanics, 0186, Georgia, Tbilisi, Mindeli st. 10

<sup>3</sup>Corresponding author; e-mail: tamazmor@mail.ru

the world is 16.407 megawatts. The development of this resource would save 8.2 million tons of fuel equivalent. Among the countries with geothermal resources, Georgia ranks the seventh.

The examination of the martensitic engines created to date, as heat sources for which there can be applied geothermal waters, waste hot water from industrial enterprises and accumulated heat of solar energy, has shown that in order to implement them, further works are needed to be done, both of a scientific nature and the structural modification, for the purpose of optimizing the heat exchange processes.

As is known, there are many devices for converting thermal energy into mechanical energy. Among them, martensitic energy converters are of great interest, the principle of operation of which is based on the property of some materials exhibiting the effect of shape memory.

## 2. The analysis of previous research

The expected energy deficit, caused by the depletion of the world's resources of fossil energy carriers, predetermines the need to use alternative sources of thermal energy. For this purpose, active research is being conducted in various countries. In order to create variable heat-energy converters, in which this energy is converted into mechanical energy, different types of phase transfer, such as ferroelectric, superconducting, magnetic, martensitic, etc. [1–3], can be used in solid bodies.

Currently, among the above-mentioned phase transitions, the martensitic phase transition is considered to be the most promising, therefore, there is a lot of patents for martensitic thermal engines converting the thermal energy of water into mechanical energy. Only in America, there are more than one hundred patents. It should be noted that the heat engine used in practice has not yet been created. Nevertheless, the creation of martensitic engines remains a very attractive and promising trend [4–11].

The most promising of martensitic engines is the one with a working body of nitinol, which possess the effect of shape "memory".

Alloys with a capability for recoverable plastic deformation with subsequent recovery of the original (prior to deformation) geometry, are known as materials with a "shape memory effect (SME)." They belong to a group of the so-called "smart" functional materials.

A characteristic feature of these alloys is the property of undergoing a thermoplastic martensitic phase transition at a certain critical temperature. Indeed, it is thanks to the martensitic transition that SME arises in them. Thermoplastic martensitic transition is a diffusion-less structural transformation with an athermal shift mechanism of the atomic planes.

Figure 1 illustrates the martensitic phase transformation scheme.

In the high-temperature phase, known as "austenite", the crystalline grid is more symmetrical than in the low-temperature phase, known as "martensite". When passing down by the temperature from the austenite phase to the martensitic phase, the crystalline grid is deformed with the creation of the long plates, the so-called "lamellae". The differently directed lamellae form pairs to minimize stresses in the

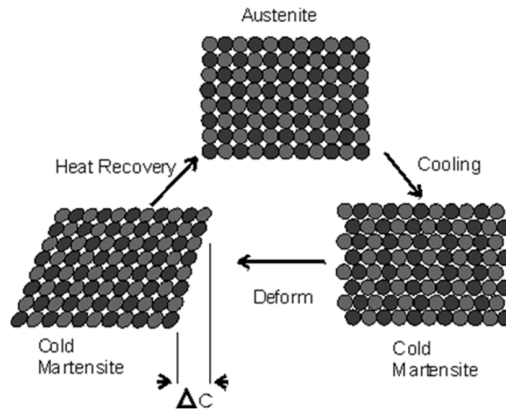


Fig. 1. Martensitic phase transformation scheme

grid.

If we subject a specimen in the martensitic phase to plastic deformation, that is to change its shape, then at a temperature below the transition it can stay in this state as long as desired. However, when it is heated above the transition temperature, when transiting into austenite, it completely recovers its original shape.

Among all materials with SME, the most widely used are alloys based on Ti-Ni, the so-called nitinol. It is characterized by a high degree of the shape memory and a very high ratio of work and volume ( $= \text{force} \times \text{deformation} / \text{volume}$ ). In addition, unlike other known materials with SME, Ti-Ni has good mechanical properties, plasticity and corrosion resistance [12].

### 3. Research methodology and results

Before proceeding to the direct calculation of the parameters of this transmission, it is necessary to consider its conditional kinematic scheme, shown in Fig. 2.

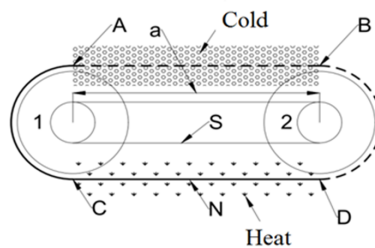


Fig. 2. Martensitic convertor (conventional kinematic scheme)

Two pulleys are shown here: 1 and 2, interconnected by synchronizing or differential transmission S, and also by an additional transmission N, conditionally called "belt transmission". If we heat and cool repeatedly the working medium N and assume that the gear ratios of the synchronizing (S) and the "belt" (N) transmissions

are equal to each other, or equal to 1.00, as shown in Fig. 2, the pulleys 1 and 2 can freely rotate; however, no torque can occur here, because there are no forces that set the system in motion. To create the forces of rotation of pulleys 1 and 2, it is necessary that one of the gears be made of a material with shape memory effect, and also that the ratios of the synchronizing and "belt" transmissions be considered unequal. This can be done according to the scheme (Fig. 3), which is a nitinol engine [11].

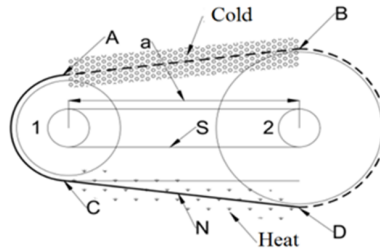


Fig. 3. Kinematic scheme of a martensitic converter

For convenience of further consideration, the ratio of the synchronizing transmission remains equal to one (1.00), and in the "belt" transmission of the nitinol engine, the ratio of the working pulleys is taken different from unity due to the increased diameter of pulley 2. In this case, if the working body in the form of a spring was previously given the occasion to "memorize" the compressed form, i.e. "turn to the turn", then being stretched out and placed in a hot environment, it shrinks, "remembering" its original form.

As an example, an arbitrary section of the working body is taken. If, during the passage of the compression section, shown as a continuous line,  $l$  is the length of the section, then its length in the stretched zone, marked by a dotted line, will be  $l\varepsilon$ , where  $\varepsilon$  is the specific deformation of the working body, which in the case of heating can return to the "memorized" form; being the specific deformation the ratio of an arbitrary length of the body segment in the stretched state to its length in the compressed state.

In order for the system to be moving, the travel time  $t$  of the point X through the hot region must be equal to its travel time through the cold zone. From this it follows that if  $v_1$  is the velocity of the working body moving through the compression zone, and  $v_2$  is its velocity through the tension zone, then

$$t = \frac{l}{v_1} = \frac{l\varepsilon}{v_2}. \tag{1}$$

Taking into account the foregoing, and also on the basis that  $\varepsilon$  is a value greater than one, it is concluded that the tension section should be longer than the compression section, so that the mass of the working body (the number of coils of the stretched spring) in one section is equal to the mass in the other section, as is the case, for example, with equal relations of the "belt" and synchronizing transmissions (see Fig. 2). This is a condition that ensures the rotation of the pulleys.

With unequal diameters of pulleys 1 and 2, it is possible to observe the condition

that ensures their rotation if the working body can change the length and have the shape memory effect, due to which the working body is compressed upon heating, "remembering" its original form, and stretched upon cooling. In this case, forces arise that cause the system to move if heat is applied and taken off at the respective sectors. The correct determination of the gear ratio of the martensitic converter is achieved by the selection of the working pulleys of the transmission. To determine the optimal diameter of the driving pulley, it is necessary to know the difference in the lengths of the working body in both tension and compression sections.

The diameter of the driving pulley 2 (Fig. 3) depends on how far the working body can be stretched in a cold environment. As mentioned above, the strain of the working body, from which it can still return to the original form, is  $\varepsilon$ ; this means that the permissible extension of the working body's length  $l$  should not exceed the value  $l\varepsilon$ , from which the required diameter of the driving pulley is determined [13].

The "free rotation condition" necessary for the operation of the martensitic transducer, need not be strictly observed provided the working medium is a spring slung over smooth pulleys, since there will be a slippage of the spring and the pulley, that is, the loss of energy. And the working body of the martensitic converter will itself regulate this process. If the working body is a chain, and instead of pulleys there are sprockets of different diameters, and slippage will be discarded, then the number of links of the working body in the martensitic and austenitic state should be equal, that is, the rotation condition must be met, otherwise the engine will not work.

In order for the system to be moving with maximum efficiency, it is necessary that the length of the austenite section  $l$ , and the length of the martensitic  $l\varepsilon$  satisfy the following equations:

$$l = \sqrt{a^2 + \frac{(D-d)^2}{4}} + \frac{\pi d}{2}, \quad (2)$$

$$l\varepsilon = \sqrt{a^2 + \frac{(D-d)^2}{4}} + \frac{\pi D}{2}, \quad (3)$$

where  $a$  is the distance between the centers of the pulleys,  $l$  is the length of working body in hot condition and  $l\varepsilon$  is the length of the working body in cold stretched state, at which it preserves the shape memory effect without residual deformations.

Subtracting the second equation from the first and carrying out the corresponding transformations, we obtain the following expression:

$$l\varepsilon - l = \frac{\pi D}{2} - \frac{\pi d}{2} \quad (4)$$

and hence

$$D = \frac{(2l)(\varepsilon - l)}{\pi} + d. \quad (5)$$

However, given that the distance between the pulleys is usually much larger than

their diameter, it can be assumed that

$$l = a + \frac{\pi d}{2} \quad (6)$$

and hence

$$D = \frac{(2a + \pi d)(\varepsilon - l)}{\pi} + d. \quad (7)$$

It is established that the greater the value of  $\varepsilon$ , the easier it is to constructively create a martensitic converter. Basically, the working body uses a spring element. However, the manufacture of a continuous wire and belt working element is associated with technological difficulties, which involve joining ends. Soldering and welding do not provide a reliable connection. The use of nitinol wire and tape is limited to a strain of 1.5%–4% with a number of operating cycles of  $10^5$ – $10^6$ , respectively. With an increase in deformation up to 6%, the number of cycles is  $10^2$  [8, 14], which is unacceptable. The connection of the spring working element (WE) requires an additional link, which when switched to working pulleys, causes noise and creates additional loads, adversely affecting the operation of the thermo-mechanical converter. The spring working element makes it possible to bring the spring deformation to 500–600%, but at the same time the traction force is reduced by a factor of about 60, with a wire diameter of 0.8 mm, the output power does not exceed 2 to 3 W, which makes it useful for demonstration and advertising [15–16]. In addition, breaks often occur in spring connections. We have manufactured and tested a number of spring-type converters, the graphic models of which being shown in Fig. 4.

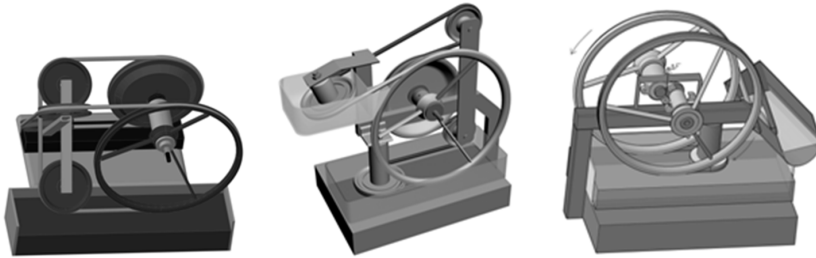


Fig. 4. Spring-type martensite converters created in the Institute of Machine Mechanics

To improve the characteristics of the rotary transducer, the power working element is represented by a combined chain (Fig 5), consisting of nitinol rings (1) connected together by traction pins (2) and side plates (3). Under the effect of the tensile force  $P$ , the ring deforms into an ellipse along the major axis:

$$t_M = d - d_1 + 2\Delta t, \quad (8)$$

where  $t_M$  is the chain link pitch after deformation in the martensitic phase,

$$d - d_1 = t_1, \quad (9)$$

where  $t_1$  is the pitch of the connecting holes of the side plates,  $2\Delta t$  is the increment of the inner diameter  $d$  of the working ring and  $d_1$  is the diameter of the connecting pin 2.

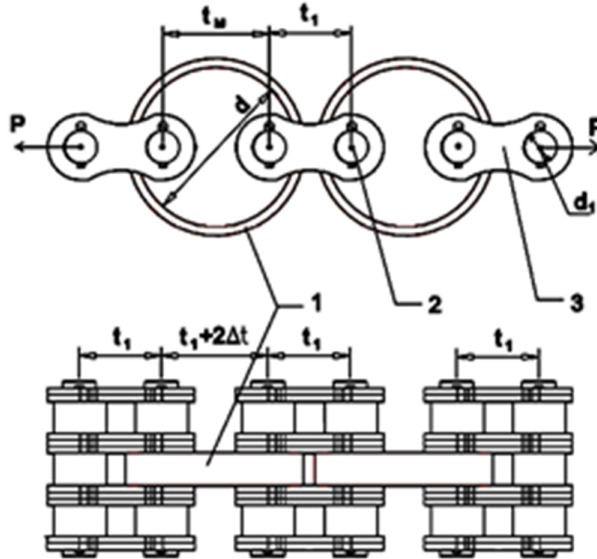


Fig. 5. Chain link with one working ring

When the working element is heated, the ellipse again assumes the shape of the ring, while developing in the austenite the force  $P_A$ , two to three times greater than the deformation force  $P_M$  in the martensite. This force is transmitted through the traction pins (2) and rollers (4) to the chain sprockets, on the shaft of which a torque is generated.

The annular form of nitinol allows a wide range of changes in the rigidity of the working ring of thickness  $t$  and length  $L$ , which can significantly increase the pulling capacity of the chain; the technology of its manufacture is quite affordable. In this version, the working element is one nitinol ring in the link. With reference to this chain, a model of the converter, shown in the photograph (Fig. 6), was created.

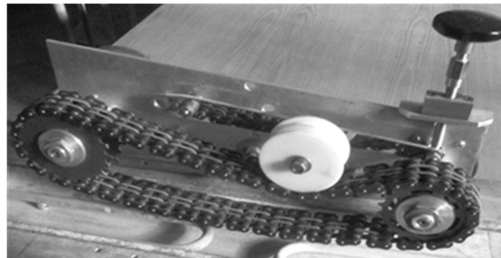


Fig. 6. Converter model with one working ring in the chain link

In order to increase the pulling capacity, a chain of four working rings was devel-

oped in one link (Fig. 7), where the axes of the pulling pins pass through the holes of the side plates (3) with some radial clearance. Within this gap, the ring can deform into an ellipse.

For this chain it was supposed to use the model in the classical way (Fig. 8).

Intrinsic Devices, Inc. (USA) [4, 11] produces nitinol rings, used as clamps for hoses and other products, recommends for rectangular cross-section thin-wall rings with  $t < d/10$ , the following calculation formulas of total radial force  $F$  and pressure  $P$  on the contact surface (Fig. 9):

$$P = 2t \frac{\sigma}{d} \quad (\text{MPa}), \quad (10)$$

$$F = 2\pi t L \sigma \quad (\text{N}), \quad (11)$$

where  $\sigma$  is the recoverable stress (200 MPa) based on the temperature, material properties and geometry of the ring [17, 18]. To calculate the parameters of the working chain with a nitinol ring, we use the scheme (Fig. 10).

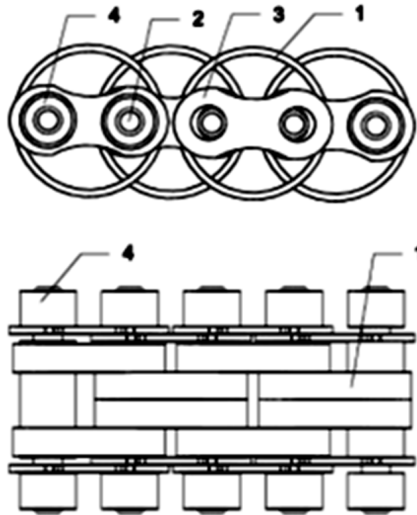


Fig. 7. Chain of four working rings in a link

The ring with the internal diameter  $d$  is stretched by the force  $P$  through the pins (rollers) of the chain side plate  $d_0$ , and, accordingly, the normal pitch in the circle is

$$t = d - d_0, \quad (12)$$

When the circle is deformed into an ellipse, the pitch is

$$t = d_1 - d_0. \quad (13)$$

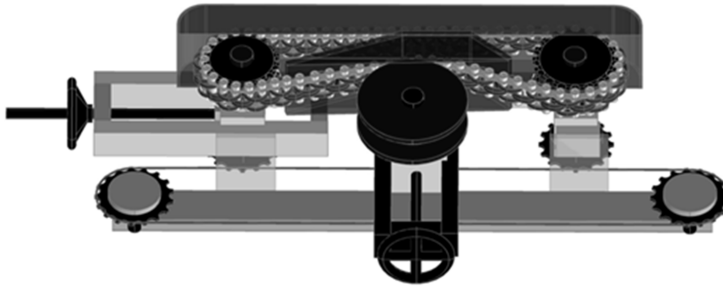


Fig. 8. Converter model with four operating rings in the chain link

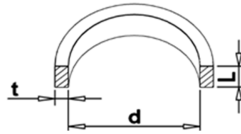


Fig. 9. Rectangular cross-section thin-wall ring

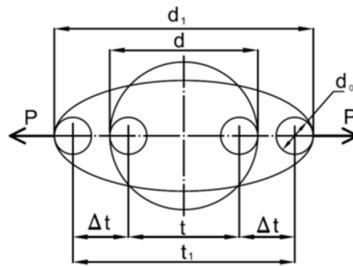


Fig. 10. Scheme for calculating working circuit parameters

The pitch increment is

$$2\Delta t = t_1 - t. \quad (14)$$

The deformation corresponding to the pitch of the working ring is

$$\varepsilon_i = \frac{2\Delta t}{t}, \quad (15)$$

ring diameter deformation is

$$\varepsilon_k = \frac{d_1 - d}{d} = \frac{t_1 - t}{t} = \frac{2\Delta t}{t}. \quad (16)$$

Here,  $\varepsilon_i > \varepsilon_k$  in an amount of  $t/d$ , i. e.

$$\varepsilon_k = \varepsilon_i \frac{t}{d} = \varepsilon_i \frac{d - d_0}{d} = \varepsilon_i \left(1 - \frac{d_0}{d}\right). \quad (17)$$

where  $d_0$  and  $t$  are selected according to the standards for chain drives, and the

inner diameter of the nitinol ring is determined from equation (12).

During the experiments and graph plotting, it was found that the task of calculating the ring element of the working chain is rather complicated and statically indeterminate. At the same time, experience shows that due to the hysteresis phenomena in the tension of the annular element, the non-renewable deformation is quite significant, which greatly reduces the range of working intervals, that is, making ineffective the use of the ring as a working body.

From the above, it is expedient to use for this purpose a deformed ring shown in Fig. 11.

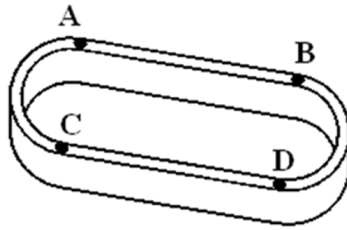


Fig. 11. Deformed ring

Since the regions AB and CD are rectilinear, when using this ring as the working body, bending deformations will be practically absent. It is known that nitinol in the austenitic state can restore its memorized shape, when it deforms to 4%, and there are forces that are two to three times higher than those that contributed to the initial deformation, that is, their magnitude in the straight regions will be quite significant. If instead of the circular ring shown within the chain in Figs. 2 and 3, the ring shown in Fig. 9 is used and the chain is configured according to the kinematic scheme of Fig. 3, it is possible to roughly calculate the forces and torque occurring in the converter.

The following problems inherent in thermal energy converters are solved herein:

1. There is no need to manufacture a continuous wire or belt element.
2. Welding or soldering of nitinol is not required either.

However, unlike the bending deformations that are present when forces are applied to the ring, stresses  $\sigma$  under tensile deformations arising in the operating element shown in Fig. 9, will reach 300–500 MPa. In this case, the force arising in the working element in the martensitic state is calculated by  $T_1 = \sigma S$ , where  $T_1$  is the force and  $S$  is the cross-sectional area. If  $\sigma$  is 300 MPa, and the cross-sectional area is 10 mm<sup>2</sup>, then  $T_1 = 3 \times 10^8 \text{ Pa} \times 10^{-5} \text{ m}^2 = 3000 \text{ N}$ . Since  $T_1$  is the force arising in the martensitic state, the force  $T_2$  arising in the austenitic state must be at least 2 times greater, hence,  $\Delta T$  will be not less than 300 N. Using the formula [2–3].

$$M_1 = M_2 = \Delta T(R_1 - R_2) \quad (18)$$

and assuming  $R_1 = 0.2 \text{ m}$ , one can calculate the torque that can occur in the converter:  $M = 3000 \times (0.2 - 0.184) = 48 \text{ N m}$ .

It can be expected that the use of the chain shown in Fig. 2 or 3 under the kinematic scheme in Fig. 3 will make it possible to obtain a rotational thermomechanical

converter with a combined operating chain of rather high power [8, 10].

However, the use of linear deformations to obtain significant capacities makes it necessary to create greater stresses in the mechanical parts, which will lead to their rapid wear. Therefore, a curved plate (Fig. 12) can be proposed as a working body. Here, by varying the number of bends and the values of  $S$ ,  $T$ ,  $R$  and  $L$ , one can achieve the optimum stiffness, heat transfer and the mass of the working body. This will make it possible to obtain a converter of the required capacity.

By chaining all these elements (Fig. 13), one can obtain the working body necessary to create a better energy converter.

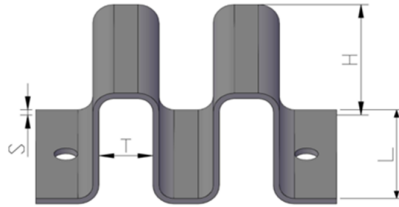


Fig. 12. Plate spring element

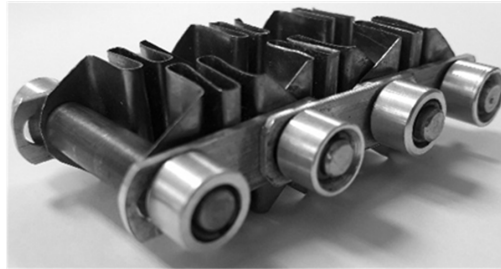


Fig. 13. Part of the converter chain

## 4. Conclusion

The above analysis of prospective schemes and designs of operating elements of the martensitic converter shows that to optimize their operation in order to obtain the highest capacity, it is necessary to use a martensitic converter with plate spring working elements.

## References

- [1] T. NARUTANI: *Effect of deformation-induced martensite transformation on the plastic behavior of metastable austenitic stainless steel*. Materials Transactions JIM 30 (1989), No. 1, 33–45.

- [2] J. MANJANNA, S. KOBAYASHI, Y. KAMADA, S. TAKAHASHI, H. KIKUCHI: *Martensitic transformation in SUS 316LN austenitic stainless steel at RT*. Journal of Materials Science 43 (2008), No. 8, 2659–2665.
- [3] A. BAUBLYS: *Methodology of transport system research*. Computer Modelling & New Technologies 6 (2002), No. 1, 72–81.
- [4] F. FOROUZAN, A. NAJAFIZADEH, A. KERMANPUR, A. HEDAYATI, R. SURKIALIABAD: *Production of nano/submicron grained AISI 304L stainless steel through the martensite reversion process*. Materials Science and Engineering: A 527 (2010), Nos. 27–28, 7334–7339.
- [5] M. ESKANDARI, A. KERMANPUR, A. NAJAFIZADEH: *Formation of nano-grained structure in a 301 stainless steel using a repetitive thermo-mechanical treatment*. Materials Letters 63 (2009), No. 16, 1442–1444.
- [6] D. SCHINO, I. SALVATORI, J. KENNY: *Effects of martensite formation and austenite reversion on grain refining of AISI 304 stainless steel*. Journal of Materials Science 37 (2002), No. 21, 4561–4565.
- [7] K. DATTA, R. DELHEZ, P. M. BRONZVELD, J. BEYER, H. M. GEIJSELAERS, J. POST: *A low-temperature study to examine the role of  $\varepsilon$ -martensite during strain-induced transformations in metastable austenitic stainless steels*. Acta Materialia 57 (2009), No. 11, 3321–3326.
- [8] A. A. GOLESTANEH: *Solid state engine using nitinol memory alloy*. United States Patent 4302939, [patents.google.com/patent/US4302939](https://patents.google.com/patent/US4302939) (1980).
- [9] R. M. BANKS: *Linear output nitinol engine*. United States Patent US4450686, [patents.google.com/patent/US4450686](https://patents.google.com/patent/US4450686) (1985).
- [10] J. L. KELLOG, M. GUO: *Nitinol heat engine with mechanical storage mechanism*. Patent Application Publication Mar. 10, 2016, US 2016/0069331 A1, [patents.com/us-20160069331.html](https://patents.com/us-20160069331.html) (2016).
- [11] J. S. CORY: *Solid state heat engine*. United States Patent 4305250, [patents.google.com/patent/US4305250](https://patents.google.com/patent/US4305250) (1981).
- [12] *Nitinol's crystalline structure*. <https://www.imagesco.com/articles/nitinol/03.html>.
- [13] [www.ultimateniti.com](http://www.ultimateniti.com).
- [14] K. OTSUKA, K. SHIMIZU, J. SUZUKI: *Alloys with shape memory effect*. M.: Metallurgy, 1990. In Russian.
- [15] J. MOLA, B. C. DE COOMAN: *Quenching and partitioning (Q & P) processing of martensitic stainless steels*. Metallurgical and Materials Transactions A 44 (2013), No. 2, 946–967.
- [16] K. MUMTAZ, S. TAKAHASHI, J. ECHIGOYA, Y. KUMARA, L. F. ZHANG, H. KIKUCHI, K. ARA, M. SATO: *Magnetic measurements of martensitic transformation in austenitic stainless steel after room temperature rolling*. Journal of Materials Science 39 (2004), No. 1, 85–97.
- [17] [www.ndt.net/article/v12n06/khan.pdf](http://www.ndt.net/article/v12n06/khan.pdf), Apr. 2012, SH Khan.
- [18] D. SCHINO, M. BARTERI, J. KAMADA: *Development of ultra-fine grain structure by martensitic reversion in stainless steel*. Journal of Materials Science Letters 21 (2002), No. 9, 751–753.

Received March 8, 2018

# A novel development of wireless mesh protocol data transmission framework for internet-based energy conservation

V. VIJAYASARO<sup>1</sup>, S. NITHYANANDAM<sup>2</sup>,  
N. PARVATHAM<sup>3</sup>

**Abstract.** This paper describes the design of wireless mesh network for the development of energy grid to overcome energy crisis problem. In past few decades, IoT and wireless sensor networks provides promising solution for implementation of real time systems in both industries and academics. To improve day today life quality, new era of technology IoT provides efficient way of machine to machine communication with internet by using wireless protocols. The proposed design has an advantage of low cost, high speed and good reliability for the implementation of energy grid.

**Key words.** Wireless mesh network, energy grid, IoT, wireless protocol.

## 1. Introduction

The novel paradigm named IoT was introduced by Kevin Ashton in the year 1990. Electronic products like Sensor, chips are used everywhere because of miniaturization and system of chip technology. Wireless sensors play a major role in IoT Communication [1–3]. Over few years with advancement of embedded devices and wireless sensors, the occurrence of IoT applications are productive, comfort, easy to use, Cost effective. IoT has great potential to communicate with unlimited devices over the internet. IoT intelligence is the technological revolution for future real-time applications. Internet of things provides promising solution for integrating sensors microcontroller wireless protocols to connect physical device to the internet. IoT emerges as new platform for consumer electronics continue to achieve performance

---

<sup>1</sup>Department of Electronics and Communication Engineering, PRIST University, Thanjavur, India, 613403

<sup>2</sup>Department of Computer Science and Engineering, PRIST University, Thanjavur, India, 613403

<sup>3</sup>Department of Electronics and Communication Engineering, P. R. Engineering College, Thanjavur, India, 613403

in terms of power and functionality and reduce cost of the system. IoT provides communication for the humans with machine anywhere and anytime.

Wireless mesh networks network is the hybrid network topology for cooperate point to multipoint communication. The performance of Wireless mesh networks in remote monitor and control of IoT applications are excellent. Wireless mesh network is a network used in communications and it consists of radio nodes that are structured in mesh topology. Customers are various electronic devices, embedded systems and several sensors that are used in communication process for interactive with people in a network. The router act as a link among two or more networks mainly for transmitting the data from one network to another. Another electronic device called gateway which acts as a passage through which the network connects to the internet [4].

In wireless mesh network while one node cannot function, the remaining nodes can be still efficient, and it can be utilized to communicate with others either straight or with the help of one or more intermediary nodes. The best quality of the wireless mesh network is simplicity and easiness to add new nodes without re-installing. The application of Wireless mesh networks has been used in the arena of remote monitoring and control system including environmental monitoring, the water meter infrastructure, automatic street light monitoring system, real time indoor carbon dioxide monitoring, data mining, Health care applications, Agriculture. The wireless module technology based physical layer such as Zigbee and radio frequency has been used in the above-mentioned studies. The topology of wireless mesh networks has a great benefit in terms of flexibility and reliability in comparison with other network topologies. The robustness of the network can be significantly enriched by using the self-organizing management approach that is present in the network nodes which finally ensuing in a strong mesh networking technology [5]. In smart ad hoc mesh networking technology, the node is used to observe the adjacent nodes initially and it is used to measure the strength of the signal. After that it chooses the proper neighbor for the synchronization of time and then based on it send the joining request. After that the neighboring node conveys the appeal to the gateway [6]. Later the gateway accepts the invitation and allocates the network resources for the node. The sensor network nodes can be allotted according to the mesh network with two or more communication paths predominantly for improving the consistency of network. Wifi technology based wireless mesh networks are appropriate for the Internet of Things applications because of its stress-free installation and connectivity [7, 8]. Wifi is a wireless communication technology which is based on internet protocol and it is widely used due to quality communication and better data security in contrast to another physical layer technology.

In present scenario, the lack of resources is major problem existing in the world. Of those resource electricity and water are the most needed resource for human in their daily life. Based on increasing demand of electricity, we design IoT based energy grid used for controlling and monitoring the power consumption by the various electrical load. The agenda of the paper is to reduce the use of active power consumption. The technology oriented products are used to help people to reduce usage of electricity as well as use it for their primary need. To change the circumstances

with use of technology. IoT is used to send the data to cloud by machine, hence it reduces human work. Energy consumed automatically updated to the cloud by interfacing sensor to each load.

The objective of the paper to avoid energy wastage, satisfy the energy growing demand and to improve security, reliability of the energy grid we design innovative energy grid. The remainder of this paper is organized as follows. In Section 2, a novel design of energy grid system based on nRF mesh network is described briefly and the outline of the control flow and software design of the system. And in Section 3, the experimental result and prototype of the system is elaborated. Finally, a conclusion is drawn in Section 4.

## 2. Design of the system

The objective of this paper is to designing wireless mesh network for energy grid, and it communicates to internet. The IoT is the path used for information exchange between objects and Internet. IoT mainly consists of three main streams. First things oriented, in this paper we use sensors such as AC712 sensor, relay load, ATMEGA328, PC. Second internet oriented, we communicate through RF protocols such as NRF2401, ESP8266 http based Wifi. We are designing wireless mesh network for transferring sensor value with another microcontroller. This is the basic work of my research. Wireless mesh network is the promising paradigm for multi hop feature. The main contribution of mesh network is flexibility in terms of self-organizing. Third semantic oriented developing smart applications, we develop energy grid.

### 2.1. Block diagram

The block diagram explains IoT based energy conservation system. IoT have capability to interconnect billions of sensors for data collection. Block diagram organized as two sections namely Transmitter section, Receiver section. Transmitter section used to sense current value by using Acs712 sensor and send data to the receiver section. By using Acs712 sensor every electrical load electrical consumption measured and sends data to microcontroller.

Microcontroller interfaced with PC, Process and stores the data. After that it sends data to receiver by using NRF2401 protocol. We use low cost RF Sensor for wireless mesh network. Wireless mesh network provides Modular architecture, low cost, decentralized network, larger range, no loss of data, failure proof. In the receiver section data sense retrieved at receiver section PC using NRF receiver. After that receiver Microcontroller send the data to cloud by using http based Wifi protocol.

ATMEGA328 ports have features that make simple, process of control and monitor. ATMEGA328 has inbuilt SPI and I2C communication features with using chip select pin. Three registers in microcontroller namely SPI Control Register, SPI status Register, SPI data register used for communication. The advantage of the whole system is fastest implementation and no loss of data.

## 2.2. Flow chart design

The firmware was presented based upon block diagram components. Flowchart explains the functionality of whole implementation. Initialize the process by power on the circuit. After that configure the sensors by using serial peripheral Communication. Electrical load interface in the block by using relay. Three types of electrical load are present. In this paper we use resistive load. By using microcontroller, data in the electrical load fetched and coded using memory. Data automatically uploaded to transmitter section of nRF module. nRF receiver section retrieved the data and sends it to core Microcontroller. Eventually machines communicate with internet.

Microcontroller sends the data to cloud by using Wifi module. First configure Wifi module by interfacing both ATMEGA328 microcontroller and nRF transmitter as well as Receiver. After that for transmission of data vice versa. Connect microcontroller transmitter to nRF receiver as well as nRF transmitter to Microcontroller receiver. The cloud stored the Data send by the Microcontroller and responds with reference of data. The Mesh network is depicted in Fig. 1, the corresponding flowchart is shown in Fig. 2.

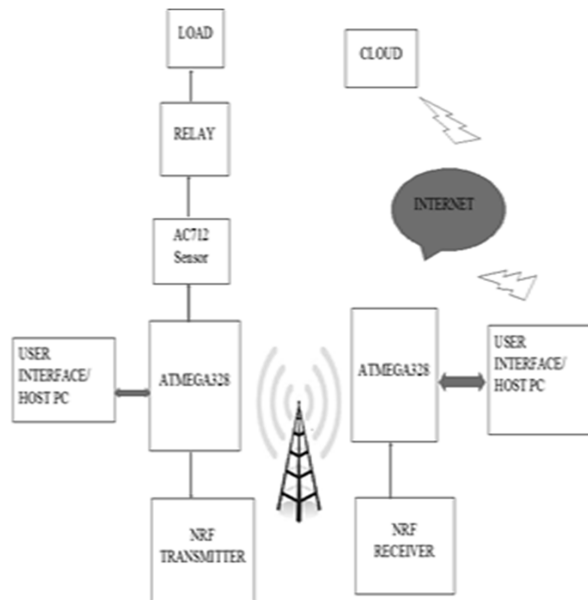


Fig. 1. Scheme of mesh network

## 3. Experimental results

The hardware and software implementation of energy grid prototype shown below. The aware of current consumption by customer is essential, because of high demand on energy resource. With the strength of IoT technology user can measure

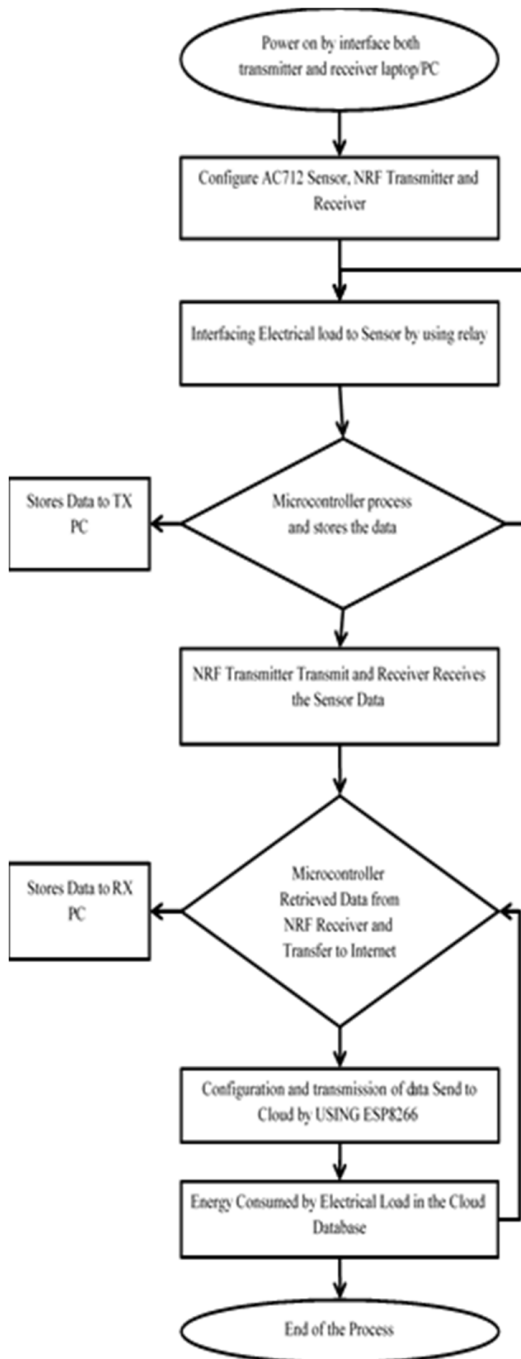


Fig. 2. Flow chart for basic mesh network

their current consumption by each load. We design simple kit of mesh network by using one electrical load.

### *3.1. Hardware implementation*

The hardware prototype for mesh network based energy grid shown below. The developed board is multihop connection and use two protocols namely nRF2401 and ESP8266 used for communication. Energy consumption can read from AC712 sensor. The developed prototype has features such as good efficiency, simple design and low power. The prototype of grid using the mesh network is in Fig. 3.

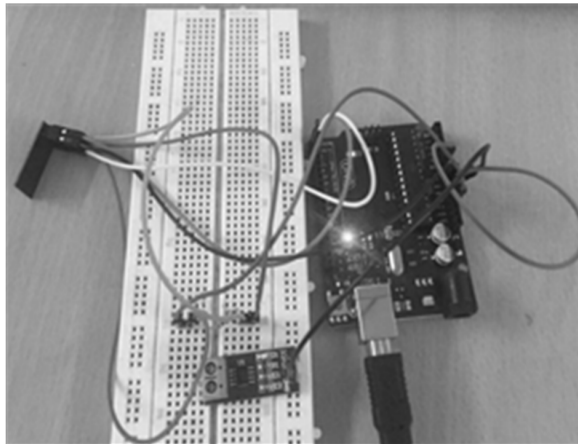


Fig. 3. Prototype of simple energy grid using mesh network

### *3.2. Visualization of data from cloud*

The current consumption by single load for the consumer shown in the figure data from cloud by using things we speak software. The graph shown in Fig. 4 is the web server output current data received by ESP8266.

By using this data user can control and monitor the whole system. Sensor value is retrieved as graphical representation. The user can get data of utilization of energy by their electrical load. So that we concentrate on saving energy.

## **4. Conclusion**

Design and implementation of wireless mesh network, IoT-based energy grid for saving energy is developed. Due to impact of energy crisis in this world, humans must concentrate on energy conservation. IoT technology helps with high potential features for analysis, monitoring and controlling functions for variety of applications. The developed protocol is the basic for my research idea. This paper focus on energy transmission, consumption. In future, we aim at generation of energy by using solar

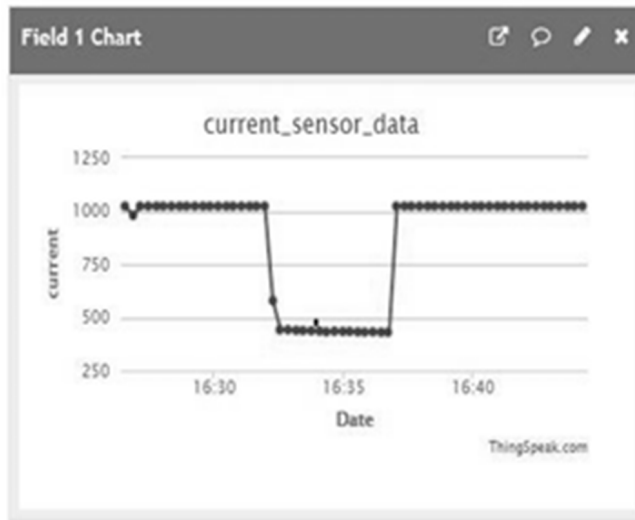


Fig. 4. Screenshot of energy meter current consumption data by electrical load

energy and distribution by using more number of electrical loads. We designed only using single electrical load in this paper. But our proposed work investigation towards energy grid for apartment blocks. Another important area must concentrate on gateway. In IoT technology, it is necessary to provide high end security introduce gateway concepts and focus on energy saving by demand energy management.

## References

- [1] L. QIN, D. M. ZHAO: *Channel time allocations and handoff management for fair throughput in wireless mesh networks*. IEEE Transactions on Vehicular Technology 64 (2015), No. 1, 315–326.
- [2] H. C. LEE, H. H. LIN: *Design and evaluation of an open-source wireless mesh networking module for environmental monitoring*. IEEE Sensors Journal 16 (2016), No. 7, 2162–2171.
- [3] R. MUHENDRA, HUSEIN, M. BUDIMAN, KHAIRURRIJAL: *Development of digital water meter infrastructure using wireless sensor networks*. Conference on Fundamental and Applied Science for Advanced Technology (ConFAST), 25–26 January 2016, Yogyakarta, Indonesia, Proceeding of ConFAST 1746 (1972), No. 1, p. 1–6.
- [4] M. KARTHIKEYAN, V. SARAVANAN, S. VIJAYAKUMAR: *Cloud based automatic street light monitoring system*. International Conference on Green Computing Communication and Electrical Engineering (ICGCCEE), 6–8 March 2014, Coimbatore, India, IEEE Conferences (2014), 1–6.
- [5] P. SPACHOS, D. HATZINAKOS: *Real-time indoor carbon dioxide monitoring through cognitive wireless sensor networks*. IEEE Sensors Journal 16 (2016), No. 2, 506–514.
- [6] M. COLLOTTA, G. PAU: *A novel energy management approach for smart homes using Bluetooth low energy*. IEEE Journal on Selected Areas in Communications 33 (2015), No. 12, 2988–2996.
- [7] G. MOIS, S. FOLEA, T. SANISLAV: *Analysis of three IoT-based wireless sensors for*

- environmental monitoring*. IEEE Transactions on Instrumentation and Measurement *66* (2017), No. 8, 2056–2064.
- [8] G. MOIS, S. FOLEA, T. SANISLAV: *A cyber-physical system for environmental monitoring*. IEEE Transactions on Instrumentation and Measurement *65* (2016), No. 6, 1463–1471.

Received October 12, 2017

# Research of the influence of polymeric drilling mud on the filtration-capacitive properties of polymictic sandstones

D. PODOPRIGORA<sup>1</sup>, I. RAUPOV<sup>1</sup>

**Abstract.** One of the main problems of the oil and gas industry, despite the high level of development of science and technology, is an effective primary and secondary opening of reservoirs, ensuring the preservation of the initial filtration and capacitance characteristics of the bottomhole zone. Even more important is the qualitative implementation of these operations with the introduction of low-permeability polymictic sandstones, since the productivity of producing wells can be significantly reduced as a result of the colmatation of the bottomhole formation zone. The example of the sample of the core of the Vyangapurovsky deposit shows the degree of change in permeability after exposure to it with drilling mud on a polymer basis. It was also established that it is possible to form a polymer membrane from the drilling mud at high reservoir temperatures.

**Key words.** Polymer drilling mud, polymictic sandstone, permeability, microcracks, Dnieper-Donets basin, polymer membrane, hydrochloric acid.

## 1. Introduction

One of the ways to preserve productive layers, which is widely used recently, is the opening of oil and gas reservoirs using polymer mud. The advantage of this drilling mud is that during the drilling process, the polymer is partially filtered out at the well-layer boundary, forming an almost impermeable crust that protects the formation and reduces the possibility of deep penetration of the mud filtrate into it. After drilling the well, the crust is easily removed by performing the hydrochloric acid treatment of the reservoir. In this article, we consider the results of laboratory experiments on the filtration-capacitance properties of four samples of polymictic sandstones from one of the gas condensate deposits located in the Dnieper–Donets Basin, drilling wells within which are carried out using polymer drilling mud (at the request of the subsoil user, we do not indicate the name of this deposit). In terms

---

<sup>1</sup>Oil and Gas Department, Saint-Petersburg Mining University, Russia, Saint-Petersburg, 21-st Line, 2

of the permeability, the studied samples correspond to the IV–V classes of collectors ( $0.001\text{--}0.1\ \mu\text{m}^2$ ) according to the A. A. Khanin classification [1–3]. It has been established that within the Dnieper–Donets Basin there is also a third-class collector (permeability  $0.1\text{--}0.5\ \mu\text{m}^2$ ). Samples with such permeability in the field could not be selected, therefore, to take up this class of reservoirs and compare the results of the experiments, the core of the Vyngapurovskoye oil and gas condensate field, located in Western Siberia, was taken for research. It should be noted that polymeric and polymer-clay drilling muds are also widely used in drilling the wells in this region, and the purpose of the experiments is to study the influence of xanthan polymeric drilling mud on the filtration-capacitive properties of polymictic sandstones of various permeability, which are often found in different regions, including the Dnieper–Donets Basin and Western Siberia. The core taken from Vyngapurovskoye oil and gas condensate field has an absolute permeability of  $123.52 \times 10^{-3}\ \mu\text{m}^2$  and is a polymictic sandstone with carbonate-clay cement (sample 417-1-4). Polymer drilling mud used for performing dynamic tests on the FDES-645 unit, is a mixture of the following components in %: biopolymer thickener (xanthan)–0.5, starch polysaccharide–2, potassium chloride–5, sodium chloride–20, carbonate filler (marble chips)–10, water–the rest.

The technology of preparation of this drilling mud does not require special equipment; for this purpose, any mixing unit (clay mixer, hydromesh mixer, solution preparation unit) is capable of creating intensive mixing and continuously maintain it for at least 4 hours. An important point is the uniformity of mixing the entire volume and the absence of stagnant zones in the cooking vessel. This solution is used in the most difficult geological conditions and is recommended for drilling at great depths. The solution provides effective suppression of hydration and swelling of clay rocks, is characterized by low water loss, and also has a heat resistance up to  $140\text{--}150\ ^\circ\text{C}$ . All of the listed properties of the mud are very important, since the opening of productive deposits occurs at a depth of about 5000 m, and the temperature in the investigated depth interval of the gas condensate field of the Dnieper–Donets basin is  $130\ ^\circ\text{C}$ .

## 2. Methodology

In the laboratory of Enhanced Oil Recovery of the Mining University, the density of the drilling mud was measured, the thermal stability of the drilling mud was studied at a temperature of  $130\ ^\circ\text{C}$ , the static shear stress was determined and an index characterizing the thixotropic properties of the solution was calculated. Also, the conditional viscosity was measured, the fluid loss and the thickness of the filter cake of the solution were determined, and rheological studies of the mud were carried out on the Rheotest RN 4.1 universal rotary viscometer. The density of the drilling mud was measured using a DE 40 density meter from Mettler Toledo at  $20\ ^\circ\text{C}$ . To determine the thermostability of the investigated mud under reservoir conditions, a temperature cabinet with a set temperature of  $130\ ^\circ\text{C}$  was used, in which the polymer solution was kept for 24 hours. Two samples were placed in the thermostat: a pure drilling mud in a volume of 40 ml and a mud (40 ml) in which 4 ml (10 %

of the total volume) of kerosene was added to simulate the process of condensate precipitation in the reservoir.

Further, the conditional viscosity of the drilling mud on the Marsh funnel was measured. Viscosity of drilling fluids should be minimal, but sufficient to hold suspended particles of drill cuttings and weighting agent at a given mud density. The water loss of the fluid was determined on the filter press FLR-1, which is designed to determine this index in solutions used in drilling oil and gas wells. Then, in the laboratory, the porosity and absolute permeability of the samples of the core of the gas condensate field of the Dnieper–Donets Basin and Vyngapurovsky oil and gas condensate field were analyzed. The porosity of the core was measured on a helium porosimeter TPI-219. Determination of the absolute permeabilities of samples by gas (air) was carried out on a TBP-804 unit. After the necessary core preparation, dynamic and static filtration experiments were performed on rock samples of the gas condensate field of the Dnieper–Donetsk basin and the Vyngapurovskoye oil and gas condensate field to simulate the influence of the drilling mud on the reservoir filtration an capacitive properties using a FDES-645 filtration unit.

### 3. Results

Based on the results of the measurement, the density of the tested drilling mud was  $1164 \text{ kg/m}^3$ .

The pure drilling mud and solution with kerosene proved to be stable during the entire experiment (24 hours) at a temperature of  $130^\circ\text{C}$ .

The values of the static shear stress of the investigated mud, measured after 1 and 10 minutes, are equal, respectively:  $\theta_1 = 9.952 \text{ Pa}$   $\theta_{10} = 13.684 \text{ Pa}$ .

The thixotropy coefficient, reflecting the rheological properties of the fluid, as a result of the calculations, is  $\kappa_T = 1.375$ . The obtained value of the exponent  $\kappa_T$  enters the required interval (1–1.5).

The conventional viscosity for mud on which the sand strata are exposed should be within an interval of 45–65 seconds.  $t_1 = 47$ ,  $t_2 = 46$ ,  $t_3 = 45$  ( $t_{\text{average}} = 46$ ).

As can be seen for the investigated mud, the obtained value of conditional viscosity corresponds to the required value. During the experiment, it was found that the investigated mud has a water loss of  $14.4 \text{ cm}^3/30 \text{ min}$  and forms a filter cake with a thickness of 0.4 mm. The results of studying the rheological properties of fluid on the Rheotest RN 4.1 are shown in Figs. 1 and 2.

As can be seen from the graphs presented in the figures, the polymer drilling mud has non-Newtonian properties and is a pseudo-plastic fluid, the effective viscosity of the solution decreases with increasing shear rate. It can also be seen on the graphs that the shear stress and the effective viscosity decrease significantly with increasing temperature, and consequently with increasing depth of the well, the viscosity of the mud will decrease and the hydraulic resistance in the circulation system decrease. The change in the viscosity of the mud at high temperatures will help to reduce the amplitude of pressure fluctuations during the start-up and shutdown of drilling pumps and perform downhole operations, as well as reduce the probability of formation of stagnant zones in the wellbore with the accumulation of

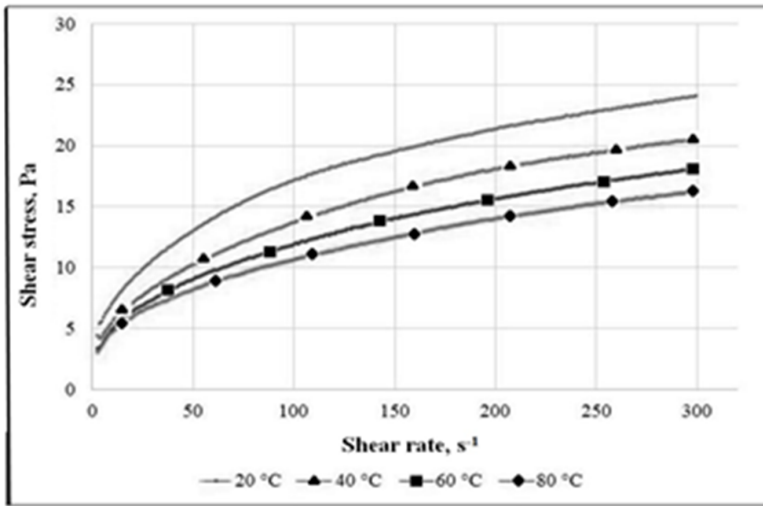


Fig. 1. Dependence of shear stress on the shear rate of shear

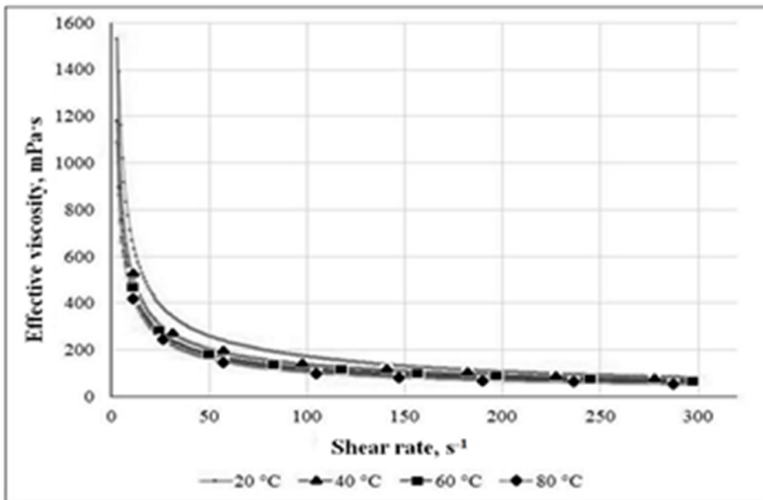


Fig. 2. Dependence of the effective viscosity on the shear rate

cuttings in them [4, 5].

Thus, as a result of laboratory studies, it was established that the polymeric drilling mud, used at the gas condensate field of the Dnieper–Donets Basin, meets all the necessary requirements for drilling fluids for drilling oil and gas wells. The results of extraction of 4 core samples of the gas condensate field of the Dnieper–Donets basin are shown in Table 1.

As can be seen from the presented table, sample 417-1-4 of Vyngapurovskoye oil and gas, the condensate field possesses the highest porosity and permeability. As for the gas condensate field of the Dnieper–Donets basin, here samples from

the interval of depths of 4961.5–4961.6 m are characterized by higher filtration and capacitive properties as compared to samples from the interval 4959.5–4959.6 m, which indicates a significant layerwise inhomogeneity of the productive horizon in vicinity of well No. 59, from which the core was selected.

Table 1. Results of extraction of 4 core samples of the gas condensate field of the Dnipro–Donetsk basin

No. of core	No. 1 4959.5–4959.6		No. 2 4959.5–4959.6		No. 1 4961.5–4961.6		No. 2 4961.5–4961.6	
	water	P+I (50:50)	water	P+I (50:50)	water	P+I (50:50)	water	P+I (50:50)
$d \cdot 10^{-3}$ (m)	29.9		29.9		29.9		29.9	
$L \cdot 10^{-3}$ (m)	74.04		56.6		72.4		73.85	
$Q \cdot 10^{-9}$ (m <sup>3</sup> /s)	8.3	8.3	1.7	2.5	16.7	16.7	16.7	16.7
$\Delta P$ (MPa)	4	1.8	5	2.5	0.65	0.41	0.46	0.28
$\mu$	1	0.688	1	0.688	1	0.688	1	0.688
$k \cdot 10^{-3}$ (μkm <sup>2</sup> )	0.223	0.342	0.027	0.057	2.689	2.897	3.848	4.325

The results of the porosity and absolute permeability measurements of the core samples are shown in Table 2.

Table 2. Results of measuring the porosity and absolute permeability in all 5 core samples

No. of core	No. 1	No. 2	No. 1	No. 2	417-1-4
	4959.5–4959.6	4959.5–4959.6	4961.5–4961.6	4961.5–4961.6	
$V_{\text{core}} \cdot 10^{-6}$ (m <sup>3</sup> )	51.99	39.74	50.84	51.85	44.90
$V_{\text{porous}} \cdot 10^{-6}$ (m <sup>3</sup> )	2.36	1.72	4.67	5.68	9.55
$M_{\text{sample}}$ (%)	4.54	4.33	9.18	10.96	21.28
$k \cdot 10^{-3}$ (μkm <sup>2</sup> )	1.02	0.32	7.09	14.69	123.52

For the core number 1 (4959.5–4959.6) of the gas condensate field of the Dnieper–Donetsk basin, a primary formation penetration was simulated, under conditions as close to the reservoir as possible, in a dynamic filtration regime, i.e. in the mode of washing the end of the core with drilling fluid, on the installation of FDES-645 (modification of the installation for working with the option Mud). The Mud option makes it possible to simulate the circulation of the drilling fluid in the device as well as in the well when the productive horizon is opened. The static filtration regime for the core No. 1 of the gas condensate field of the Dnieper–Donetsk basin was not modeled, the core has a very low permeability ( $k_{\text{air}} = 1.02 \mu\text{m}$ ).

Consequently, in the process of drilling, there occurs often absorption of drilling mud, associated with the opening of microcracks in the formation due to high re-pression. To confirm this conclusion, during the experiment, the pressure difference in the FDES-645 circulating system and the core pressure decreased periodically below the recommended value of 500 psi (3.5 MPa). This pressure difference ultimately led to the destruction of the sample at the end. Thus, during the dynamic experiment, it was established that technogenic cracks formed at the end of the core sample (Fig. 3), while the total porosity of the sandstone, following the scanning of the core on the SkyScan computer microtomograph, increased after the impact of the drilling mud by the calculations from 4.54 % to 12 %. This applies only to that part of the core sample where man-caused cracks were formed, the rest of the porosity remains unchanged. This experiment confirmed the presence of microcracks in the productive strata of the gas condensate field of the Dnieper-Donets Basin and the possibility of their disclosure due to differences in pressure and absorption of the drilling mud during the drilling process.



Fig. 3. Appearance of Core No. 1 (4959.5–4959.6) gas condensate field of the Dnieper–Donets Basin after simulation of the dynamic filtration regime

Further, dynamic and static experiments were carried out on the core of Vyn-gapurovskoye oil and gas condensate field. In the process of studying this core, the reservoir conditions of the gas condensate field of the Dnieper–Donets Basin were modeled ( $T_{\text{formation}} = 130^{\circ}\text{C}$ ,  $P_{\text{formation}} = 48.7\text{ MPa}$ ). The purpose of this experiment was to evaluate the change in the filtration and capacitive properties of polymictic sandstones after the polymer drilling mud was exposed to them. Simulation was carried out in 2 stages:

Dynamic mode of filtration of the mud, at which the solution was circulated along the end of the core with a constant flow rate; Static filtration regime at a constant effective pressure, which is equal to the difference in pressure of the drilling mud column at a depth of 4960 m and hydrostatic pressure. The constant effective pressure was 1157 psi (7.98 MPa). In the dynamic filtration regime, the polymer drilling mud was pumped at a flow rate of 1 ml/min for 4 hours, then the same time the sample was maintained in a static mode at a constant pressure of 7.98 MPa and a variable flow rate. The graph obtained in the course of the experiment is shown in Fig. 4.

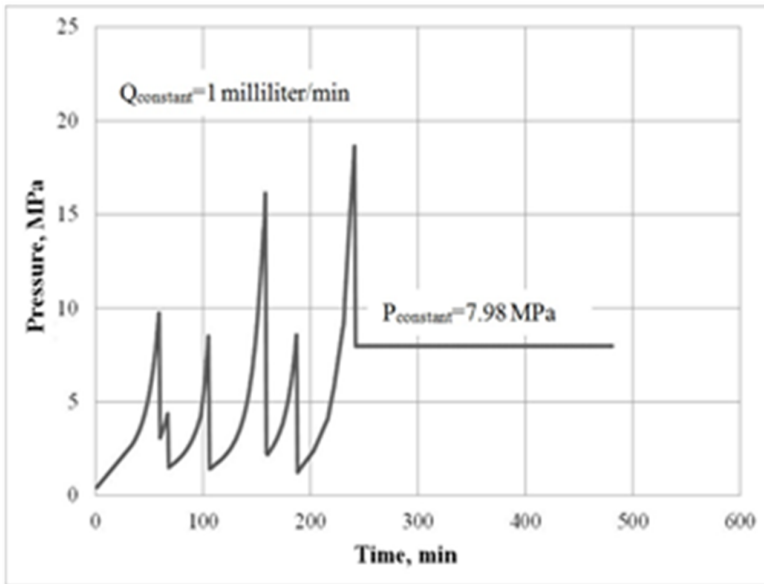


Fig. 4. Graph of pressure changes, obtained during simulation in dynamic and static modes

Under the dynamic regime of filtration of the polymer drilling mud along the core end, the same sharp changes in pressure were observed in the experiment as in the previous experiment on the core from Dnieper–Donets basin. After 4 hours, the installation was transferred to the static mode, i.e. in the regime of maintaining constant pressure at the end of the core. Figure 5 shows a sample of Vyangapurovskoye oil and gas condensate field core after dynamic and static tests on the FDES-645 unit.



Fig. 5. Appearance of the core sample from Vyangapurovskoye oil and gas condensate field after dynamic and static tests on the FDES-645 unit

Further, a mechanical removal of the filter cake from the end part of the core was carried out with the help of a metal scraper and the absolute permeability in gas was measured, in order to determine the change in the filtration characteristics of the test sample 417-1-4 after exposure to the drilling mud. The results of permeability measurements before and after exposure to the mud showed that the permeability of this sample decreased from  $153.52 \times 10^{-3} \mu\text{m}^2$  to  $64.31 \times 10^{-3} \mu\text{m}^2$ . In the work

[2], the influence of the polymer component of drilling fluids on the permeability of polymictic sandstones was investigated and similar results were obtained. High-molecular polysaccharides were the polymer components: platogel, xanthan gum and sodium carboxymethyl cellulose technical (Kamtsel-1000). The aqueous solutions of these polymers prepared at the concentration in which it was present in the drilling mud saturate the cores, then they were extracted with an alcohol-benzene mixture, dried and the gas permeability was measured. The results were obtained as follows: the presence of xanthan gum and Kamtsel-1000 in the pore space reduced the core permeability by 25–49% relative to the values obtained before saturation of these samples with aqueous solutions of polymers [2].

Thus, as a result of the experiment, almost a 2-fold decrease in the permeability was recorded, which is explained by the penetration of the mud filtrate and the carbonate particles of the solution weighting agent into the core. Also, in the laboratory experiment with the polymer filtrate produced by the filter press FLR-1, it was found that at high temperature (105 °C) water from it begins to evaporate and a solid polymer film is formed (Fig. 6). The formation of such a film can be explained by the fact that the composition of the drilling mud contains xanthan and various salts (KCl, NaCl), which can interact with rock-forming minerals. Thus, it was shown that at a high temperature a polymer film is formed from the filtrate, which can shield the hollow space of the matrix and cracks.

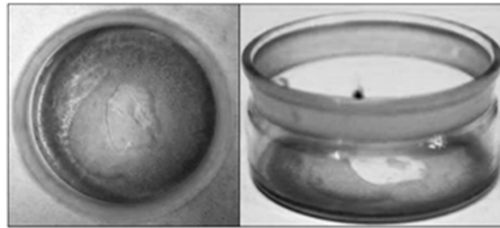


Fig. 6. Polymer film after evaporation of water from the filtrate

It is known that xanthanum and marble dissolve hydrochloric acid, the solutions of which are usually used to clean the productive formation after drilling wells using polymer drilling mud [1, 7]. To study the action of hydrochloric acid on the resulting polymer film in laboratory conditions, another experiment was carried out. In the course of which, an aqueous solution of 12% hydrochloric acid was gradually added to the bottle with the polymer film formed from the filtrate, which completely dissolved it. This experiment showed the effectiveness of the use of aqueous solutions of hydrochloric acid for the purification of bottomhole formation zone after the use of polymer drilling mud. However, how deep into the fissure-porous collector can penetrate and react the acid compared to the of the drilling mud filtrate to be clarified in subsequent experiments.

In conclusion, it should be noted that in low-porosity sandstones of gas condensate fields of the Dnieper–Donets basin there are microcracks that can expand during drilling and form the so-called technogenic fracturing. As a result, significant absorption of the washing liquid and deep penetration of the drilling mud into the formation take place, while the filtration-capacitive properties changes both in the

bottomhole formation zone and in its remote part. The polymer film, formed from the drilling mud filtrate, can also screen collector pores and microcracks.

#### 4. Conclusion

1. The investigated samples of the core of the gas condensate field of the Dnieper–Donets basin allow attributing the productive sandstones of the V-21 formation in well No. 59 mainly to the fractured-pore type of the reservoir. As shown by laboratory experiments, in the process of opening such sandstones, the microcracks present in them can be opened at a pressure difference in the FDES-645 circulating system and the core pressure is below the recommended value of 500 psi (3.5 MPa). During the experiment, the pressure drop reached 200 psi. Based on the obtained results, it can be argued that in real conditions of drilling wells at the opening of productive strata for repression, fracture processes will occur on a larger scale than in the laboratory.

2. The carried out filtration experiment on the sample of the core of the Vyn-gapurovskoye field showed that the polymer drilling mud used in drilling wells significantly reduces filtration-capacitive properties of polymictic sandstones. In this case, the absolute permeability of sample No. 417-1-4, after exposure to the mud, decreased almost twofold from  $123.52 \times 10^{-3} \mu\text{m}^2$  to  $64.31 \times 10^{-3} \mu\text{m}^2$ . This change in permeability can be explained by the deep penetration of the filtrate and particles of the carbonate weighting agent into the core, despite the presence of a protective filter cake at the end of the sample.

3. The laboratory experiment to study the effect of hydrochloric acid on a polymer film showed that a polymer film formed from a high-temperature (105 °C) filtrate of the mud can be effectively destroyed by a 12 % aqueous solution of hydrochloric acid, but in further laboratory experiments it is necessary to find out how deep it is capable to penetrate the fissured-pore sandstone and react with the contaminant.

4. The use of modern technologies of stimulation of the inflow during the development of wells, such as acid treatments and multi-stage hydraulic fracturing of the reservoir, as well as the correct selection of the acid composition and method of hydrochloric acid treatment bottomhole zone will significantly increase the productivity of low-porosity polymictic sandstones.

#### References

- [1] V. A. ZHILINA, N. A. SAMOILOV: *Directions of modernization of diesel fuel hydro-treating plants*. Internet-Portal. URL: <http://newchemistry.ru> (2017).
- [2] A. R. NASIRI, M. VALIZADEH, H. NOROUZI, M. HEMMATI: *Investigating the effect of polythin and polydrill on the properties of drilling fluids*. Journal of Petroleum Science and Technology 2 (2012), No. 1, 37–42.
- [3] A. A. HANIN: *Porod-collectives of Nephi and gas and their extinction*. Book on Demand Ltd. (2012), p. 367.
- [4] Z. ZHAO, X. PU, L. XIAO, G. WANG, J. SU, M. HE: *Synthesis and properties of high temperature resistant and salt tolerant filtrate reducer N, N-*

*dimethylacrylamide 2-acrylamido-2-methyl-1-propyl dimethyl diallyl ammonium chloride N-vinylpyrrolidone quadripolymer*. Information Processing in Agriculture 35(2015), No. 7 (<https://www.degruyter.com/view/j/polyeng.ahead-of-print/polyeng-2014-0260/polyeng-2014-0260.xml>).

- [5] Z. I. NIKOLAEV, E. L. LEUSHEVA: *Development of drilling fluids composition for efficiency increase of hard rocks drilling*. Journal of Mining Institute 219 (2016), 412–420.

Received October 12, 2017

# Parameters and operating modes of the working organs of the machine for harvesting forage grass seeds by comb on the root<sup>1</sup>

OMIRSERIK ZHORTUYLOV<sup>2</sup>, VLADIMIR SOLDATOV<sup>2</sup>,  
GANI ZHUMATAY<sup>2</sup>, ULAN BEKENOV<sup>2</sup>, AZAMAT  
ZHORTUYLOV<sup>2</sup>, SERIK ZHUMABAEV<sup>2</sup>

**Abstract.** The results of research on the development and justification of the parameters and operating modes of the working organs of the machine for harvesting forage grass seeds are presented. Two variants of machines for harvesting forage grass seeds (stripper) were developed: a hinged stripper with a combing drum, beads from rubberized combs and a trailing comb, with a brush drum for combing grass seeds and equipped with a cutting device for cutting stems. Analytic equations characterizing the trajectory and velocity of the end of the rubberized combs of the combing drum are obtained. Analytical dependencies characterizing the conditions of capture and length of the combs are established, the coefficient of the influence of the combs on the ears of the plant stems is determined. Theoretical and experimental studies were carried out and the parameters of the working bodies of the trailer stripper equipped with a brush drum and a cutting device are justified. The production tests were carried out, the quality of the alfalfa seedbed and the power needed to drive the machines were determined.

**Key words.** Harvesting of alfalfa seeds, combing drum, rubberized combs, brushes, power, grain harvester, cutting device.

## 1. Introduction

Out of 182 million hectares of pastures of the Republic of Kazakhstan, due to unsystematic grazing, 30–40% of pasture lands are subject to degradation. For

---

<sup>1</sup>This work is financed by the Science Committee of the Ministry of Education and Science of the Republic of Kazakhstan under the budget program 217 "Development of Science", sub-program 102 "Grant financing of scientific research".

<sup>2</sup>LLP «Kazakh Scientific Research Institute Mechanization and Electrification of Agriculture», Raiymbek Prospect, 050005, Almaty, Republic of Kazakhstan

the radical improvement of pastures, it is necessary to create a new grass stand by sowing high-yielding varieties of perennial and wild grasses [1–3]. To accomplish this task, seeds are needed in large quantities. The development of the country's economy provides for the transformation of the agro-industrial complex into a highly developed industry capable of providing the population with quality products. One of the main tasks in this direction is the creation of a stable fodder base for livestock, the development of which is constrained by the lack of the necessary quantity of seeds of forage grasses, especially alfalfa [4–9]. The most widespread in the conditions of Kazakhstan received a separate method. Alfalfa is mowed by harvesters (ZpRB-4.2, ZhVN-6, etc.) with the laying of the beveled mass in the roll. As the beans dry out, the rolls are picked up and threshed by conventional grain combines equipped with a PS-54-108 device. The stem mass during the harvesting period has an increased humidity (60% or more), high yield (up to 180 c/hectare). The purpose of the work is the development and justification of the design parameters and operating modes of the machine for harvesting grass seed (alfalfa) with a root comb, which ensures a reduction in seed losses and a high-quality execution of the technological process.

## 2. Materials and methods

The studies were carried out using classical methods of theoretical and applied mechanics, the theory of mechanisms and machines. Justification of the parameters and operating modes of the main working organs of the machine for harvesting the seeds of forage grasses; - checking the developed machine in production conditions. Experimental studies were carried out using strain gauges. A numerical analysis of the equation of motion of a comb of a reeling drum is performed using standard programs Excel, MatCaD. The processing of the results of experimental studies used the provisions of mathematical statistics. The 80% grain mass thus formed, consisting of free grain, seeds, under the action of inertia and air flow, moves to the screw conveyor and the inclined chamber is fed into the grinder of the combine for the window-hungry gutter and separation. The separator separates the seeds from impurities in the air stream, and enters the storage hopper. The tests showed that the stripper operation is possible at speeds up to 5.0 km/s, while the productivity of the machine with a working width of 2.7 m was 1.2 hectares/h.

## 3. Results

The drum combs, rotating around the horizontal axis and simultaneously moving forward with the machine, perform a complex movement with the speed  $V_0 = \omega R$  and simultaneously move forward with the machine at a speed  $V_m$ , perform a complex movement, where  $\omega$  is the angular velocity of the drum rotation in rad/s and  $R$  is the radius of the drum. The trajectory of this movement must be coordinated with the height of the arrangement of the spikes. Otherwise, the combs will not comb the plants, but will push them backwards [10]. In absolute motion, the point A of the

ridge describes the cycloid curve of parameters

$$x = V_m t + R \sin \omega t, \quad y = (H + h) - R \cos \omega t. \tag{1}$$

Taking the time derivative of equation (1) and taking into account that  $V_0 = R\omega$  and  $\gamma = \omega\tau$ , we define the projections of the speed of the point of the comb of the drum

$$\left. \begin{aligned} V_x &= V_m + V_0 \cos \omega t = V_m + V_0 \cos \varphi, \\ V_y &= V_0 \sin \omega t = V_0 \sin \varphi. \end{aligned} \right\} \tag{2}$$

The degree of impact of the ridge on plants is determined by the formula  $\lambda = V_0/V_m$ . The operating condition of the combing drum, i.e. the occurrence of combs in plants and their combing occurs at  $\lambda > 1$ , i.e., when  $V_0 > V_m$ . Usually,  $\lambda$  is taken within the limits of  $1.5 \cdots 1.7$ . At  $\lambda \geq 1.7$ , combs striking the ear can thresh seeds, creating losses, and at  $\lambda < 1.5$ , on the contrary, the combing drum will grab few stems and most of the stalk will not be exposed to it. Compliance with these conditions is necessary, so that the speed of the combs is between 8.0 and 16.0 m/s. Figure 1 schematically shows the work of the combs of a six-barrel drum, whose axis is located on the same vertical line with the front line of the bottom of the combing body. The input of the stems between the fingers of the combs occurs in the zone  $A_0B$  in the sections  $\Delta X$  by moving the machine, so that each comb combs the ears of those stems that occur to it on this segment.

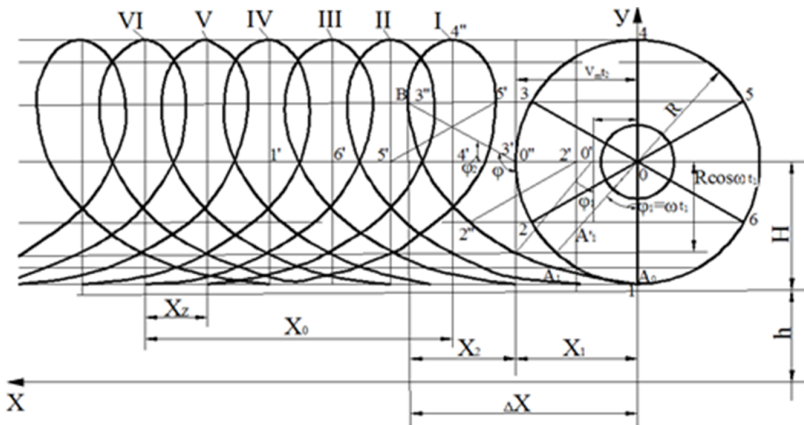


Fig. 1. Interaction of combs of combing drum with plant stems

Figure 1 shows that  $\Delta X = X_1 + X_2$ . On the other hand, when  $0 \leq X_1 \leq V_m t_2 = V_m t_1 + R \sin \varphi_1$ , then

$$X_1 = V_m t_2 = V_m t_1 + R \sin \varphi_1, \tag{3}$$

where  $\varphi_1 = \omega t_1$ , so that  $t_1 = \varphi_1/\omega$ . When  $0 \leq X_2 \leq R \cos \varphi_2$ , then  $X_2 = R \cos \varphi_2$  and  $\Delta X = V_m t_2 + R \cos \varphi_2$ .

Taking into account that  $V = R\omega/\lambda$ , we finally obtain

$$\Delta X = \frac{R}{2\lambda} (\pi + 2\varphi_2 + 2\lambda \cos \varphi_2) . \tag{4}$$

On a piece of the car's path, each row of combs grabs and combs the ears of the plant stems. If the drum has  $Z$  slats with combs and for one complete revolution of the drum the machine moves to a distance  $X_0$  equal to [10]

$$X_0 = V_m T = V_m \frac{2\pi}{\omega} = \frac{2\pi R}{\lambda} . \tag{5}$$

Then all  $Z$  slats with combs will sequentially capture the ears of plant stalks and comb the total length  $Z\Delta X$ . The coefficient of influence of the combs on the ears of the plant stalks is the ratio of the way in which the combs grab and comb the ears of the stems, to the entire path traversed by the machine during the same time

$$\eta = \frac{Z\Delta X}{X_0} = \frac{Z}{4\pi} (\pi + 2\varphi_2 + 2\lambda \cos \varphi_2) . \tag{6}$$

The step of the combing drum with slats and combs is the movement of the shaft (axis) of the combing drum  $X_z$  during the rotation time by an angle  $\varphi_z = 2\pi/z$

$$X_z = \frac{X_0}{z} = \frac{2\pi R}{\lambda z} . \tag{7}$$

Usually,  $\eta = 0.2 - 0.8$ . To increase the coefficient of action of the combs on the stems, it is necessary to increase the number of slats  $Z$  and the value of  $\lambda$ . With an increase in  $\lambda$  from 0.3 to 2.1, the coefficient of influence  $\eta$  increases more than 4 times. The number of slats  $Z$  with combs was chosen from the condition of combing all the bread along the length of the rut without missing (Fig. 2), i.e., a portion, combed by combs, must strictly follow the bread combed by the previous comb.

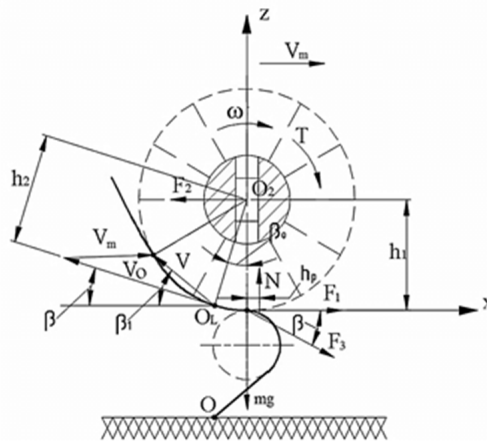


Fig. 2. Forces acting on the brush drum with its free movement in the vertical direction

The characteristics of harvested grasses are listed in Table 1

Table 1. Characteristics of harvested grasses

Denomination	Alfalfa	Fescue meadow grass	Rangeland ryegrass	Wheat grass
Height (cm)	95,0	70...75	55...60	40...60
Yield of seeds (c/ha)	3.0	2.5	2.5	2.65
Number of plants (t/m <sup>2</sup> )	420.0	310.0	270	210.0
Humidity seeds (%)	18.0	11.0	12.5	14.0
Humidity of stem mass (%)	65.0	40.0	43.0	30.0

The tests showed that at a speed of rotation of the combing drum with slotted combs  $n = 520$  rpm, the linear speed of the combs  $V_0 = 17.96$  m/s,  $V_m = 1.4$  m/s,  $V = V_0/V_m = 12.82$ , seed losses by shedding were 2.3–2.5 %, and at  $n = 720$  rpm, the linear velocity of the combs  $V_0 = 24.87$  m/s,  $V_m = 1.4$  m/s,  $V = V_0/V_m = 17.76$ , seed loss by shedding 2.2–2.4 %, and undercuts 0.5–0.7 %. The required engine power for the drive of the combing drum was 7.2 kW. The productivity of the stripper with a width of 2.0 m was 0.8–1.0 ha. Separation of alfalfa seeds is carried out directly on the root of the device (Fig. 2), consisting of a receiving chamber 1, mounted on it a pair of rollers: the upper brush drum 2 and lower roller 3. The power required to rotate the brush drum is determined by the formula  $P_1 = P_2 + P_3$  where  $P_2$  is the power needed to overcome friction of the brush on the stems of alfalfa, and also the breakage of the seeds is determined by the formula

$$P_2 = 4.7 \times 10^{-4} \times 736 D_2 n f_1 \cos \beta_1 F_3 \cos \epsilon, \quad (8)$$

where  $D_2$  is the outer diameter of the brush along the pile (m),  $n$  is the number of revolutions of the brush drum (rpm),  $f_1$  is the coefficient of friction of pile sliding on the surface of alfalfa stems,  $\beta_1$  is the angle of the pile with a fixed shaft,  $\cos \beta_1 = 1 - \Delta L_0/R_2$ ,  $\Delta L_0$  is the amount of deformation (sagging) of the pile,  $R_2$  is the radius of the brush drum (mm) and  $F_1$  is the force of action of brushes on stalks of plants (N).

The gap depends also on the number of leaves and seeds to be traversed, and, consequently, the power required to break off leaves and seeds. The moment  $T_1$ , which is expended directly on the breakage of leaves and seeds from the stems, is determined by the formula (see Fig. 2)

$$T_1 = F_1 \frac{D_2}{2},$$

where  $F_1$  is the the average tearing force of one leaf from the stem (N), where  $F_1 = fN$  and  $m$  is the average number of leaves terminated simultaneously in the series by a single ring of brushes. The values of  $F_1$  and  $m$  are determined as a result of laboratory studies.

Figure 3 shows the power variation curves  $P_2$ ,  $P_3$  and  $P_1$  as functions of the rotational speed of the brush drum. The graphs show that with increasing the rotational speed of the drum, the power is increased. With a frequency of rotation of the combing drum  $n = 1000$  rpm, the power required to comb the leaves and seeds of alfalfa  $P_1$  sharply increases to reach 5.0 kW, and the power required to overcome the air resistance to the rotation of the brush  $N_2$  is 2.0 kW.

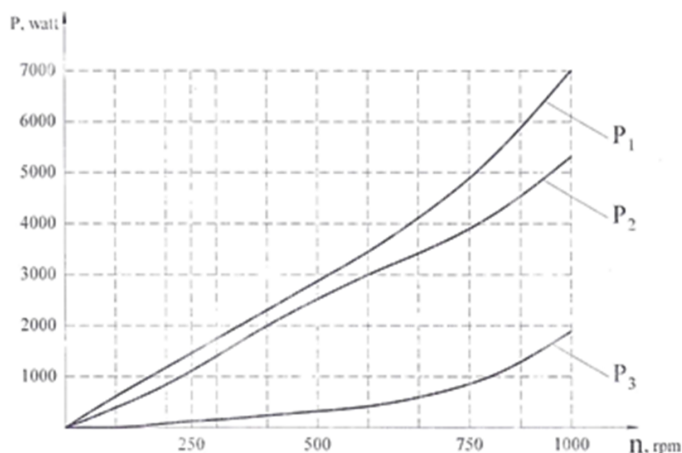


Fig. 3. Dependencies of the power  $P_1$  required to drive a brush drum,  $P_2$  to overcome the resistance of air to the rotation of brush and  $P_3$  to combing of leaves and seeds of alfalfa from the rotation speed  $n$  of the brush drum

When the machine moves along the field, the combing drum combs the leaves and plant seeds, rotating downwards together with the casing and support flap, creates a suction airflow that transports them to the storage hopper. Simultaneously, a mower with a segment-finger cutting device, installed at the bottom of the pallet behind the combing drum, cuts the lower part of the stems and puts them into the wire. After filling the receiving hopper, the leaves and seeds are unloaded by means of a conveyor into vehicles. The brush drum with nylon brushes with a diameter of 2.0 mm, a length of 220 mm and a working width of 2.0 m was tested. In the experiments, the quality of the seeds and leaves collected from 100 m<sup>2</sup> was estimated at a brush speed of  $n = 250$  and 500 rpm and different ratios of the peripheral speed  $V_0$  of the brushes to the translational speed  $V_m$  of the machine. The power required for the drive of the universal machine of the trailer was determined by the formula:  $P = T\omega = T\pi/30$  W, where  $T$  is the torque on the drive shaft (Nm),  $\omega$  is the angular speed of shaft rotation (rad/s) and  $n$  is the shaft rotation speed (rpm).

Experiments have shown that with an increase in the peripheral speed of the drum 13.0–20.0 m/s, the amount of seeds and leaves collected increases, but at the

same time the content of debris of stems in the heap increases. As the speed of movement increases, the loss of seed from cut plants increases from 0.2 to 2.5%. This is due to the fact that with increasing speed of the stripper movement, the bending of the bent stems increases with the casing of the drum and the brushes do not grasp the bent stalks of the plants (Figure 4). The productivity of the machine was 1.08 ha/h. The oscillogram of the torque readings is shown in Figure 5.



Fig. 4. Combing of alfalfa seeds with a trailed universal machine

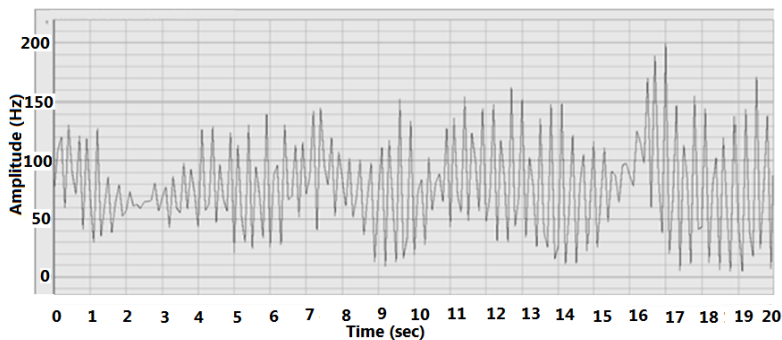


Fig. 5. Oscillogram of the sweep of the stripping device universal machine for harvesting alfalfa seeds and stamping

As a result of the theoretical and experimental studies of the working organs of the trailing machine for harvesting seeds and leaf mass, the parameters of the machine's working parts are justified: rotation speed: combing drum with brushes - 250–500 rpm, conveyor auger shaft  $n = 410 - 540$  rpm,; crooked-spike shaft - rpm, the power required to rotate the brush drum when combing the leaf mass and seeds is determined. The best quality indices of the comb is provided at a speed of machine movement 1.0–1.5 m/s, the speed of the reeling drum is 500 rpm, and the cut quality of the stem part of the plants is ensured at a crank shaft speed of 460 rpm.

#### 4. Conclusion

A promising way of harvesting grain crops, as well as testes of grasses by direct combining is to comb the grain from the ears and feed the combed mass into the combine. The parameters of the working organ of the combing drum are proved: the hinged stripper: the number of slats with the rubberized combs  $z = 6$  pcs, the

length of the rubberized combs  $l = 220 - 240$  mm, the distance between the lateral surfaces of the combs  $t = 10 - 12$  mm. The production test of the hinged stripper was carried out: at frequencies of rotation of a reeling drum of 520 rpm and 720 rpm. Velocity of the stripper movement is  $V_m = 1.4$  m/s, the degree of influence of the combs on the plants  $\lambda = V_0/V_m = 12.82 - 17.76$ , seed loss by shedding 2.2–2.4%, and underdosage - 0.5–0.7%. The crushing capacity of the engine for the drive of the combing drum was 7.2 kW. The productivity of the stripper with a working width of 2.0 m was 0.8–1.0 ha. Theoretical and experimental studies were carried out on the trailing stripper and the parameters of the working bodies of the trailer stripper equipped with a brush drum and a cutting device were justified. Production tests of the combing machine were carried out during the harvesting of alfalfa seeds, the quality of alfalfa seed coat and the required power for the drive were determined. The power required to unload seed and leaf mass is 0.4 kW. The capacities required for driving the combing drum and mower with a segment-finger cutter do not exceed 12.0 kW. The productivity of the machine was 1.08 ha/h. Possible perspectives for further research is to work to reduce losses when harvesting combing grain of loose breads, grass seeds by installing stems.

## References

- [1] I. I. ALIMAYEV: *To the question of pastures*. AgroAlem (2017), No. 11, 44–47.
- [2] ARUNAKUMAR: *Standardization of seed production technologies in lucerne (medicago sativa l.)*. Dissertation thesis, University of Agricultural Sciences, Dharwad, India (2014).
- [3] L. MU, H. LIU, Y. CUI, L. FU, Y. GEJIMA: *Mechanized technologies for scaffold-ing cultivation in the kiwifruit industry: A review*. Information Processing in Agriculture (2018), in print (<https://www.sciencedirect.com/science/article/pii/S2214317318301161>).
- [4] A. SH. DZHAMBURSHIN, G. D. TURymbETOVA: *Substantiation of expedient parameters and operating modes of the stripping device for harvesting grain crops in Kazakhstan*. Kainar 8 (2017), No. 11, 152.
- [5] H. ARYAN, M. GHASSEMIEH: *A superelastic protective technique for mitigating the effects of vertical and horizontal seismic excitations on highway bridges*. Journal of Intelligent Material Systems and Structures 28 (2016), No. 12, 1533–1552.
- [6] A. JAMES, V. ZIKANKUBA, F. YILDIZ: *Postharvest management of fruits and vegetable: A potential for reducing poverty, hidden hunger and malnutrition in sub-Saharan Africa*. Cogent Food & Agriculture 3 (2017), No. 1.
- [7] C. RAJ, E. TRYBULA, I. CHAUBEY, S. M. BROUDER, J. J. VOLENEC: *Watershed scale impacts of bioenergy crops on hydrology and water quality using improved SWAT model*. Gcb Bioenergy 8 (2016), No. 4, 837–848.
- [8] V. STONE, J. P. LANE: *Modeling technology innovation: How science, engineering, and industry methods can combine to generate beneficial socioeconomic impacts*. Implement Sci. (2012), No. 35, p. 48.
- [9] I. CALESTOUS: *Building new agricultural universities in Africa*. [https://dash.harvard.edu/bitstream/handle/1/9359206/rwp12-026\\_juma.pdf?sequence=1](https://dash.harvard.edu/bitstream/handle/1/9359206/rwp12-026_juma.pdf?sequence=1)
- [10] *Combing reapers "Slavyanka"*. Ukr.AGRO-SERVICE, <http://ukragroserv.com.ua>.

# Effect of a near-surface nanolayer formation on the magnetic fluid electrical properties<sup>1</sup>

N. V. KANDAUROVA<sup>2</sup>, V. V. CHEKANOV<sup>3</sup>,  
V. S. CHEKANOV<sup>2</sup>

**Abstract.** In a magnetic colloid- a magnetic fluid (MF), which is placed in an electrochemical cell (a flat capacitor), a thin near-surface layer is formed in the electric field. This layer is an active medium in which the process of self-organization – autowaves was observed and studied. The layer consists of magnetite particles with a protective coating—oleic acid (HOI). We found a several orders increase of capacitance and a few times increase in the resistance of an electrochemical cell filled with a magnetic fluid by sending a pulsed electric field to the electrodes. Electrodes in the cell are thin transparent conductive ITO (InSnO<sub>2</sub>) membranes deposited on the glass. The cell reflectivity (reflectance) changes due to the formation of the near-electrode layers of magnetic fluid nanoparticles in the electric field. It can be registered by the interference of the falling light in these layers. The thickness of the near-electrode layer is estimated from the change in the reflectivity of monochromatic light. With increasing voltage on the electrodes, the layer becomes unstable, it periodically arises and collapses. As a result, the intensity of the reflected light fluctuates. When illuminated with white light, brightly colored waves are visible on the surface of the cell.

**Key words.** Polarization capacitance, magnetic fluid, near-electrode nano-layer, autowaves.

## 1. Introduction

Magnetic fluid (MF) is a stable colloid of single-domain ferromagnetic particles (magnetite) dispersed in various liquids (kerosene, water, etc.) [1]. The effect of an electric field on the magnetic fluids leads to a number of interesting phenomena: a change in the reflectivity of a cell with MF, formation of a layer of close-packed

---

<sup>1</sup>The work was performed as the element of the basic part of the state task Project No. 3.5385.2017/8.9 for the implementation of the project on the topic: "Experimental research and mathematical modeling of interphase and near-surface phenomena in a thin membrane of a nanostructured magnetic fluid

<sup>2</sup>Moscow Technological University, (MIREA, Stavropol branch) pr. Kulakova 18, 355029 Stavropol, Russia

<sup>3</sup>North-Caucasian Federal University, Pushkin st. 1, Stavropol, Russia

magnetite particles with a protective coating near the electrode, and the appearance of autowaves [2]. In the absence of an electric field, the magnetic fluid, placed in a cell between two electrodes is homogeneous [3]. When the field is turned on, the particles of the solid phase start migrating under the influence of electrophoresis and dipolophoresis, and on the surface of the electrodes the concentration of magnetite particles increases to a value of 25–27% vol., so the near-electrode layer is formed. This layer is a unique active medium in which an autowave process is observed. The purpose of this paper is to show that the formation of a near-electrode layer consisting of magnetite nanoparticles affects the increase in the capacitance and conductivity of an electrochemical cell with a magnetic fluid.

## 2. Materials and methods of the experiment

A magnetic fluid of the "magnetite in kerosene" type was used in the experiment. The concentration of magnetite is 3.2% vol. Dielectric permittivity of fluid  $\varepsilon = 2.1$ , conductivity  $\sigma = 3.8 \cdot 10^{-7} \Omega\text{m}^{-1}$  (measured at a frequency of 1000 Hz). The average size of magnetite particle is  $\sim 10$  nm. The experimental device is shown in Fig. 1. The magnetic fluid was placed in an electrochemical cell, consisting of two electrodes made of glass with a conductive transparent coating  $\text{InSnO}_2$  (ITO). The electrode surface area  $S = 40 \times 30 \text{ mm}^2$ . The glass thickness of the samples is 4 mm, the thickness of a conductive coating is  $h_0 = 160 \pm 5$  nm, the thickness of the magnetic fluid layer  $l = 40 \mu\text{m}$  (Fig. 1A). The capacitance of the electrochemical cell (static capacitance), calculated by geometric dimensions, measured at a frequency of 1000 Hz is  $C_{\text{st}} = 6 \cdot 10^{-10}$  F.

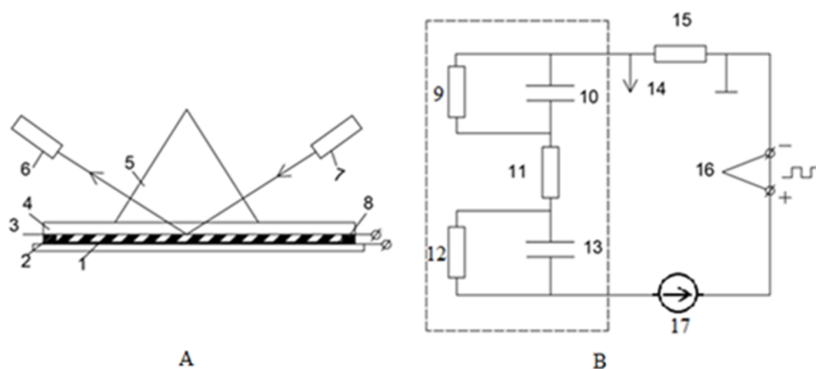


Fig. 1. Scheme of the experimental device. A—cell with a MF; 1—magnetic fluid, 2 and 4—transparent conductive coated glass (ITO), 3 and 8—insulating gaskets, 5—prism, 6—photodiode, 7—illuminator (laser), B—equivalent circuit of electrical measurements (the equivalent circuit of the cell with the MF is dashed); 9 and 12— $R_1$ ,  $R_3$  (resistances of near-electrode layers), 10 and 13— $C_2$ ,  $C_5$  (capacitances of electrode layers), 11— $R_2$  (resistance of interelectrode layer), 14—oscilloscope input, 15— $R_4$  (oscilloscope shunt), 16—terminals connected to the output generator of unipolar rectangular pulses, 17—EMF of electro-chemical (Faraday) polarization

The electrodes 16 (Fig. 1B) were supplied with rectangular pulses: amplitude  $U$ ,

impulse length is half of a period. The pulse period was 2.2 s. Front is less than  $1 \mu\text{s}$ . The output resistance of the generator is  $600 \Omega$ .

When switching on the pulse voltage, the current through the shunt ( $10^5 \Omega$ ) passes through the cell with the MF. The dependence of the current on time was recorded with the oscilloscope (Figs. 2 A,B,C)

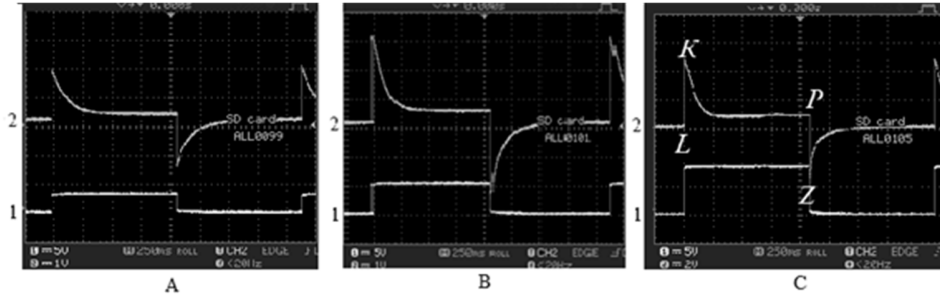


Fig. 2. Beams #1–dependence of the current flowing through cell on time, beams #2–impulse voltage  $U$  at the electrode: A– $U = 2.5 \text{ V}$ , B– $U = 4 \text{ V}$ , C– $U = 6 \text{ V}$

At the moment of the electric pulses switching on and off, the current is maximal (points K and Z in Fig. 2C), after a time  $\tau \sim 200 \text{ ms}$  the current becomes stationary. After applying a voltage in the cell, a layer of particles forms near each electrode, and we assume that this is the cause of the change in the current value.

We show below how we detected the formation of a near-electrode layer using the method of electrically controlled interference [4, 5]. Electrically controlled interference (electrointerference) occurs when light is reflected from electrodes in an electrochemical cell with a magnetic fluid. In an electric field, the particles of the dispersed phase (magnetite) migrate to the electrodes. In this case, the optical properties of the medium near the transparent electrode change (the complex refractive index increases). The reflected light properties change as well. When the cell surface is illuminated with monochromatic light, the reflectivity of the reflected ray varies periodically with the layer growth. By registering the change in the intensity of the reflected beam (optical response), we can state that the near-electrode layer was formed and we can measure its thickness by the method described in [4]. The method for obtaining the optical response is as follows (Fig. 3): the laser beam (1 mm in diameter, wavelength  $\lambda = 650 \text{ nm}$ , TE-polarization) was directed to the surface of the MF cell. The beam was reflected from the “glass–ITO membrane”, “ITO membrane is a layer of magnetite particles” and “layer of magnetite particles–MF” surfaces and entered the photodiode. It is connected to the input of a double-beam oscilloscope GDS-71022, which allows recording the voltage change on a photodiode FD-256 (optical response) with time (Fig. 4, beam 1 and Fig. 3).

We note that the change in the near-electrode layer thickness is fixed precisely by the optical signal [5]. Beam 2 on the oscillogram in Fig. 4 is the dependence of the current in the cell with the magnetic fluid on time. The section AEB corresponds to a change in the current in the cell when the electric pulse is turned on.

Comparing the sections AEB (beam 2) and CFDN (beam 1), we can see that a change in the current through the cell occurs simultaneously with the formation

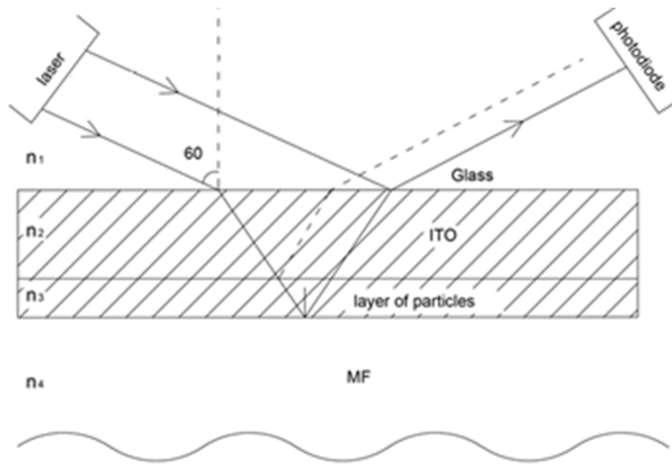


Fig. 3. Model of multilayer structure “glass-ITO—layer of particles—MF” with the course of the rays

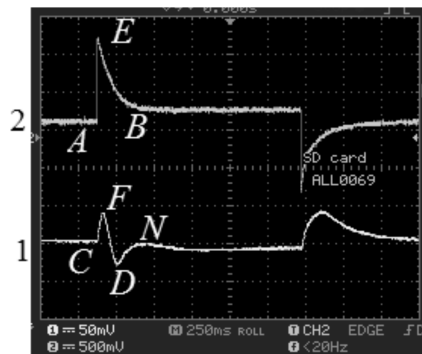


Fig. 4. Beam 1—optical response of the reflected beam (voltage on photodiode), beam 2—dependence of cell current with the magnetic fluid on time

of a near-electrode layer of magnetite nanoparticles. These observations give us reason to conclude that the reason for the change in cell current is the formation of near-electrode layers.

### 3. Results

#### 3.1. Resistance calculation of the electrode layers

The oscilloscope GDS-71022 used in the experiments allows not only to derive the current dependence through the cell  $i(t)$  on the screen (Figs. 2 and 4), but to write to the Excel file: 1000 data units for one second (Fig. 5). For calculations it is convenient to use the graph obtained from these data.

By the maximum value of the current  $i_{\max} = 58 \mu\text{A}$  at the moment of switching

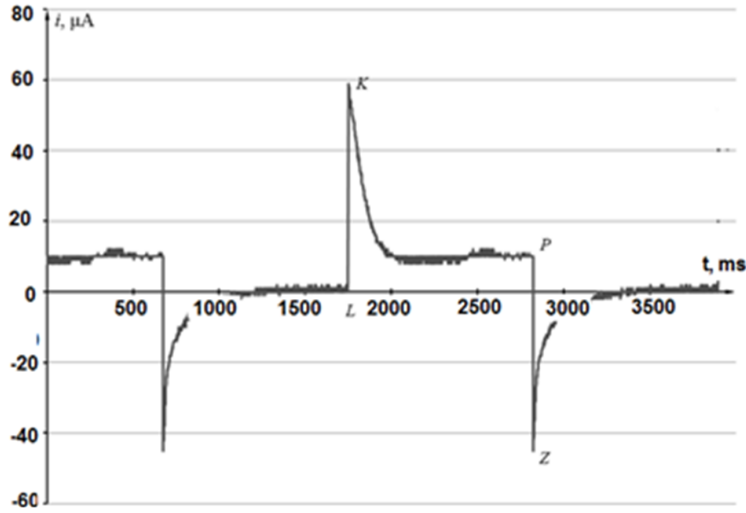


Fig. 5. Dependence of current in a cell with a magnetic fluid on time, impulse voltage on the electrodes  $U = 8\text{ V}$

on (point  $K$  in Fig. 5) and the voltage in the pulse  $U = 8\text{ V}$ , we found the cell resistance before the appearance of the near-electrode layer— $R_{\text{before}} = 1.4 \cdot 10^5\ \Omega$ . As expected, it is equal to the resistance of the cell, measured for alternating current. The stated current is  $\approx 10\ \mu\text{A}$ . So the cell resistance, after the formation of layers, is  $R_{\text{after}} = 8 \cdot 10^5\ \Omega$ . Thus, after the formation of the layers, the resistance of the cell with the magnetic fluid increased six times. In the experiment, the currents in the cell  $i_1$  (voltage on) and  $i_2$  (voltage off) are equal to each other within the error of the experiment (sections  $KL$  and  $PZ$  in Figs. 2C and 5) and are determined by the formulas

$$i_1 = \frac{U - E}{R_c}, \quad (1)$$

$$i_2 = \frac{U + E}{R_c}, \quad (2)$$

where  $R_c$  is the resistance of a cell with a magnetic fluid,  $E$  is the EMF of electrochemical (Faraday) polarization (Fig. 1B). The signs "+" and "-" in EMF in formulas (1) and (2) are related to the fact that the charge current  $i_1$  and the discharge current  $i_2$  have different directions. Consequently, the EMF of the electrochemical (Faraday) polarization is much less than the voltage in the pulse and can be ignored. By the difference in resistance before and after the formation of layers, the sum of the near-electrode layers resistances was found:  $R_{\text{ls}} = (6.6 \pm 0.5) \cdot 10^5\ \Omega$ .

### 3.2. Resistance calculation of the electrode layers

The charge  $Q$ , accumulated in the cell, can be found by integrating the dependence of  $i(t)$  on time from the moment of switching off the voltage (point  $Z$  in Fig. 5)

to  $i = 0$ .

$$Q = \int_{t_1}^{t_2} i \, dt = (6.9 \pm 0.3) \cdot 10^{-6} \text{ C}, \quad (3)$$

where  $t_1 = 0$  is the moment of switching off the voltage and  $t_2 = 1.1$  s.

It is known that the capacitance associated with the dependence of its magnitude on the voltage and time of electric current flow (polarization capacitance) can be calculated by the formula

$$C_{\text{pol}} = Q/U. \quad (4)$$

For the voltage  $U = 7$  V on the electrodes, it is  $(0.9 \pm 0.1) \cdot 10^{-6}$  F, for the voltage  $U = 5$  V the capacitance is  $(1.3 \pm 0.1) \cdot 10^{-6}$  F, and for the voltage  $U = 5$  V the capacitance is  $(2.2 \pm 0.3) \cdot 10^{-6}$  F.

### ***3.3. Change in the cell capacitance and the resistance of the near-electrode layers is the cause of the self-oscillations of the near-surface layer***

The thickness of the near-electrode layer was calculated by the oscillogram in Fig. 5 and equals  $\sim 100$  nm. At a voltage  $U = 15$  V, local self-oscillations arise which were fixed by the oscillations of the optical signal (Fig. 6A). The oscillogram in Fig. 6A was obtained when the voltage divider 1:10 that was switched on to the oscilloscope input (channel 2).

After the transient process, the oscillations become regular and an autowave process starts in the cell (Fig. 6B).

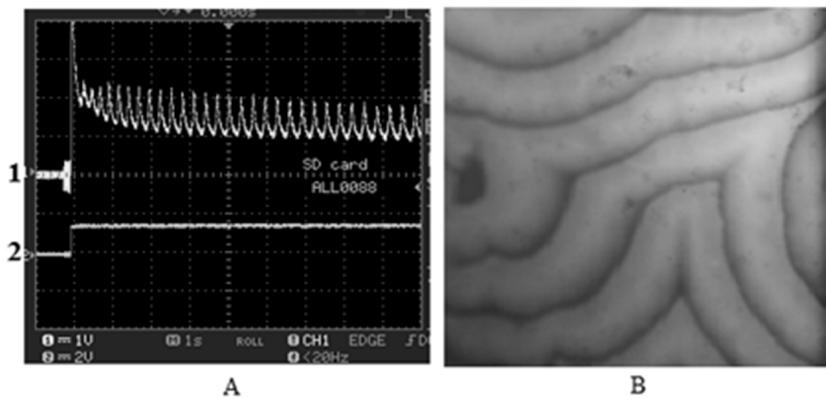


Fig. 6. Autowave process in the electrochemical cell with a MF; A—oscillogram of the process (beam 1—optical signal oscillations during autowaves appearance, beam 2—impulse voltage); B—photograph of the steady-state autowave process in the electrochemical cell with the MF (40 seconds after the electric field switching on); frame width is 1.2 cm

## 4. Conclusion

The properties of the electrochemical cell with transparent electrodes filled with a weakly conducting dielectric—a magnetic fluid was researched. Rectangular electric pulses were applied to the electrodes, and a polarization capacitance was calculated from the measured current in a cell with a magnetic fluid. It is established that the polarization capacity of the cell is greater than the static capacity by 3–4 orders of magnitude. This phenomenon is attributed to the formation of thin ( $\sim 100$  nm) near-electrode layers consisting of a magnetic fluid dispersed phase particles (magnetite) with a protective shell. The resistance of a cell with a magnetic fluid is calculated after the formation of near-electrode nanolayers, which is several times higher than the cell resistance before the electric impulses are applied to the electrodes. It is shown that when the voltage higher than 11 V is applied to the electrodes, the field strength in the near-electrode layer reaches a value of more than  $2.3 \cdot 10^7$  V/m, at which the layer resistance drops sharply, it becomes conductive (Wine effect). The particles from which the layer consists, repel and come into the liquid, where they are discharged and the process repeats. Local self-oscillations arise, and brightly colored autowaves can be observed near the surface of the electrode.

## References

- [1] R. E. ROSENSWEIG: *Ferrohydrodynamics*. Cambridge University Press (1985), p. 344.
- [2] V. V. CHEKANOV, N. V. KANDAUROVA, V. S. CHEKANOV: *Phase autowaves in the near-electrode layer in the electrochemical cell with a magnetic fluid*. Journal of Magnetism and Magnetic Materials 431 (2017), 38–41.
- [3] P. V. GEYDT, A. V. KUZMIN, A. G. MATVEEVA, E. V. YURTOV, T. YU. TYANGINSKII, V. V. SLEPTSOV: *Capacitance measurement of the capacitors with liquid-crystal electrolyte based on potassium laurate with silver nanoparticles*. Journal Advances in Chemistry and Chemical Technology 26 (2012), No. 7, p. 136.
- [4] V. V. CHEKANOV, N. V. KANDAUROVA, V. S. CHEKANOV: *Thickness calculation of thin transparent conductive membrane on the border with a magnetic fluid*. Journal of Nano and Electronic Physics 8 (2016), No. 4, C. 04045, p. 3.
- [5] M. BORN, E. WOLF: *Principles of optics*. Verlag Nauka, Moskau (1973).

Received October 12, 2017



# Method of determination of parameters of impact interaction by using phenomenological models

SLAVA MEBONIA<sup>1</sup>, TAMAZ MORCHADZE<sup>2,3</sup>, NUNU RUSADZE<sup>2</sup>

**Abstract.** The main rheological models describing the impact interaction of bodies in the process of elastic, viscous elastic and plastic deformation are considered. Recommendations for the choice of the type and parameters of models under different conditions of loading of interacting bodies are given. The expression of the impact velocity during which stresses in the material of bodies reach the yield point and plastic deformation arises, is determined. The phenomenological solving of problems of shock interaction involves the determination of the parameters of the force function not experimentally, but on the basis of the conclusions obtained in the study of rheological models is described. The parameters of strength function with due consideration of the character of the content (elastic, plastic) and velocity of collision, condition of the material and its physical and mechanical properties are defined. Linearization of contact rigidity from equality condition of deformation energy is done. The equation system of impact at capture of the metal by the rolls of the mill is composed and the maximum value of the force of impact is determined.

**Key words.** Force, impact, rheological model, shock parameters.

## 1. Introduction

Determination of the parameters of the impact interaction of parts is important in the calculation and design of mechanisms and machines. The main parameters of the impact are the shape of the shock pulse, the maximum contact force, the maximum deformation of the bodies, the duration of the impact, etc. These parameters depend on the laws of the shock process, the main difficulty of which is that the shock forces can be found only in connection with the study of the dynamic deformation of the bodies collided [1–3].

---

<sup>1</sup>R. Dvali Institute of Machine Mechanics, 10, Mindeli str., Tbilisi, 0186, Georgia

<sup>2</sup>Faculty of Technical Engineering, Akaki Tsereteli State University, 59 Tamara Mepe, Kutaisi, 4600 Georgia

<sup>3</sup>Corresponding author; e-mail: tamazmor@mail.ru

Since the shock forces propagate from the contact zone of the impacted bodies not instantly, but with some finite velocities, a complex stress-strain state occurs in the bodies which changes both in space and in time. In addition, the calculation of the force of impact of bodies is complicated by the fact that the physical and mechanical properties of materials are manifested differently at different loading patterns and different collision speeds.

At present well-known impact theories by Hertz, Shtaierman, also the wave impact theory are used only in case of elastic collision of the bodies. Last time in the impact theory was planned a new direction the base of which is phenomenological description of the fact. Phenomenological theory of impact, developed in the works [4, 5], allows to calculate the parameters of impact for different nature of the interaction of bodies, including for the elastic-plastic shock interaction, so the calculation methods considered here take into account the basic provisions of this theory.

## 2. Basic part

The nature of the interaction of bodies during the impact depends on many factors. Foremost among them are the relative approach velocity of bodies, their geometric shape and mechanical properties of the material. The approach velocity of bodies or the impact velocity, is determined by kinematics of the mechanism, and is derived from solution of differential equations of motion of links. Geometry of the impacting bodies is determined by their configuration and characteristic dimensions: length, diameter, height, etc. The bodies may have geometry properties representing combination of regular shapes or other configuration. Setting of body shape determines its mass, curvature in the contact area and the contact stiffness of the interacting bodies.

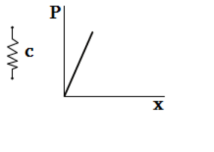
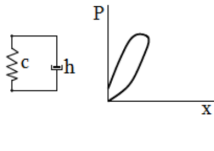
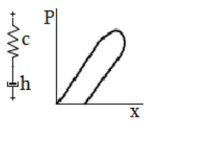
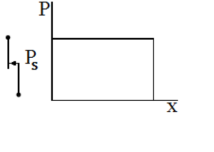
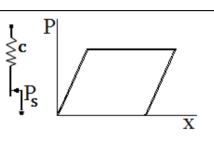
Mechanical properties of materials are determined by the correlation of rheological properties of viscosity and elasticity, plasticity, a measure of which are modulus of elasticity, viscous resistance drag coefficient, modulus of plasticity and flow limit.

Mechanical models reproducing these relationships are commonly referred to as the rheological models. Placing the rheological model between the discrete masses reproducing inertial properties of interacting bodies we can reproduce the process of force interaction of bodies during the impact. Such an approach, based on an implicit assumption about the nature of phenomena occurring during the impacts of real bodies is called phenomenological.

Mechanical models are presented in Table 1. Elastic medium is presented by Hooke's model as the spring of the elastic stiffness. The power coupling function is described by the evident ratio  $P = cx$ . If the geometrical conditions on the contact are such that the deformation force is not proportional to crumbling, for example, as in Hertz' model, the contact stiffness is considered to be nonlinear, and the power coupling function is written down as  $P = c(x) \cdot x$ .

In Foigt's model, the elements are connected in parallel, and their deformation is equal to the total deformation  $x$ , but the force  $P$  is equal to the total force imparted by each element:  $P = P_1 + P_2$ . By virtue of the fact that  $P_1 = cx$  and  $P_2 = h\dot{x}$ , the force function takes the following form:  $P = cx + h\dot{x}$ .

Table 1. Basic mechanical models

Medium	Model of medium	Scheme of a model and the diagram of deformation	Power coupling function	Model's application area
Elastic	Hooke's model		$P = cx$	Elastic impact $R = 1$
Visco-elastic	Foigt's model		$P = cx + h\dot{x}$	Not quite elastic impacts with the small velocities, without residual deformations $0 < R < 1$
	Maxwell's model		$P = h \left( \dot{x} - \frac{\dot{P}}{c} \right)$	
Plastic	Plastic-rigid model		$P = P_S, \dot{x} > 0$ $P = 0, \dot{x} < 0$	Plastic impacts $R = 0$
	Elasto-plastic model		$P = cx, \dot{x} > 0; x < x_S$ $P = P_S, \dot{x} < 0; x > x_S$ $P = c(x - x_0); \dot{x} < 0,$	Elastic impacts with the presence of plastic deformations

In Maxwell's model, the elements are series-connected, and therefore, the total deformation of model is equal to the total deformation of the each element  $x = x_1 + x_2$ . By virtue of the fact that the each model element imparts the same force  $P$ , then the components of deformation are determined by the ratios: for elastic element  $x_1 = P/c$ , but for the damper of viscous friction  $x_2 = \int \frac{dP}{h} dt$ .

For a rigid-plastic model the power coupling function in the approach phase of bodies, when  $\dot{x} > 0$ , is expressed by the formula  $P = P_S = \sigma_S F$ , where  $P_S$  and  $\sigma_S$  denote the force and stress, during which plastic deformations occur in the material,  $F$  is the contact area, depending on the value of crumbling of bodies. When unloading a rigid-plastic model with  $\dot{x} < 0$ , the power function is always zero.

An elastic-plastic model represents a series connection of models of Hooke and rigid-plastic medium. When loading reaches force  $P$ , initially the elastic element is

deformed. When the force  $P$  reaches the force  $P_S$ , then the deformation of the elastic element ceases, and the element of rubbing friction goes to work. When removing the force  $P$  on the element of rubbing friction, there is memorized deformation  $x_0$  it had reached, which is fixed in the model as a residual, after unloading the elastic element.

The choice of a particular model to describe the impact process depends primarily on the properties of bodies, their geometry and the approach velocity. Usually, the material of bodies and the impact velocity are pre-assigned. This suffices to assess the possibility of the emergence of plastic deformation in the material, and make conclusion on the alleged nature of impact. Approximately, the impact velocity during which stresses in the material of bodies reach the yield point and plastic deformation arises is determined according to the expression

$$v_S = \frac{\pi^2 \left[ \frac{4(1-\mu_1)}{E_1} + \frac{4(1-\mu_2)}{E_2} \right]^2 \sigma_{S1}^{2,5}}{32 \sqrt{10} \rho_1 e^5 (1-\mu_1)^5},$$

where  $\mu_1$  and  $\mu_2$  are the Poisson ratios,  $E_1$  and  $E_2$  are the elastic module of bodies,  $\sigma_{S1}$  and  $\rho_1$  are the yield point and the density of the material of the first body, and  $e$  stands for the coefficient that takes into account the stress state at different points of the deformable volume of bodies in the contact area. The average value of this coefficient at the contact site, according to [3], is equal to 0.436.

If the impact velocity is less than  $v_S$ , the impact is elastic or viscous-elastic and it is necessary to use the models of the elastic or viscous-elastic impact family. Otherwise, the impact will be elastic or viscous-plastic, and in order to describe the impact, the model of the plastic family should be assigned.

The criterion for the choice of plastic models of impact is a small magnitude or the absence of the elastic component of deformation in the material. In this case, virtually no post-impact bodies are bouncing off each other. The coefficient of restitution of the velocity is close to zero. The plastic models describe the impacts of soft plastics and steels at high temperatures, just about 1100–1300 °C and at the relatively small deformation velocities.

The elastic-plastic models are recommended to use for the strain-hardening materials with the developed elastic and plastic deformations at the average impact velocities, just about  $10v_S$ .

The viscoelastoplastic models are useful for modeling of impacts of plastics and elasto-plastic materials at the high impact velocities—more than  $10v_S$ .

Thus, the defining criteria for the choice of the model of impact are the velocity and the material of the impacting bodies. Moreover, for the same material, depending on the ratio, there can be applied the various models of impact.

Once the nature of impact has been determined and the type of model has been chosen, there is initiated determination of the parameters, that is, the construction of a power coupling function. The main parameters to be determined are the contact stiffness  $c$ ,  $h$  as well as the force  $P_S$ , at which the plastic flow of material begins.

There are three methods for determining these parameters:

1. Experimental method of dynamic tests of natural or their equivalent model

samples.

2. Method based on processing of diagrams – static and dynamic deformation of materials on special samples.
3. Analytical method, which is based on the fundamental concepts of the theory of elasticity and plasticity on regularities of changes in the stress-strain state of the materials of bodies in the contact problems.

Experimental method is the most accurate, because it allows for obtaining the power coupling function  $P(x, \dot{x})$  directly on the real bodies. This method requires the application of expensive equipment to register fast-moving processes. However, in some cases, this method is the only possible one.

The second method involves the use of known results of the standard on compression-tensile and deflection tests of special samples. The diagrams created properly processed on the basis of test materials contain sufficient information for approximate determination of model parameters.

Analytical method involves the use of solutions of the contact problems in various cases of force interaction of bodies. This method has several advantages compared with the previous two ones, since it does not require special experiments, and is based on the most general laws of deformation of materials. In order to obtain quantitative characteristics of interactions, there is only need for physical parameters of materials - Young's modulus, the Poisson ratio, modulus of plasticity and yield point.

In the case when the material obeys the law of rigid-plastic deformation (for example, ingot, heated to the temperature of 1000–1200 °), it is possible to apply the simplifying hypotheses and obtain the rather simple formulas based on them for approximate evaluation of stiffness.

The problem of impact is much more complicated in the presence of plastic deformation. According to the empirical Gerstner's law, elastic and plastic deformations develop independently during loading [6], i.e.

$$\delta = \delta_1 + \delta_2 = kP^{\frac{2}{3}} + \lambda P,$$

where  $\delta$  is the total deformation;  $\delta_1$  denotes the elastic deformation component and  $\delta_2$  stands for the plastic component deformation. Symbol  $k$  denotes the coefficient determined from the curvature of the bodies in the area contact and material properties and  $\lambda$  is the coefficient of proportionality.

A different approach to the problem of elastic-plastic deformation is outlined in the work [6]. Here, in the entire area of loading, the force function is given by one analytical expression:  $P = b\delta^n$ , where  $b$  is the coefficient that depends on their physical and mechanical characteristics and configurations of impacted bodies and  $n$  denotes the measure of the degree that depends on the shape of the bodies in the impact zone.

Experimental studies indicate that in the process of impact, the degree of the strength characteristic index undergoes a change that is most noticeable at the beginning of the plastic deformation process at impact. Analysis of the oscillograms of the impact forces shows that at the beginning of the shock process the dependence

of the contact force on the local crumple is linear, which corresponds to the physical representations, since at the beginning of the collision the plastic component of the local collapse is absent and there is only an elastic component of deformation.

At speeds of impact  $v_0 \leq 100$  m/s, the mechanical characteristics of the materials vary slightly, so it can be assumed that the static force characteristic of the deformable element is practically the same as the dynamic one and can be used in calculating the force of impact. The use of static power characteristics in solving the problems of impact is very convenient, because it allows you to do without complex and expensive dynamic testing of materials.

The phenomenological approach to solving problems of shock interaction involves the determination of the parameters of the force function not experimentally, but on the basis of the conclusions obtained in the study of rheological models [4, 5, 7].

The parameters of function  $P = b\delta^n$  mainly are defined by the character of the content (elastic, plastic) and depend on velocity of collision, condition of the material and its physical and mechanical properties. The index of degree  $n$  generally can be defined according to the diagram extending of the material (see Fig. 1):  $n = \tan \alpha_2 / \tan \alpha_1$ .

Coefficient  $b$  in the expression for the power function is defined according to the formula

$$b = S_\pi^n F^{n-1},$$

where  $S_\pi$  is the linearization contact rigidity of collision bodies;  $F$  – flow force.

Linearization contact rigidity one can find according to the formula [3]

$$S_\pi = 1.3k^{0.8}m^{0.2}v^{0.4},$$

where  $k$  is the coefficient of proportionality in the formula of Hertz,  $m$  denotes the given mass of the colliding bodies and  $v$  stands for the collision velocity.

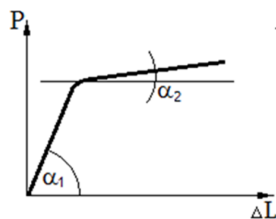


Fig. 1. Diagram of expanding material

Fluidity force can be calculated according to the formula:

$$F = \sqrt{S_\pi m} \cdot v_S,$$

where  $v_S$  denotes the velocity of collision causing first plastic shifts in the material.

During calculation of impact loads, for simplification of computation operation linearization of power communication function is made. Linearization can be realized according to different criteria: according to equality of maximum deformations or amplification in initial or finishing models, etc. In the work [9] linearization of

contact rigidity is done from equality condition of deformation energy (see scheme in Fig. 2).

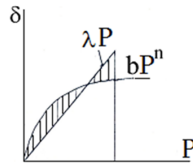


Fig. 2. Dependence of plastic deformation from amplification

$$\int_0^{\delta_{\max}} b\delta^n d\delta = \frac{b\delta_{\max}^{1+n}}{1+n} = \frac{\bar{C}\delta_{\max}^2}{2}, \quad \bar{C} = \frac{2b\delta_{\max}^{n-1}}{1+n}, \quad \lambda = \frac{1}{\bar{C}}, \quad \delta = \lambda P,$$

where  $\lambda$  is the pliability of the linearization system,  $\delta_{\max}$  denotes the quantity of maximum crushing of the edge;

$$\delta_{\max} = 0.7575 \left( \frac{mv_0^2}{K} \right)^{0.4} \frac{Q}{n_1}, \quad n_1 = \frac{v_0}{v_S}$$

where  $v_0$  is the peripheral velocity of the shafts and

$$Q = \left[ \frac{n_1}{2}(1+n) \right]^{\frac{1}{1+n}}.$$

The important stage to solve the impact load is also to construct the calculation scheme and make it convenient for research. In case of calculation of impact interaction of the metal with rolls in the moment of grip, the working rolls of the rolling mill can be given in the form of the double supporting beam with rolling mass  $m$  which collide with the body of mass  $M$  (see Fig. 3, top part). Such a scheme can be used also for the tube rolling mill at describing of impact interaction at the first grip by the rolls of the tube mill [8, 9].

At the secondary grip of the metal by the shafts of the tube rolling mill (namely, the automatic mill) takes place impact interaction in the system of sleeve-mandrel-bar. In the given case the calculation scheme can be presented in the view of coiled spring, on the one end of which is fastened mass  $M$ , and the other end rests on the rigid support (Fig. 3, bottom part). At that mass  $M$  takes impact from the movable mass  $m$ .

Correctness of substitution of the rectilinear rod of the coiled spring in the given calculation scheme is proved by investigation of the formation of rods of automatic mills carried out in laboratories of VNIMETMASH. As a result of these researches it is stated that at axial loading the rod takes the form of a spring [10].

As an example, consider the impact process in the secondary capture of metal by rolls of tube rolling mill. The scheme is shown in Fig. 4.

The peculiarity of the impact process is that the secondary capture of the work piece is clamped in the caliber of the rolls and therefore the rolls participate in the process of impact together with the conjugated parts. Therefore, the mass of the

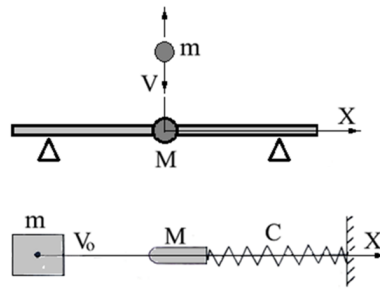


Fig. 3. Schemes of impact interaction

striking bodies can be defined from equality of kinetic energy of shafts rotation and kinetic energy of advanced motion of the mass with the given mass:

$$M = \frac{2J_0\omega}{v_0^2},$$

where  $J_0$  is the inertia moment of the roll relative to its own rotation axis,  $\omega$  denotes the roll's angular velocity and  $v_0$  stands for the collision velocity.

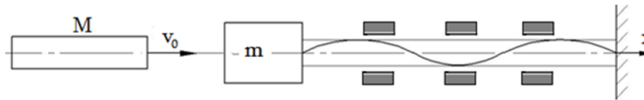


Fig. 4. Secondary capture of metal by rolls of tube rolling mill

So, in the given case the problem comes to impact of the mass body  $M$  on the elastic rod, fastened by the opposite end. At collision between the sleeve and mandrel, a contact force  $P(t)$  is produced, that from one side leads to plastic crushing of the sleeve edge  $\delta$ , and from the other side to longitudinal-cross-section oscillation of the rod, instead of which according to the adopted calculation scheme we will consider longitudinal oscillations of concentrated mass  $M$ .

The equation system of impact at capture of the metal by the rolls of the mill generally contains three equations with three unknowns, at that the third equation is a function of power connection

$$\begin{cases} M\ddot{x} + cx = P(t), \\ m\ddot{x} + m\ddot{\delta} = -P(t), \\ \delta = bP^n. \end{cases} \tag{1}$$

With the help of the expression  $\delta = \lambda P$  the initial system differential equation transforms into the differential equation with constant coefficients

$$\begin{cases} P'''' + AP'' + BP = 0, \\ A = \frac{1+\beta+\omega^2 m\delta}{m\beta\delta}, \\ \beta = \frac{\omega^2}{m\beta\delta}. \end{cases} \tag{2}$$

By solution of this equation we obtain the meaning of power function, also quantity of maximum meaning of amplification of impact.

The initial conditions for this equation are determined from the system (1) taking into account the relations  $\delta = \lambda P$ ,  $P(0) = 0$ ,  $P'(0) = \frac{v_0}{\lambda}$ ,  $P''(0) = 0$ ,  $P'''(0) = \frac{v_0}{m\lambda^2} \left(1 + \frac{1}{\beta}\right)$ .

Preliminary calculations of forces of shock interaction showed that for the parameters proper for the system „sleeve-mandrel-rod“ of the automatic mill, the roots of the characteristic equation usually are expressed in imaginary numbers. Therefore, in this paper, the method of solving the differential shock equation is analyzed in detail only for the case of imaginary roots of the characteristic equation. In such cases, the solution of the differential shock equation can be written in the following form

$$P = C_1 \cos(\lambda_1 t) + C_2 \sin(\lambda_2 t) + C_3 \cos(\lambda_3 t) + C_4 \sin(\lambda_4 t), \quad (3)$$

where  $\lambda_1$ ,  $\lambda_2$ ,  $\lambda_3$  and  $\lambda_4$  are the roots of the characteristic equation and  $C_1$ ,  $C_2$ ,  $C_3$  and  $C_4$  are the constants determined from the initial conditions.

By successive differentiation of the expression (3), taking into account the initial conditions, we find the values of the above constants:

$$C_1 = C_3 = 0, \quad C_2 = \frac{V_0}{\lambda_2(\lambda_4^2 - \lambda_2^2)\delta} \cdot \left(\lambda_2^2 - \frac{1 + \beta}{m\beta\delta}\right)$$

$$C_4 = \frac{V_0}{\lambda_4\delta} \left[1 - \frac{1}{\lambda_4^2 - \lambda_2^2} \left(\lambda_4^2 - \frac{1 + \beta}{m\beta\delta}\right)\right].$$

So, the power function will have the form of

$$P_{\max} = C_2 \sin(\lambda_2 t) + C_4 \sin(\lambda_4 t) \quad (4)$$

To determine the maximum value of the force of impact, it is necessary to find the time corresponding to the maximum of the force function and substitute it in the expression (3a), i.e.

$$P_{\max} = C_2 \sin(\lambda_2 t_{\max}) + C_4 \sin(\lambda_4 t_{\max}).$$

Practical calculations by this method, carried out for the case of rolling pipes D127x4 from steel 10 on automatic mill of pipe rolling unit 140, showed that the maximum value of the impact force is about 31.5 tons. According to the reference data, the axial force on the rod of automatic mill during the oral rolling process for the same pipe size is 24 tons, so that the maximum impact force is about 1.3 times higher than this value.

### 3. Conclusions

1. At calculation of impact load in tube mills consideration of plastic deformation is realized by corresponding choice of the function of power connection of the

interacting elements.

2. Linearization of the function of power connection significantly simplifies calculations of the impact load.

3. Choice of the model for description of the impact process depends on the character of the collision properties of the material of colliding bodies and velocity of their reciprocal motion.

## References

- [1] K. CHENG: *Machining dynamics*. Springer Science & Business Media (2008).
- [2] EDITOR A. N. EVGRAFOV: epmhAdvances in Mechanical Engineering. Selected Contributions from the Conference “Modern Engineering: Science and Education”, June 20–21, 2013, Saint Petersburg, Russia, <http://www.springer.com/in/book/9783319156835>.
- [3] EDITOR S. SEETHARAMAN: epmhFundamentals of metallurgy. Woodhead Publishing in Materials, Cambridge, England (2005).
- [4] X. L. J. SEYKENS: *Development and validation of a phenomenological diesel engine combustion model*. Dissertation thesis, University of Eindhoven, Netherlands (2010).
- [5] P. LAKSHMINARAYANAN, Y. AGHAV: *Phenomenology of diesel combustion and modelling*. Modelling Diesel Combustion. Mechanical Engineering Series. Springer, Dordrecht (2010).
- [6] G. S. BATUEV, JU. V. GOLUBKOV, A. K. EFREMOV: *Engineering methods of researching impact processes*. Leningrad (1977). In Russian.
- [7] G. MIKULOWSKI, M. FOURNIER, T. PORCHEZ, C. BELLY, F. CLAEYSSSEN: *Semi-passive vibration control technique via shunting of amplified piezoelectric actuators*. Proc. 15th International Conference on New Actuators (ACTUATOR 2016), 13–15 June 2016, Bremen, Germany, 542–546.
- [8] A. L. IGUMNOV, S. V. METRIKIN, V. I. NIKIFOROVA: *The dynamics of eccentric vibration mechanism*. Journal of Vibroengineering 19 (2017), No. 7, 4854–4865.
- [9] A. S. GVOZDEV, V. S. MELENTJEV: *Control of elastic-hysteretic characteristics of multilayer all-metal vibration insulators with structural damping*. Journal of Vibroengineering 19 (2017), No. 5, 3178–3190.
- [10] V. P. ANISIFOROV, A. U. GRINDSPUN: *Analysis of the force acting on the rod of automatic rolling mill*. VNIIMETMASH, N 29. Moscow, Metallurgy (1970). In Russian.

Received May 15, 2018

# Finite-time convergence of gradient-based neural network for solving Lyapunov matrix equation<sup>1</sup>

SHIHENG WANG<sup>2</sup>, SHIDONG DAI<sup>3</sup>, KE WANG<sup>3,4</sup>

**Abstract.** With a new type of activation function — Li activation function, the gradient-based neural network (GNN) is established to solve Lyapunov matrix equation. In this case, the theoretical analysis shows that GNN can converge in finite time, while it can converge only in infinite time with conventional activation functions, such as linear and power-sigmoid. Numerical results confirm that GNN with Li activation function can not only globally converge to the solution of the Lyapunov matrix equation but also converge in finite time, compared with the conventional two activation functions.

**Key words.** Gradient-based neural network, global convergence, finite-time convergence, Lyapunov matrix equation, online solution, activation function

## 1. Introduction

The applications of Lyapunov (or Lyapunov-like) matrix equation exist widely in many different engineering and scientific computing areas, such as linear algebra [1], control theory [2], boundary value problem [3], signal processing [4] and optimization [5].

With the development of neural networks theory [6, 7], more and more authors use neural networks approaches for solving linear systems and matrix equations. To construct a neural network, the first and foremost thing is to define a scalar-valued norm-based energy function. The minimum point (it is generally a global minimum) of the energy function corresponds to the solution of the original problem. Then one should minimize the energy function. The most common method is to find the

---

<sup>1</sup>Supported by National Natural Science Foundation of China (11301330) and “Gaoyuan Discipline of Shanghai – Mathematics, Shanghai City, China”

<sup>2</sup>Nanyang Vocational College of Agriculture, Nanyang 473000, China

<sup>3</sup>Department of Mathematics, College of Sciences, Shanghai University, Shanghai 200444, China

<sup>4</sup>Corresponding author; e-mail: kwang@shu.edu.cn

negative gradient direction. Therefore, in [8], the gradient-based neural network (GNN) model was proposed for solving Lyapunov matrix equation. And the authors of [9] improved the GNN model by using different activation functions, and indicated that the GNN model without activation function is equivalent to the improved GNN model with linear activation function. They also proved that the improved GNN model with power-sigmoid activation function has a superior convergence. But the improved GNN model with the suggested activation functions never converges to the accurate value in finite time.

In this paper, the improved GNN model is suggested for solving the Lyapunov matrix equation with a new activation function referred to Li activation function which was suggested in [10]. This improved GNN model was included in the proceedings of the 4th International Conference on Information Technology and Management Innovation (ICITMI 2015) [11]. Here, the details of this model are presented. The global convergence, finite-time convergence and the upper bound of the convergent time are provided. Computer simulations are given to demonstrate the theory.

The remainder of the paper is organized as follows. Section 2 introduces the background of Lyapunov matrix equation. Section 3 gives the detail of the GNN model for solving Lyapunov matrix equation, and four conventional types of activation functions and Li activation function are also introduced in this section. In Section 4 it is proved that the improved GNN model with Li activation function can converge to the exact solution of the Lyapunov matrix equation asymptotically. A theorem is also given in this section to show the finite-time convergence of the improved GNN model with LI activation function. Section 5 gives the numerical results. Finally, in Section 6, the conclusion is presented.

## 2. Lyapunov matrix equation

In scientific and engineering areas, it is crucial to analyze the stability of given systems. For the linear time-invariant (LTI) dynamical control system, a host of methods have been put forward to analyze its stability, such as Nyquist method [12] and Routh-Hurwitz method [13]. However, these methods are not effective enough to deal with the nonlinear dynamical control systems. Instead, Lyapunov methods are effective approaches to handle various kinds of nonlinear and linear systems. Below, a simple example is introduced to show how Lyapunov method works to analyze the stability of the LTI dynamical control system.

Consider a continuous-time linear autonomous system

$$\dot{x}(t) = Ax(t), \quad x(t_0) = x_0 \in \mathbb{R}^n, \quad (1)$$

where  $x(t)$  is a state vector and  $A \in \mathbb{R}^{n \times n}$  is the coefficient matrix. The matrix  $A$  is called stable (also Hurwitz or negative stable in the literature) if all its eigenvalues have negative real parts. If  $A$  is stable, the equilibrium of linear system [1] is unique and such a system is asymptotically stable. Then the system is asymptotically stable is equivalent to  $A$  is stable. To check the stability of system [1], the first and foremost

is to build an energy function (also called Lyapunov function)

$$V(x) = x^T P x, \quad (2)$$

here  $P \in \mathbb{R}^{n \times n}$  is a symmetric positive definite matrix. Then the time derivative of the Lyapunov function is

$$\frac{dV}{dt} = \frac{dV(x)}{dx(t)} \frac{dx(t)}{dt} = \dot{x}^T P x + x^T P \dot{x} = x^T (A^T P + P A) x, \quad (3)$$

defining

$$A^T P + P A = -C, \quad (4)$$

where  $C$  is a symmetric positive definite matrix. Eq. (4) is the well-known Lyapunov matrix equation.

Solving Lyapunov matrix equation is an important approach for checking the stability of  $A$ . To check the positive definiteness of  $P$ , the following theorem is needed.

**Theorem 2.1** [14]: A matrix  $A \in \mathbb{R}^{n \times n}$  is stable if and only if there exists a positive definite solution to the Lyapunov matrix equation (4) where  $C$  is a symmetric positive definite matrix.

In (4),  $C$  is often chosen as identity matrix. With Theorem ??, checking the stability for an arbitrary matrix  $A \in \mathbb{R}^{n \times n}$  is transferred to the simpler problem of checking positive definiteness for a symmetric matrix  $P$ . Moreover, the following theorem guarantees the existence and uniqueness of  $P$  to Lyapunov matrix equation (4).

**Theorem 2.2** [15]: The necessary and sufficient condition for the existence of a unique solution of Lyapunov matrix equation (4) is that no two eigenvalues of matrix  $A \in \mathbb{R}^{n \times n}$ ,  $\lambda_i(A)$  and  $\lambda_j(A)$ ,  $i, j = 1, 2, \dots, n$ , add up to zero for any time. In mathematics.

$$\lambda_i(A) + \lambda_j(A) \neq 0, \text{ for all } \lambda_i(A), \lambda_j(A) \in \delta(A), i, j = 1, 2, \dots, n, \quad (5)$$

where  $\lambda_i(A)$  denotes the  $i$ th eigenvalue of matrix  $A$ , and  $\delta(A)$  denotes the eigenvalues set of matrix  $A$ .

### 3. Gradient-based neural network (GNN) model

Consider the Lyapunov matrix equation

$$A^T X + X A = -C, \quad (6)$$

where  $A \in \mathbb{R}^{n \times n}$  is the coefficient matrix, and  $C \in \mathbb{R}^{n \times n}$  is positive definite. According to the traditional gradient-based algorithm, the first and foremost is to define

an energy function  $\varepsilon(X)$  based on a nonnegative scalar-valued norm:

$$\varepsilon(X) = \frac{\|A^T X + X A + C\|_F^2}{2}, \quad (7)$$

where  $\|\cdot\|_F$  denotes the Frobenius matrix norm, i.e.,  $\|A\|_F = \sqrt{\text{trace}(A^T A)}$ , and  $\text{trace}(A^T A)$  is the trace of  $A^T A$ . Thus, it follows

$$\varepsilon(X) = \frac{\text{trace}((A^T X + X A + C)^T (A^T X + X A + C))}{2}. \quad (8)$$

With the basic differential properties of the trace of a product matrix  $PZQ$ :

$$\frac{\partial \text{trace}(PZQ)}{\partial Z} = P^T Q^T, \quad \frac{\partial \text{trace}(PZ^T Q)}{\partial Z} = QP, \quad (9)$$

where  $P$ ,  $Z$  and  $Q$  are arbitrary matrices with appropriate order, the following can be obtained

$$\frac{\partial \varepsilon(X)}{\partial X} = A(A^T X + X A + C) + (A^T X + X A + C)A^T. \quad (10)$$

By evolving along the negative gradient of such an energy function  $\varepsilon(X)$ , the following classical GNN model is taken

$$\dot{X}(t) = -\Gamma(A(A^T X + X A + C) + (A^T X + X A + C)A^T), \quad (11)$$

where  $\Gamma$  is a positive definite matrix, and the time varying matrix  $X(t)$ , starting from an initial condition  $X_0 = X(0) \in \mathbb{R}^{n \times n}$ , is the activated state matrix corresponding to the theoretical solution  $X^*(t)$  of (6). Usually  $\Gamma$  is simply taken as  $\gamma I$  with constant scalar  $\gamma > 0$  and  $I$  is identity matrix. And  $\gamma$  should be set as large as the hardware permit and is generally used to scale the convergence rate [16].

Nonlinearity always exists even if the linear activation function is used. The nonlinear phenomenon may appear in the hardware implementation, e.g., in digital realization due to truncation and round-off errors. Inspired by this, in 2005, Zhang et al. combined four kinds of activation functions with the ZNN model [17]. In [9], to solve the Lyapunov matrix equation the author added the four kinds of activation functions to the classical GNN model, where the author called the new GNN model the improved GNN model. Here is the improved GNN model,

$$\dot{X}(t) = -\Gamma(A\mathcal{F}(A^T X + X A + C) + \mathcal{F}(A^T X + X A + C)A^T), \quad (12)$$

where  $\mathcal{F}(\cdot)$  is a function of matrix, defined as follows:

$$\mathcal{F}(A) = f(a_{ij}), A \in \mathbb{R}^{n \times n}, i, j = 1, 2, \dots, n. \quad (13)$$

The following is the four kinds of activation functions:

1. linear activation function  $f(x) = x$ ;

2. bipolar sigmoid activation function  $f(x) = (1 - \exp(-\xi x)) / (1 + \exp(-\xi x))$  with  $\xi \geq 2$ ;
3. power activation function  $f(x) = x^p$  with odd integer  $p \geq 3$ ;
4. power-sigmoid activation function

$$f(x) = \begin{cases} x^p, & |x| \geq 1, \\ \frac{1 + \exp(-\xi)}{1 - \exp(-\xi)} \cdot \frac{1 - \exp(-\xi x)}{1 + \exp(-\xi x)}, & |x| < 1, \end{cases} \quad (14)$$

with suitable design parameters  $\xi \geq 2$  and  $p \geq 3$ .

In [9], the author proved that with the linear and the power-sigmoid activation functions the GNN model [12] can converge to the solution of the Lyapunov matrix equation globally. But how to find the accurate solution to the Lyapunov matrix equation with the GNN model [12] in finite time? In the remainder of this paper, we will combine a new activation function, presented in 2013 [10] and referred to Li activation function, to the GNN model [12]. Both theoretical analysis and numerical simulation show that when using GNN model [12] with this type of activation function to solve the Lyapunov matrix equation, the state matrix  $X(t)$  can converge to the accurate solution in finite time. Here is the Li activation function

$$f(x) = \frac{1}{2} \text{sig}^r(x) + \frac{1}{2} \text{sig}^{\frac{1}{r}}(x), \quad (15)$$

where  $x \in \mathbb{R}$ ,  $r > 0$  is a parameter. The function  $\text{sig}^r(x)$  is defined as follows

$$\text{sig}^r(x) = \begin{cases} |x|^r, & \text{if } x > 0, \\ 0, & \text{if } x = 0, \\ -|x|^r, & \text{if } x < 0. \end{cases} \quad (16)$$

For the Li activation function defined in [15] and [16], it is easy to see that for a positive constant  $\rho$ , the case  $r = \rho$  is always same to the case  $r = 1/\rho$ . Then it is only needed to consider the Li activation function with  $0 < r \leq 1$  or  $r \geq 1$  without loss of generality. The Li activation function with different  $r \geq 1$  is shown in Fig. 1. From the figure, it can be seen that the Li activation function is reduced to the linear activation function when  $r = 1$ , and for  $|x| \gg 1$  with  $r$  increasing, the Li activation function approaches  $\frac{1}{2} \text{sig}(x)$ .

#### 4. Global convergence and finite-time convergence

It is easy to see that both  $\text{sig}^r(x)$  and  $\text{sig}^{\frac{1}{r}}(x)$  are monotonically increasing odd functions. Then it can be said that the Li activation function  $f(x) = \frac{1}{2} \text{sig}^r(x) + \frac{1}{2} \text{sig}^{\frac{1}{r}}(x)$  is a monotonically increasing odd function, thus the following theorem holds:

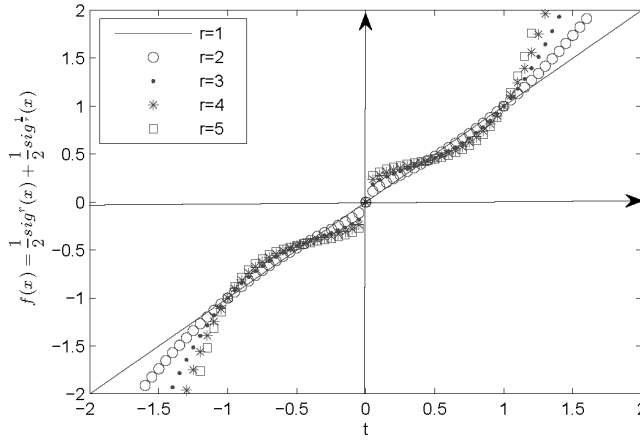


Fig. 1. The Li activation function at  $r = 1, r = 2, r = 3, r = 4$  and  $r = 5$

**Theorem 4.1** If Theorem 2.2 is satisfied,  $X^*$  is the unique solution of Lyapunov matrix equation (6). By using the GNN model (12) with Li activation function, the state matrix  $X(t)$  starting from any initial state  $X_0$  always converges to  $X^*$ .

To prove this theorem, the following two definitions of Kronecker product and vectorization should be given.

1. In a general situation, for given matrices  $A = [a_{ij}] \in \mathbb{R}^{m \times n}$  and  $B = [b_{ij}] \in \mathbb{R}^{p \times q}$ , the Kronecker product of  $A$  and  $B$ , denoted by  $A \otimes B$ , is defined as the following block matrix

$$A \otimes B = \begin{pmatrix} a_{11}B & \cdots & a_{1n}B \\ \vdots & \vdots & \vdots \\ a_{m1}B & \cdots & a_{mn}B \end{pmatrix} \in \mathbb{R}^{mp \times nq}, \tag{17}$$

which is also known as the direct product or tensor product. Note that, in general,  $A \otimes B \neq B \otimes A$ . Specially,  $I \otimes A = \text{diag}(A, A, \dots, A)$ .

2. In a general situation,  $X = [x_{ij}] \in \mathbb{R}^{m \times n}$  can be changed to a column  $\text{vec}(X) \in \mathbb{R}^{mn \times 1}$ , where  $\text{vec}(X)$  is called vectorization and defined as

$$\text{vec}(X) = [x_{11}, \dots, x_{m1}, x_{12}, \dots, x_{m2}, \dots, x_{1n}, \dots, x_{mn}]^T. \tag{18}$$

With the definitions of Kronecker product and vectorization, it is possible to change a matrix equation to a general system of linear equations. For instance,  $AXB = C$ , where  $A \in \mathbb{R}^{m \times m}, B \in \mathbb{R}^{n \times s}, C \in \mathbb{R}^{m \times s}$ , can be changed to  $Gx = c$ , where  $G = A \otimes B^T, x = \text{vec}(X), c = \text{vec}(c)$ .

**Proof of Theorem 4.1.** First, change the GNN model (12) to the following

(for the sake of simplicity, argument  $t$  is dropped hereafter),

$$\begin{aligned} \text{vec}(\dot{X}) &= -\gamma((A \otimes I)\mathcal{F}((A^T \otimes I)\text{vec}(X) + (I \otimes A^T)\text{vec}(X) + \text{vec}(C)) \\ &\quad + (I \otimes A)\mathcal{F}((A^T \otimes I)\text{vec}(X) + (I \otimes A^T)\text{vec}(X) + \text{vec}(C))) \\ &= -\gamma((A \oplus A)\mathcal{F}((A^T \oplus A^T)\text{vec}(X) + \text{vec}(C))), \end{aligned} \quad (19)$$

where

$$A \oplus A = A \otimes I + I \otimes A, \quad (20)$$

$$A^T \oplus A^T = A^T \otimes I + I \otimes A^T, \quad (21)$$

$$(A \oplus A)^T = A^T \oplus A^T. \quad (22)$$

Denoted by  $M = A^T \oplus A^T$ ,  $M^T = A \oplus A$ ,  $y = \text{vec}(X)$ , Eq.(19) is changed to

$$\dot{y} = -\gamma M^T \mathcal{F}(My + \text{vec}(C)). \quad (23)$$

By defining solution error  $\tilde{y} = y - \text{vec}(X^*)$ , the following is obtained

$$\dot{\tilde{y}} = -\gamma M^T \mathcal{F}(M\tilde{y}). \quad (24)$$

Then a candidate Lyapunov function is defined as  $V(\tilde{y}(t), t) = \frac{\|\tilde{y}\|_2^2}{2} = \frac{\tilde{y}^T \tilde{y}}{2}$ . It is easy to see that  $V(\tilde{y}) > 0$  if  $\tilde{y} > 0$ ,  $V(\tilde{y}) = 0$  if and only if  $\tilde{y} = 0$  and  $V(\tilde{y}) \rightarrow \infty$  when  $\|\tilde{y}\|_2 \rightarrow \infty$ . For the system (16), the time derivation of  $V(\tilde{y})$  is

$$\dot{V} = \frac{dV}{dt} = \tilde{y}^T \dot{\tilde{y}} = -\gamma (M\tilde{y})^T \mathcal{F}(M\tilde{y}), \quad (25)$$

$$= -\gamma \sum_{k=1}^{n^2} [M\tilde{y}]_k f([M\tilde{y}]_k). \quad (26)$$

Because Li activation function is an odd monotonically increasing function, it has these properties: (i)  $f(-u) = -f(u)$ , (ii) if  $u > 0$ ,  $f(u) > 0$ . It is also known that  $\gamma$  is a positive constant and  $M$  is a nonsingular matrix. The following conclusions are easily obtained:  $\dot{V}(\tilde{y}) < 0$  as  $\tilde{y} \neq 0$ ;  $\dot{V}(\tilde{y}) = 0$  if and only if  $\tilde{y} = 0$ .

By Lyapunov stability theory,  $\tilde{y} = 0$  is globally asymptotically stable, i.e., as  $t \rightarrow \infty$ ,  $\tilde{y} \rightarrow 0$  and  $\tilde{y} = 0$  means  $\tilde{y}(t) = \text{vec}(X^*)$ .

The proof is completed.

The following theorem shows that by using the GNN model (12) with Li activation function the exact solution to the Lyapunov matrix equation can be obtained in finite time.

**Theorem 4.2** If Theorem 2.2 is satisfied.  $X^*$  is the unique solution of Lyapunov matrix equation (6). By using the GNN model (12) with Li activation function with  $0 < r < 1$ , the state matrix  $X(t)$  could converge to the exact solution  $X^*$  in finite time  $t < \frac{\|X_0 - X^*\|_F^{1-r}}{\gamma(1-r)(\frac{\alpha}{n})^{r+1}}$ , where  $X_0$  is the initial state matrix,  $\alpha$  is the minimum eigenvalue of matrix  $M = A^T \oplus A^T$  and  $n$  is the order of matrix  $A$ .

**Proof of Theorem 4.2.** Based on the Eq.(24) and the Li activation function

$f(x)$ , the following holds:

In the case  $[M\tilde{y}]_k \geq 0$ ,

$$\dot{V} = -\gamma \sum_{k=1}^{n^2} [M\tilde{y}]_k ([M\tilde{y}]_k^r + [M\tilde{y}]_k^{\frac{1}{r}}), \tag{27}$$

$$= -\gamma \sum_{k=1}^{n^2} ([M\tilde{y}]_k^{r+1} + [M\tilde{y}]_k^{\frac{1}{r}+1}). \tag{28}$$

In the case  $[M\tilde{y}]_k < 0$ ,

$$\dot{V} = -\gamma \sum_{k=1}^{n^2} -|[M\tilde{y}]_k| (-|[M\tilde{y}]_k|^r - |[M\tilde{y}]_k|^{\frac{1}{r}}), \tag{29}$$

$$= -\gamma \sum_{k=1}^{n^2} (|[M\tilde{y}]_k|^{r+1} + |[M\tilde{y}]_k|^{\frac{1}{r}+1}). \tag{30}$$

These two cases can be combined the following equation

$$\dot{V} = -\gamma \sum_{k=1}^{n^2} (([M\tilde{y}]_k^2)^{\frac{r+1}{2}} + ([M\tilde{y}]_k^2)^{\frac{\frac{1}{r}+1}{2}}). \tag{31}$$

Suppose  $[M\tilde{y}]_j^2$  is the maximum element of vector  $M\tilde{y}$ , then

$$\dot{V} = -\gamma \sum_{k=1}^{n^2} (([M\tilde{y}]_k^2)^{\frac{r+1}{2}} + ([M\tilde{y}]_k^2)^{\frac{\frac{1}{r}+1}{2}}) \tag{32}$$

$$\leq -\gamma \sum_{k=1}^{n^2} ([M\tilde{y}]_k^2)^{\frac{r+1}{2}} \tag{33}$$

$$\leq -\gamma ([M\tilde{y}]_j^2)^{\frac{r+1}{2}} \tag{34}$$

$$\leq -\gamma \left( \sum_{k=1}^{n^2} \frac{[M\tilde{y}]_k^2}{n^2} \right)^{\frac{r+1}{2}} \tag{35}$$

$$= -\gamma n^{-(r+1)} \left( \sum_{k=1}^{n^2} [M\tilde{y}]_k^2 \right)^{\frac{r+1}{2}}. \tag{36}$$

The proof of Theorem 4.1 indicates that  $M$  is nonsingular. Assume  $\alpha$  is the minimum of  $|\lambda_i(M)|$ , then

$$\dot{V} \leq -\gamma n^{-(r+1)} \left( \sum_{k=1}^{n^2} [M\tilde{y}]_k^2 \right)^{\frac{r+1}{2}} \quad (37)$$

$$= -\gamma n^{-(r+1)} ((M\tilde{y})^\top (M\tilde{y}))^{\frac{r+1}{2}} \quad (38)$$

$$\leq -\gamma n^{-(r+1)} \alpha^{r+1} (\|\tilde{y}\|_2^2)^{\frac{r+1}{2}} \quad (39)$$

$$= -2^{\frac{r+1}{2}} \gamma \left( \frac{\alpha}{n} \right)^{r+1} V^{\frac{r+1}{2}}. \quad (40)$$

Solving the differential inequality  $\dot{V} \leq -2^{\frac{r+1}{2}} \gamma \left( \frac{\alpha}{n} \right)^{r+1} V^{\frac{r+1}{2}}$  with the initial condition  $V_0 = \frac{\|y_0 - \text{vec}(X^*)\|_2^2}{2} = \frac{\|X_0 - X^*\|_F^2}{2}$ , the following inequalities hold

$$V^{-\frac{r+1}{2}} \dot{V} \leq -2^{\frac{r+1}{2}} \gamma \left( \frac{\alpha}{n} \right)^{r+1}, \quad (41)$$

$$\int_0^t V^{-\frac{r+1}{2}} \dot{V} dt \leq \int_0^t -2^{\frac{r+1}{2}} \gamma \left( \frac{\alpha}{n} \right)^{r+1} dt, \quad (42)$$

$$V^{\frac{1-r}{2}}(t) \leq V^{\frac{1-r}{2}}(0) - 2^{\frac{r-1}{2}} (1-r) \gamma \left( \frac{\alpha}{n} \right)^{r+1} t. \quad (43)$$

As  $V(t)$  is defined to be a Lyapunov function, it is easy to see  $\forall t \geq 0, V(t) \geq 0$ . Then the following conclusion holds:

$$V(t) \begin{cases} \geq 0, & \text{if } 0 \leq t \leq \frac{\|X_0 - X^*\|_F^{1-r}}{\gamma(1-r)\left(\frac{\alpha}{n}\right)^{r+1}}, \\ = 0, & \text{if } t > \frac{\|X_0 - X^*\|_F^{1-r}}{\gamma(1-r)\left(\frac{\alpha}{n}\right)^{r+1}}. \end{cases} \quad (44)$$

Here  $V(t) = 0$  means  $X(t) = X^*$ . Then it can be said that  $X(t)$  converges to the exact solution  $X^*$  in finite time  $t = \frac{\|X_0 - X^*\|_F^{1-r}}{\gamma(1-r)\left(\frac{\alpha}{n}\right)^{r+1}}$ .

It completes the proof.

**Remark.** If  $r > 1$ , similarly, an upper bound of the convergence time can also be obtained. However, by the definition of Li activation function,  $r \geq 1$  and  $0 < r < 1$  is same. So it is only need to consider  $0 < r < 1$  or  $r > 1$ . And in either case, the convergence time  $t$  has the same supremum which is smaller than the upper bound obtained in Theorem 4.2.

## 5. Illustrative example

For illustration and comparison, consider Lyapunov matrix equation (6) with the following coefficients (which is the same as Example 4.9 in [16])

$$A = \begin{pmatrix} 0 & 1 & 0 \\ 0 & 0 & 1 \\ -1 & -2 & -3 \end{pmatrix}. \quad (45)$$

Taking  $C$  as an identity matrix, if the routine  $X = \text{lyap}(A^T, C)$  is used, the theoretical solution can be obtained:

$$X^* = \begin{pmatrix} 2.3 & 2.1 & 0.5 \\ 2.1 & 4.6 & 1.3 \\ 0.5 & 1.3 & 0.6 \end{pmatrix}. \quad (46)$$

Figure 2 depicts a typical trajectory of  $X(t)$  using the GNN model (12) with Li activation function and  $r = 1/3, \gamma = 10$ .

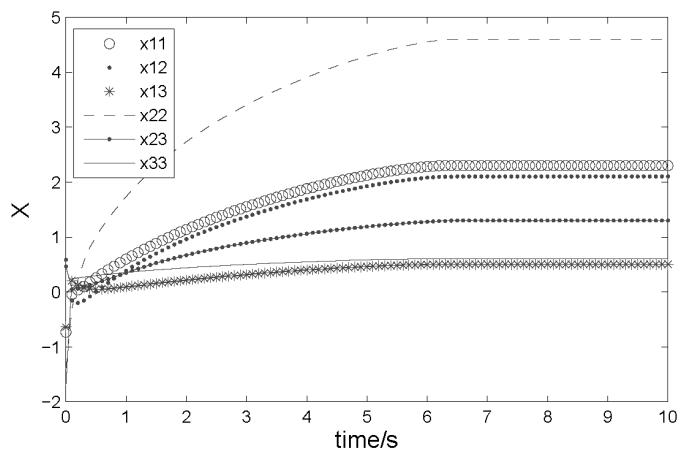


Fig. 2. Evolution of  $X(t)$  with respect to time for the improved GNN model (12) with Li activation function and  $r = 3$

By the global convergence (Theorem 4.1), the initial matrix  $X_0$  is randomly generated within  $[-2, 2]_{3 \times 3}$ . As  $X^*$  is a symmetric matrix, here we only need to display  $x_{11}(t)$ ,  $x_{12}(t)$ ,  $x_{13}(t)$ ,  $x_{22}(t)$ ,  $x_{23}(t)$ ,  $x_{33}(t)$ . From this figure, it can be observed that the neural network output  $X(t)$  reaches the exact solution  $X^*$  in a period of time (approximately 6 seconds which should be close to the supremum). This shows the finite-time convergence.

Figure 3 depicts the finite-time convergence of GNN model (12) with Li activation function which is compared with the GNN model (12) with the linear and power-

sigmoid functions, where  $r = 1/3, p = 3, \xi = 4, \gamma = 10$  and

$$X_0 = \begin{pmatrix} 0.1 & 0.1 & 0.1 \\ 0.1 & 0.1 & 0.1 \\ 0.1 & 0.1 & 0.1 \end{pmatrix}, \quad (47)$$

and the error is defined as  $\|X(t) - X^*\|_F$ .

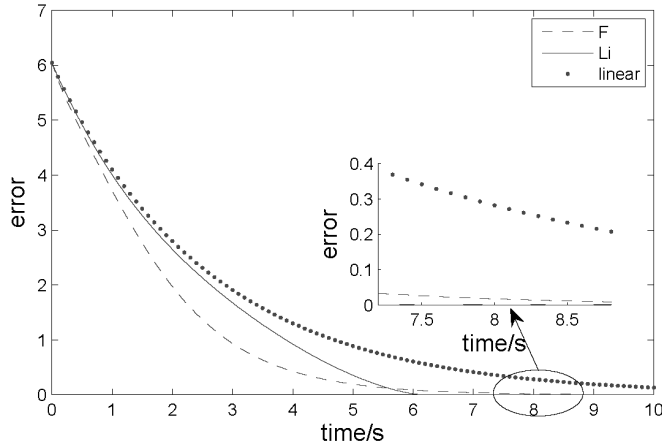


Fig. 3. Comparisons of the improved GNN model (12) with different activation functions

From this figure, it can be observed that the GNN model (12) with Li activation function can converge to the exact solution in about 6 seconds (The upper bound is about 14.4 seconds by Theorem 4.2) compared to the GNN model (12) with the linear and power-sigmoid activation functions which can converge to the exact solution only in infinite time. In contrast, the GNN model (12) with power-sigmoid and linear activation functions still have a relative large error at  $t = 6$ . It is also seen that at the end of the simulation the GNN model (12) with power-sigmoid and linear activation functions still can't return the true solution  $X^*$ .

Figure 4 shows the comparison of the GNN model with the Li activation function and  $r = 1/2, r = 1/3, r = 1/4$  and  $r = 1/5$ . It can be seen that when  $0 < r < 1$  a faster convergence rate can be obtained with  $r$  decreasing.

## 6. Conclusion

In this paper, Li activation function is combined with the GNN model for solving Lyapunov matrix equation. Compared with traditional activation functions such as the linear and power-sigmoid activation functions, the GNN model with Li activation function can converge to the exact solution of Lyapunov matrix equation in finite time. Also, the global convergence and finite time convergence are analyzed and proved. The upper bound of the convergence time is also given. Numerical example

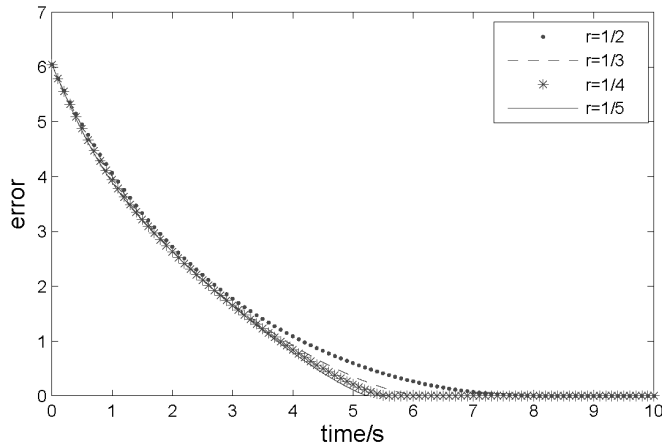


Fig. 4. Comparisons of the improved GNN model (12) with the Li activation functions with different  $r$

illustrates the global convergence and finite time convergence.

## References

- [1] T. J. LAFFEY, H. SMIGOC: *Sufficient conditions on commutators for a pair of stable matrices to have a common solution to the Lyapunov equation*. *SIAM Journal on Matrix Analysis and Applications* 31 (2010), No. 4, 2017–2028.
- [2] H. BOUZAOUACHE, N. B. BRAIEK: *On the stability analysis of nonlinear systems using polynomial Lyapunov functions*. *Mathematics and Computers in Simulation* 76 (2008), No. 5–6, 316–329.
- [3] N. TANAKA, H. IWAMOTO: *Active boundary control of an Euler–Bernoulli beam for generating vibration-free state*. *Journal of Sound and Vibration* 304 (2007), No. 3–5, 570–586.
- [4] J. C. TRIGEASSOU, N. MAAMRI, J. SABATIER, A. OUSTALOUP: *A Lyapunov approach to the stability of fractional differential equations*. *Signal Processing* 91 (2011), No. 3, 437–445.
- [5] E. J. CANDÉS, B. RECHT: *Exact matrix completion via convex optimization*. *Foundations of Computational Mathematics* 9 (2009), No. 6, 717–772.
- [6] L. WU, Z. FENG, J. LAM: *Stability and synchronization of discrete-time neural networks with switching parameters and time-varying delays*. *IEEE Transactions on Neural Networks and Learning Systems* 24 (2013), No. 12, 1957–1972.
- [7] L. XIAO, L. BOLIN: *A convergence-accelerated Zhang neural network and its solution application to Lyapunov equation*. *Neurocomputing* 193 (2016), 213–218.
- [8] D. GUO, C. YI, Y. ZHANG: *Zhang neural network versus gradient-based neural network for time-varying linear matrix equation solving*. *Neurocomputing* 74 (2011), No. 17, 3708–3712.
- [9] C. YI, Y. CHEN, Z. LU: *Improved gradient-based neural networks for online solution of Lyapunov matrix equation*. *Information Processing Letters* 111 (2011), No. 16, 780–786.
- [10] S. LI, S. CHEN, B. LIU: *Accelerating a recurrent neural network to finite-time conver-*

- gence for solving time-varying Sylvester equation by using a sign-bi-power activation function. *Neural Processing Letters* 37 (2013), No. 2, 189–205.
- [11] S. WANG, S. DAI, K. WANG: *Gradient-based neural network for online solution of Lyapunov matrix equation with Li activation function*. International Conference on Information Technology and Management Innovation, Shenzhen, China, September 2015, Proceedings ICITM, Series: Advances in Computer Science Research 28 (2015), 955–959.
  - [12] F. HAAS, G. MANFREDI, J. GOEDERT: *Nyquist method for Wigner-Poisson quantum plasmas*. *Physical Review E* 64 (2001), No. 2, paper 026413.
  - [13] M. T. HO, A. DATTA, S. P. BHATTACHARYYA: *An elementary derivation of the Routh-Hurwitz criterion*. *IEEE Transactions on Automatic Control* 43 (1998), No. 3, 405–409.
  - [14] Z. GAJIC, M. T. J. QURESHI: *Lyapunov matrix equation in system stability and control*. Academic Press, San Diego 195 (1995).
  - [15] C. YI, Y. ZHANG, D. GUO: *A new type of recurrent neural networks for real-time solution of Lyapunov equation with time-varying coefficient matrices*. *Mathematics and Computers in Simulation* 92 (2013), 40–52.
  - [16] C. MEAD, M. ISMAIL: *Analog VLSI implementation of neural systems*. Springer, Series: Springer International Series in Engineering and Computer Science 80 (1989).
  - [17] Y. ZHANG, S. S. GE: *Design and analysis of a general recurrent neural network model for time-varying matrix inversion*. *IEEE Transactions on Neural Networks* 16 (2005), No. 6, 1477–1490.

Received February 16, 2018



# The analysis of high-strength concrete slump and strength based on GA-SVM<sup>1</sup>

QIANG LI<sup>2,3</sup>, XIAOFENG LIU<sup>4,5</sup>

**Abstract.** This paper proposes a support vector machine with genetic algorithm optimized parameters for predicting of high-strength concrete (HSC) slump and strength. The rules of strength variation with time and slump variation with the level are found through creating a support vector machine (SVM) model. The experimental result presents that this method supports nonlinear prediction comparing with the partial least square regression (PLSR) and computes more precise through less sample training comparing with BP. In addition, the variation rule of HSC in a deeper level is obtained according to the analysis of the fitting function.

**Key words.** High-strength concrete, slump, compressive strength, SVM, genetic algorithm; BP network, PLSR.

## 1. Introduction

Compressive strength and slump are the main causes to contribute to the performance indicators of concrete structure [1]. Generally, slump and strength of concrete are assessed in 28th day as performance reference. By our analysis, the performance of high-strength concrete variation with its own characteristics is different from ordinary concrete.

Many experiments and analytical methods have been used to predict the slump and strength of high-strength concrete (HSC), where multi-variables linear regression methods are mainly used; however, this method is weak in slump prediction, because the change of the slump is not linear. BP neural network has been applied to predict

---

<sup>1</sup>This work was supported by the National Natural Science Foundation of China (61502330) and Science and Technology Innovation Project of Shanxi Province (20171119) and Project of Soft Science Project of Shanxi Province (2016041008-5).

<sup>2</sup>Information Department, College of Finance & Economics, Taiyuan University of Technology, No. 25, Qian-feng South Road, Wan Bolin District, Tai Yuan, 030024, China; E-mail: 122824940@qq.com

<sup>3</sup>College of Information, Shan Xi Finance & Taxation College, Tai Yuan, 030024, China

<sup>4</sup>College of Data Science, Tai Yuan University of Technology, Tai Yuan, 030024, China

<sup>5</sup>Corresponding author; e-mail: liuxinyu1206@163.com

the strength of concrete with more satisfying effect in comparison [1]. However, it needs more training data to enhance the precision in practice [2].

The artificial neural network methods (ANNs) are the most popular among machine learning methods and have been proposed for predicting the strength of concrete. For example, back propagation (BP) neural network is applied in the analysis of concrete structure [3], but this method needs large data for training.

The support vector machine is a fashionable machine learning algorithm presently owing to its advantages, such that it can find the global minimum point and obtain a more precise prediction effect with less training data [4].

This paper attempts to use the return of the machine algorithm in SVM to predict and analyze the slump and strength of HSC.

The parameters' setting of SVM is a key factor in the performance of support vector machine, thus it must be set carefully. It is proposed that a genetic optimization algorithm to compute the parameters for solving this problem automatically in our experiment.

In this paper, an SVM method is utilized to predict the slump and the compressive strength of high-strength concrete, with nonlinear regression constructed by this method [4]. In addition, through the analysis of the results of fitting, the special variation discipline of slump and compressive strength of HSC be found.

## 2. Partial least squares regression

### 2.1. The principle of PLSR

Let us consider  $m$  independent variables  $X_1, \dots, X_m$  and  $n$  dependent variables  $Y_1, \dots, Y_n$ . The principle of PLSR is following:

First, it is obtained the first principal component  $T_1$ , that is a linear combination of variables  $X_1, \dots, X_m$  with extraction of more variation information in the independent variables. Meanwhile, it is also obtained the first principal component  $U_1$ , that is a linear combination of variables  $Y_1, \dots, Y_n$ , with the maximum degree of correlation between  $T_1$  and  $U_1$ .

Then the regression of dependent variables  $Y_1, \dots, Y_n$  and  $T_1$  is constructed. If the precision of regression is satisfactory, the algorithm ends, otherwise it continues to extract the second principal component, repeating the above steps until meeting the required accuracy.

Ultimately, the  $r$  components  $T_1, \dots, T_r$  of independent variables are obtained for constructing the regression of  $Y_1, \dots, Y_n$ , then the dependent variables  $Y_1, \dots, Y_n$  are expressed by the independent variables  $X_1, \dots, X_m$ , that is final partial least squares regression equation [5].

### 2.2. The features of PLSR

The essence of PLSR is the translation and rotation of original coordinate system so that a new coordinate's origin coincides with the center of gravity of the sample points.

PLSR has a very strong ability to set up forecasting model, but useless orthogonal information will decrease the forecasting accuracy. In addition, PLSR is a linear regression method, that it is incapable in the case of nonlinear relationship.

### 3. Principle of BP neural network

#### 3.1. The structure of BP neural network

There is a multi-layer feed-forward network in BP neural network. The network includes an input layer, an output layer and at least one hidden layer. Each layer consists of several neurons. Adjacent neurons connect between the two layers through the weight. And there is no direct relation between neurons in same layer. The structure of a simple BP network is shown in Fig. 1.

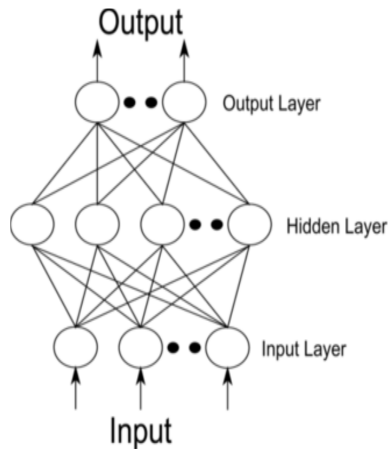


Fig. 1. Structure of a simple BP network

#### 3.2. BP learning algorithm

This machine learning algorithm is a steepest descent method, that it adjusts the weight between neurons by sample training for the smallest output error, called error back-propagation learning [3].

After the trained machine has obtained the stable and optimized weights, it can predict a value by inputting testing data.

#### 3.3. The features of BP network

BP network can achieve non-linear function fitting and forecasting, but training is slow, requires a lot of training data, and often falls into a local minimum.

## 4. Support vector machine regression

### 4.1. The principle of SVM

SVM is mainly based on the following idea [6]:

Firstly, it is converted from the sample space  $x_1, y_1, \dots, x_r, y_r \in \mathbb{R}^n$  to a high-dimensional feature space by non-linear mapping function  $\Phi(\cdot)$ . In the feature space, the optimal decision function is constructed. And the kernel function  $K(x_i, y_j)$  is introduced to replace the dot product in the space for decreasing computation.

The optimal decision function is defined as

$$y(x) = \text{sgn}(w \cdot \Phi(x) + b). \quad (1)$$

By introducing slack variables  $\xi_i$ , one can resolve a problem when some vectors  $x_i$  are divided into the wrong place [9]. The parameter  $C$  is a penalty factor. Thus, the optimal problem can be simplified using the following expression

$$\min J(\omega, \xi) = \frac{1}{2} \|\omega\|^2 + C \sum_{i=1}^M \xi_i, \quad C > 0,$$

$$\text{s.t. } [\Phi(x_i) \cdot w + b] \geq 1 - \xi_i$$

$$\xi_i \geq 0, \quad i = 1, 2, \dots, l. \quad (2)$$

Further, it can be converted from the above expression to the quadratic programming problems by Lagrange method.

$$\max W(\alpha) = -\frac{1}{2} \sum_{i,j=1}^l \alpha_i y_i y_j K(x_i, x_j) \alpha_j + \sum_{i=1}^l \alpha_i,$$

$$\text{s.t. } \sum_{i=1}^l \alpha_i y_i = 0, \quad 0 \leq \alpha_i \leq c, \quad i = 1, 2, \dots, l. \quad (3)$$

Thus, the nonlinear regression function takes the form [9]

$$f(x) = \sum_{i,j=1}^l (\alpha_i - \alpha_j) \cdot K(x_i \cdot x) + b. \quad (4)$$

For the nonlinear mapping, in this work the Gaussian kernel function is selected as

$$K(x_i, x) = \exp\left(-\frac{\|x - x_i\|^2}{2\sigma^2}\right). \quad (5)$$

The parameters of  $C$  and  $\sigma$  play a very key role in the performance [7]. Generally they are set by experience that leads to low performance in computation. In this

experiment, they are set by genetic algorithm automatically.

#### 4.2. The features of SVM

The support vector machine has an excellent performance in non-linear fitting function and prediction with the characteristics of high precision, quick response and less data.

#### 4.3. GA--SVM algorithm

In this paper, genetic algorithm (GA) is used to set penalty factor  $C$  and kernel parameter  $\sigma$  so that SVM reaches an excellent performance.

The main idea of genetic algorithm is a simulation of genetic selection, crossover and mutation in nature, which it is a biologically motivated adaptive system [8]. It is the most effective approach to set the optimal parameters without human intervention. The principal method is as follow:

Step 1. Encoding chromosomes: each of parameters needs to be encoded by binary respectively after initializing parameters.

Step 2. Fitness function is constructed by root mean square error (RMSE) in order to guide the search.

$$\text{RMSE} = \sqrt{\frac{1}{n} \sum_{i=1}^n (y_i - \bar{y}_i)^2}. \quad (6)$$

Step 3. Sample  $x_i$  is selected by the following formula, which computes the possibility  $p_{si}$  of selected sample  $x_i$ , assuming the fitness of sample  $x_i$  as  $f_i$ . That is a plot for keeping species elitist in the next generation.

$$p_{si} = \frac{f_i}{\sum f_i}. \quad (7)$$

Step 4. Crossover and mutation: the genetic segments will be exchanged in the breaking points between two chromosomes in terms of single-point crossover principle. Mutation is a process that one bit of information randomly alters from "1" to "0" or from "0" to "1" in accordance with roulette wheel model [9].

Step 5. Breeding the next generation.

Step 6: When the number of population is constant, the chromosomes are the final results; otherwise go back to Step 2.

## 5. Experiment and analysis

### 5.1. The strength and slump model of HSC

5.1.1. *Experimental method and experimental data.* The goal of this experiment is to predict the strength and slump of HSC in first 28 days.

There are too many factors that can influence the slump and strength of high-strength concrete [1], [3]. Generally considered, major factors including water, cement, fly-ash, silica-fume, sand, gravel, sand ratio, super plasticizer and exposed days are selected as input feature parameters, while output values are slump and strength.

There are six big groups of data, representing the six different grades from C50 to C100. Each big group contains 14 small groups, with each small group including data of every seven days from the first day to the ninety-one day and having 3 samples. The data are from the Department of Material Engineering of TYUT. Nine groups data of C50, C80 and C100 are listed in Table 1, where the samples No. 3 and No. 6 (randomly selected) are used as the test samples, the remaining groups servings as training samples.

MATLAB SVM toolbox is used to train the data and with CityplaceMATLAB StateGA toolbox to search for better combinations of the parameters in SVM [9].

MATLAB neural network toolbox is used to train the BP neural network and determine the optimal number of hidden layer neurons, the training function and learning rate.

MATLAB PLSR function is used to calculate data and predict trends.

*5.1.2. Experimental parameters.* The computing parameters of GA are listed in Table 2 and parameters of SVM are listed in Table 3.

*5.1.3. Analysis and results.* Figure 2 shows the strength fitting for different levels in the 28th day. After computing the compressive strength variation of different concrete grades, the results are shown in Tables 4 and 5.

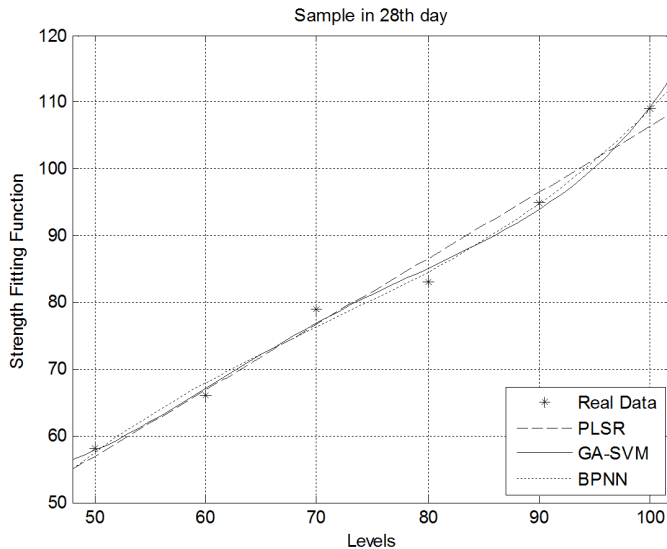


Fig. 2. Strength fitting for different levels in the 28th day

Table 1. Input data

No.	Grade	Water	Cement	Fly ash	Silica fume	Sand	Gravel	Sand ratio	Superplasti-cizer (%)	Day	Compression strength (MPa)	Slump (mm)
1	C50	171	385	165	0	621	1075	0.38	1.32	28	65.4	161
2		175	433	108	0	635	1051	0.39	1.35	28	69.2	157
3		184	410	99	0	650	1025	0.38	1.25	28	62.1	192
4	C80	170	322	162	54	622	1073	0.36	1.44	28	82.5	165
5		177	365	101	43	640	1045	0.36	1.41	28	79.8	139
6		180	410	53	55	641	1039	0.37	1.44	28	86.3	160
7	C100	162	361	109	77	606	1084	0.36	1.62	28	112.2	185
8		168	352	166	70	611	1092	0.36	1.52	28	103.2	180
9		169	412	54	76	621	1069	0.37	1.60	28	105.4	182

It can be found in Fig. 2 that the three curves represent almost linear change in the same direction along with the strength grade. Table 4 shows that the learning time and testing time of GA-SVM is faster, meanwhile with smaller error by comparing with BP neural networks. We can see in Table 5 that the three methods to predict the results are basically identical.

Table 2. The results of the genetic algorithm

Algorithm name	Average number of iterations	Average convergence time (ms)	Global optimal probability (%)
GA	92	101	70.51

Table 3. Selected parameters for SVM

Parameters	Value by GA
$C$	200
$\delta^2$	0.21

Table 4. The effectiveness of three methods

Methods	Learning time (ms)	Testing time (ms)	Mean squared error (MSE)	Maximum error
GA-SVM	221	32	0.006	1.8
BPNN	870	113	0.012	1.7
PLSR	90	0.2	0.037	3.5

Table 5. The compressive strength prediction of three methods

Test sample	Actual Value	GA-SVM	BPNN	PLSR
No. 3	60.1	60.5	61.1	59.7
No. 6	86.3	84.7	85.2	84.3

After computing the slump variation of different concrete grades, the results are shown in Tables 6 and 7.

Table 6. The compressive strength prediction of three methods

Methods	Mean squared error (MSE)	Max error
GA-SVM	0.021	4
BPNN	0.043	9.5
PLSR	2.731	23

Table 7. The slump prediction of three methods

Test sample	Actual Value	GA-SVM	BPNN	PLSR
No. 3	192	194	188	173
No. 6	160	162	174	168

Figure 3 shows that slump does not increase monotonously along with the increase of strength grade, presenting highly nonlinear relationship, and PLSR method failures in this case. However, this change rule can be basically captured by the BP and SVM methods.

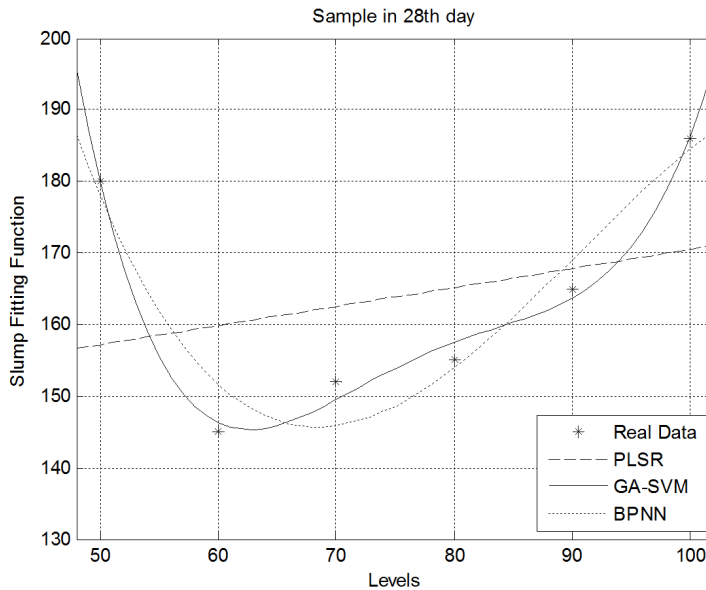


Fig. 3. Slump fitting for different levels in the 28th day

Looking carefully at the curves at the same time, we can also further find that the SVM method can be more accurate fitting sample points by comparing with BPNN. Between strength grades 60 and 70, there is a minimum point of BPNN fitting curve, having a maximum error around this point. According to the analysis of "The clinical phenomenon", it is drawn that BPNN method easily falls into a local minimum [2]. This situation does not exist in SVM method, since SVM method obtains optimization in the global.

## 5.2. Hardening procedure model of HSC

5.2.1. *Experimental method and experimental data.* The purpose of this experiment is to fit the hardening process of high-strength cement. The calculation tools, method and data are same as the previous experiment, moreover, a time factor is added into the analysis model.

5.2.2. *Analysis and results.* After computing the dependence of compressive strength variation on time, the results are shown in Tables 8 and 9.

Table 8. The effectiveness of three methods taking into account the time factor

Methods	Learning time (ms)	Testing time (ms)	Mean squared error (MSE)	Maximum error
GA-SVM	521	82	0.003	0.97
BPNN	1982	97	0.021	2.3
PLSR	133	0.2	0.792	21.2

Table 9. The strength prediction of three methods

Test sample	Actual Value	Days	GA-SVM	BPNN	PLSR
C50	53	29	52.3	52.7	48.3
C80	81	36	80.5	82.7	67
C100	101	90	100.6	101.2	113

By comparing, Table 9 demonstrates that the learning time and testing time of GA-SVM is faster and its error is smaller. It also displays that PLSR method cannot be applied in the whole hardening process of high-strength concrete.

The training and the testing parameters during this process present: the efficiency and error of GA-SVM can meet the needs of HSC. That is to say, GA-SVM is more senior to BPNN in the aspect of high-strength concrete strength prediction.

## 6. Conclusion

In this paper, a new GA-SVM method is applied to predict the slump and strength of high-strength concrete.

In this approach, genetic algorithm is used to set up adaptive parameters for the SVM.

It is obviously found the different effects using three methods respectively with the same experimental data.

By comparisons, the computed precisions of GA-SVM are superior to BP neural network and PLSR.

And it also reveals that the GA-SVM method is very promising for predicting the slump and strength of HSC according to computation effectiveness and precision. By the analysis of these experiment results, it is found that strength variation of HSC is not linear, and the compressive strength in 28th day is not the final value, further still a lot to increase after 28th day. In addition, addition, it is observed that slump with the change of strength grade is monotonous.

It can be found in Figs.4-4 that the sample variation with time is nonlinear, meanwhile both SVM and BPNN can reflect this nonlinear relationship.

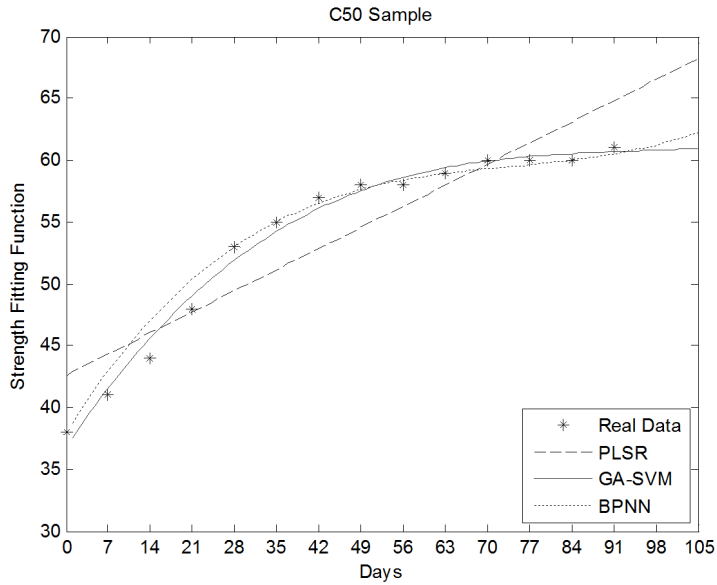


Fig. 4. Strength fitting for C50 sample

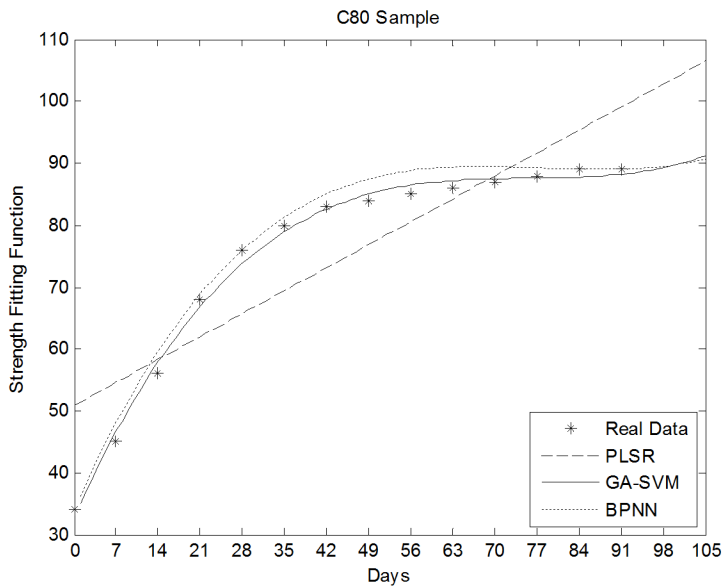


Fig. 5. Strength fitting for C80 sample

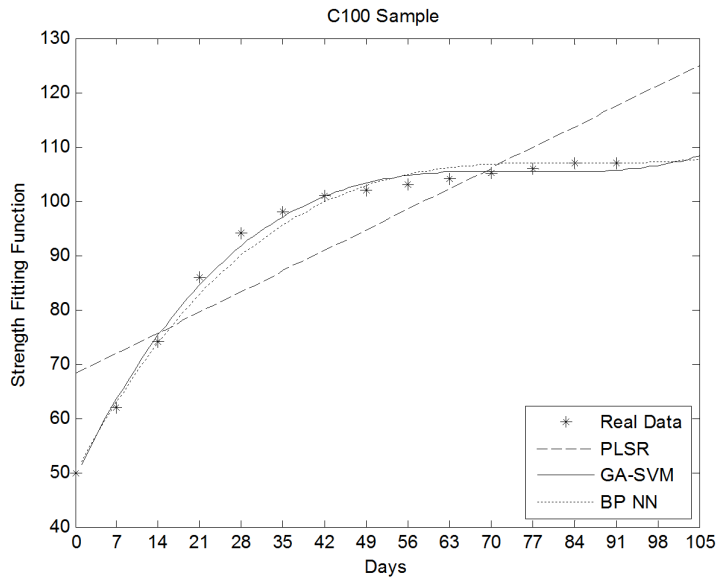


Fig. 6. Strength fitting for C100 sample

We also can draw that:

1. The compressive strength of HSC is still a lot of change after the first 28th day that the change with time is nonlinear.
2. The compressive strength variation of HSC with time is linear before 35th day basically, that the relationship can be reflected by PLSR.
3. The compressive strength value in 42nd day can be practically taken as the hardening index of HS.

## References

- [1] M. HAN, J. H. XI, L. J. WANG, J. C. WANG: *Application of artificial neural networks for analyzing concrete strength*. Journal of Building Materials 4 (2001), No. 2, 192–195.
- [2] X. J. CHEN, GUANG, X. D. PEI: *Artificial neural network technology and its application*. Beijing: China Electric Power Press (2003).
- [3] I. C. YEH: *Simulation of concrete slump using neural networks*. Proceedings of the Institution of Civil Engineers - Construction Materials 162 (2009), No. 1, 11–18.
- [4] J. L. AN, Q. X. YANG, Z. P. MA: *Study on SVM on-line function regression method for mass data*. International Conference on Machine Learning and Cybernetics, 19–22 August 2007, Hong Kong, China, IEEE Conferences 5 (2007), 2773–2777.
- [5] Y. L. ZHAO, LEI MING: *Multivariable PLSR analysis for quality effect factor of high strength concrete*. Cement Engineering (2006), No. 5, 1–6.
- [6] Z. LI, H. HE, S. ZHAO: *Research on support vector machine's prediction of concrete carbonization*. International Seminar on Business and Information Management, 19–19 December 2008, Wuhan, China, IEEE Conferences 1 (2008), 319–322.
- [7] J. ZHOU, T. BAI, J. TIAN, A. ZHANG: *The study of SVM optimized by Culture Particle Swarm Optimization on predicting financial distress*. International Conference on In-

dustrial Engineering and Engineering Management, 8–11 December 2008, Singapore, IEEE Conferences (2008), 1689–1693.

- [8] J. ZHOU, T. BAI, C. SUO: *The SVM optimized by culture genetic algorithm and its application in forecasting share price*. International Conference on Granular Computing, 26–28 August 2008, Hangzhou, China, IEEE Conferences (2008), 838–843.
- [9] Q. LI: *Analysis and assessment of voltage stability based on GA-SVM*. Journal of System Simulation 26 (2014), No. 10, 2369–2373.

Received April 10, 2018



# Cooperative localization approach for multi-robot systems based on state estimation error compensation<sup>1</sup>

ZHANG SHI-JIE<sup>2</sup>, SHI QING-SHENG<sup>2</sup>, CAO YI<sup>2</sup>

**Abstract.** In order to improve the localization accuracy of multi-robot systems, a cooperative localization approach with communication delays is proposed in this paper. In the proposed method, the reason of time delay for robots' cooperative localization approach is analyzed firstly, and then the state equation and measure equation were reconstructed by introducing the communication delays into the states and measurements. Furthermore, the cooperative localization algorithm using extended Kalman filtering technique based on state estimation error compensation is proposed to reduce the state estimation error of delay filtering. Finally, the simulation and experiment results demonstrate that the proposed algorithm can achieve good performance in location in the present of communication delay, meanwhile, with reduced computational and communicative cost.

**Key words.** Cooperative localization, multi-robots system, communication delays, state estimation error compensation.

## 1. Introduction

Multi-robot systems were first proposed in early 1980s. In multi-robot systems, team of robots can increase the reliability and performance over single robot. Additionally, information can be shared across the team to improve the localization accuracy. Multi-robot systems have been widely used in a variety of tasks such as target tracking [1, 2], data collection [3], rescue [4–6] and formation [7, 8].

Precise knowledge about locations and poses of the robots in the multi-robot systems is a basic condition for the collaborative tasks. One approach to localize

---

<sup>1</sup>This work is supported by National Nature Science Foundation under Grant 61403124, and supported by Natural Science Project of Henan provincial Science and Technology Department under Grant 182102210392, and the Fundamental Research Funds for the Henan Provincial Colleges and Universities in Henan University of Technology under Grant 2017QNJH32.

<sup>2</sup>Henan University of Technology, Zhengzhou 450001, China

<sup>3</sup>E-mail addresses: zhangshijie@haut.edu.cn, shiqs@haut.edu.cn, caoyioffice@163.com

the robots is to equip them with Global Positioning System (GPS) receivers and use the GPS system. However, GPS signals are not available indoors and they cannot directly provide the orientation information. An alternative approach is cooperative localization (CL) in which robots work together and use the robot-to-robot measurements to construct a map of their network [9]. Since the pioneering works of Kurazume et al. [10] in 1994, the cooperative localization problem of multi-robot systems has attracted the interest of many researchers in the past few years [11, 12].

In [13], a CL approach based on Extended Kalman Filter (EKF) was presented to update an estimate of the robot poses in correspondence to each sensor measurement. An entropic criterion was used to select optimal measurements that reduce the uncertainty relative to the estimate of the robot poses. In [14], the relative position information was used to improve the localization accuracy in a multi-robot system. The upper bound of the uncertainty was described as a function of time and noise characteristics of the robot sensors. In the above case, the effect of the uncertainty in both the state propagation and the relative position measurements is ignored, resulting in a simplified distributed algorithm. In [15] the sample-based Monte Carlo Localization (MCL) algorithm was proposed to improve collaborative localization of indoor robots team. The MCL algorithm was extended in [16] to the case of two robots if the map of environment is available to both robots. However, the drawback of MCL approach is that it can be only used in known environments.

In practical application, the communication constraints should be taken into account, the information from different types of sensors in the multi-robot systems need to be fused. However, due to the different working frequency and the different information processing time of these different proprioceptive sensors, it causes many problems such as time-delay, which means the delayed measurements are used when state filtering of sensor measurement outputs. Unexpected positioning errors may increase or even filtering divergence if ignoring the influence of communication delay. A delayed extended Kalman filter (DEKF) method was proposed to solve the communication delay problem in CL [17, 18], the delayed information was converted to current measurement after transformations, and then used for update. However, this algorithm may fail due to large amount of calculations.

Consider the reason above, an extended kalman filtering (EKF) based on state estimation error compensation is designed in this paper to deal with the communication delay. In the proposed method, the delayed measurements are predicted in advance to compensate the state estimation error, and the proposed cooperative localization algorithm is applied to leader-follower robot formation to demonstrate the effectiveness of the proposed strategy.

## 2. Problem formulation

In this paper, we consider that each individual robot in the group carries sensors to exchange information within the multi-robot systems. As shown in Fig. 1, assume that at time  $t_1$ , the Robot  $b$  sends communication and pose measurement requests to Robot  $a$ . After the data transmission time  $T_a$ , Robot  $a$  receives the requests

from Robot  $b$  at time  $t_2$ , and it takes time  $T_b$  for processing those information. Then, Robot  $a$  sends the relative distance and pose estimation to Robot  $b$  at time  $t_3$ , and Robot  $b$  receives the relative measurements from Robot  $a$  at time  $t_4$  after data transmission time  $T_c$ . In the entire communication process, the time delay we considered in this paper including data transmission time  $T_a$  and  $T_c$ , and the information processing time  $T_b$ . In practical work, the data transmission time  $T_a$  and  $T_c$  are typically very short, therefore, this paper will pay more attention to the information processing time  $T_b$ . Consider the situation that the information processing time  $T_b$  caused by communication device is usually fixed. Then, the following time-invariant delay is considered in this paper:

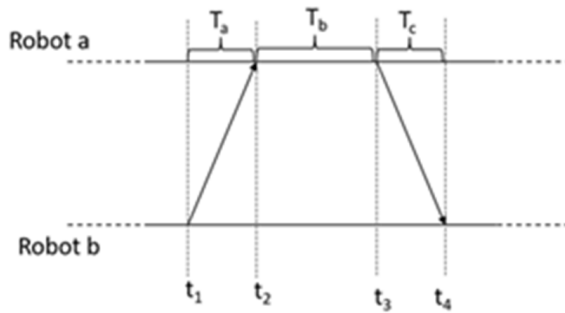


Fig. 1. Time line of robot-to-robot communication

As stated previously, there are  $N$  filtering periods during the entire communication process. Denote  $Z(k)$  the measurements which Robot  $b$  received at time  $t_4$ , the relative range and absolute position information received from Robot  $a$  are used for measurements update of the systems. Due to the existence of delay, these state vector used for measurements update are actually measured at time  $t_2$ . Therefore, the problem this paper deals with is how to improve the location accuracy and reliability of the systems under the time-invariant delay.

**2.1. The augmented state motion model with delay**

Consider the augmented state model with time delay. For the convenience of analysis, the leader-follower structure is used for the multi-robot systems in this paper, and here we use symbol  $t_s$  and  $t_k$  substituting  $t_2$  and  $t_4$  in the following equations.

The states of the systems are denoted as

$$X(k) = (x_l(s), y_l(s), x_f(k), y_f(k), \theta_f(k))^T, \tag{1}$$

where the subscripts  $l$  and  $f$  denote the leader robot and follower robot respectively, and  $x_l(s), y_l(s)$  denote the state of the leader robot at time  $t_s, x_f(k), y_f(k), \theta_f(k)$  denote the state of the follower robot at time  $t_k$ . Then, the linearized propagation

equation for the follower robot is described as

$$\tilde{X}_f(k+1) = \Phi_f(k) \tilde{X}_f(k) + \Gamma_f(k) \omega_f(k), \quad (2)$$

where

$$\Phi_f(k) = I + \delta t \begin{bmatrix} 1 & 0 & -\delta t v_f(k) \sin(\theta_f(k)) \\ 0 & 1 & \delta t v_f(k) \cos(\theta_f(k)) \\ 0 & 0 & 1 \end{bmatrix}$$

$$\Gamma_f(k) = \begin{bmatrix} \delta t \cos(\theta_f(k)) & 0 \\ \delta t \sin(\theta_f(k)) & 0 \\ 0 & \delta t \end{bmatrix}$$

and  $\delta t$  is the period time of sampling,  $v_f(k)$  and  $\theta_f(k)$  are the linear and rotational velocities of the robot at time  $t_k$ . Quantity  $\omega_f(k)$  is the system noise due to the errors in the linear and rotational velocity measurements of the follower robot. The system inputs are denoted as

$$u(k) = (x_1(s), y_l(s), v_f(k), \theta_f(k)). \quad (3)$$

Then, the linearized augmented state equation is described as

$$\tilde{X}(k+1) = \Phi(k) \tilde{X}(k) + \Gamma(k) \omega(k), \quad (4)$$

where

$$\begin{cases} \tilde{X}(k+1) = \begin{bmatrix} \tilde{X}_1(s+1)^T & \tilde{X}_f(k+1)^T \end{bmatrix}^T, \\ \omega(k) = \begin{bmatrix} \omega_1(s)^T & \omega_f(k)^T \end{bmatrix}^T, \\ \Phi(k) = \text{diag} \left( \begin{matrix} \Phi_1(s) & \Phi_f(k) \end{matrix} \right), \\ \Gamma(k) = \text{diag} \left( \begin{matrix} \Gamma_1(s) & \Gamma_f(k) \end{matrix} \right). \end{cases}$$

and the system noise covariance is given as

$$Q(k) = E[\omega(k) \omega^T(k)] = \begin{bmatrix} \sigma_v^2(k) & 0 \\ 0 & \sigma_\theta^2(k) \end{bmatrix}, \quad (5)$$

and  $\Phi(k)$  and  $\Gamma(k)$  are the Jacobian matrices of the state vector and error vector, respectively.

## 2.2. Measurement model with delay

Supposing that the follower robot receiving the ranging information from the leader robot. The range measurement model with communication delay can be described shortly as

$$Z(k) = C(k) X(k) + v(k). \quad (6)$$

According to the states defined in (1), the states of the leader robot at time  $t_s$  and the states of the follower robot at time  $t_k$  are included in the states of system. However, the measurement of system only consist of self-location of the leader robot

and the relative position information at time  $t_s$ . Consider that the measurement at  $t_k$  equals to the measurement at  $t_s$  after  $N$  filtering periods. Then the measurement model can be reconstructed as

$$Z(k) = C(k)X(k) + v(k) = c_l(s)X_l(s) + c_f(s)X_f(s) + v(k) \tag{7}$$

Utilizing the system state transition matrix, we have

$$X_f(s+1) = \vartheta(s+1, k+1)X_f(k+1) = \vartheta(k+1, s+1)^{-1}X_f(k+1) \tag{8}$$

where the relationship of the one-step prediction state of the follower robot at time  $t_k$  and the system state at time  $t_s$  is described in (8). Substituting (8) in (7) yields

$$\begin{aligned} Z(k) &= c_l(s)X_l(s) + c_f(s)X_f(s) + v(k) \\ &= c_l(s)X_l(s) + \vartheta_f(k, s)^{-1}X_f(s) + v(k) \\ &= \begin{bmatrix} c_l(s) & c_f(s)\vartheta_f(k, s)^{-1} \end{bmatrix} \begin{bmatrix} X_l(s) \\ X_f(s) \end{bmatrix} + v(k), \end{aligned} \tag{9}$$

where the system state transition matrix is given as:

$$\vartheta(k, s) = \prod_{i=s}^k \vartheta(i), \tag{10}$$

$$\vartheta_f(k, s)^{-1} = \prod_{i=s}^k \vartheta_f(i)^{-1} = \begin{bmatrix} 1 & -\sum_{i=s}^k L(i) \\ 0 & 1 \end{bmatrix},$$

$$L(i) = \begin{bmatrix} -\delta t^2 V_f(i) \sin(\theta_f(i)) \\ -\delta t^2 V_f(i) \cos(\theta_f(i)) \end{bmatrix}$$

$$c_l(s) = \frac{\partial Z(s)}{\partial X_l(s, s-1)^T}, \quad c_f(s) = \frac{\partial Z(s)}{\partial X_f(s, s-1)^T},$$

and the measurement noise covariance matrix s given by

$$R(k) = E[v(k) v^T(k)].$$

### 3. Cooperative localization with communication delays

The system and measurement model with communication delay has been expressed in the previous section. Based on the measurement update, this paper propose a Delayed Extended Kalman Filter (DEKF) to deal with the problem of cooperative localization with communication delays.

First, the one-step prediction state of the multi-robots system is given as follows:

$$\widehat{X}(k+1, k) = \begin{bmatrix} \widehat{X}_l(s+1, s)^T & \widehat{X}_f(k+1, k)^T \end{bmatrix}^T \tag{11}$$

where  $\widehat{X}_1(s+1, s)^T$  and  $\widehat{X}_f(k+1, k)^T$  denote the one-step prediction states of the leader robot at time  $t_s$  and the leader robot at time  $t_k$  respectively.

Based on the linearized augmented state models (4), the one-step state prediction is given as follows:

$$\widehat{X}(k+1, k) = \Phi(k) \widehat{X}(k) \quad (12)$$

and its covariance are also given as follows:

$$P(k+1, k) = \Phi(k) P(k) \Phi^T(k) + \Gamma(k) Q(k) \Gamma^T(k). \quad (13)$$

The estimated state of the system is

$$\widehat{X}(k) = \widehat{X}(k, k-1) + K(k) \left( Z(k) - C(k-1) \widehat{X}(k, k-1) \right),$$

where  $K(k)$  is the filter gain with communication delays.

If the possibility of communication delays were not a consideration, the general KF algorithm can be used to deduce the error prediction as follows:

$$\begin{aligned} \widehat{X}'(k, k-1) &= \Phi(k-1) \widehat{X}(k-1) = \\ &= \Phi(k-1) \begin{bmatrix} (I - K'(k-1)C(k-1)) \widehat{X}(k-1, k-2) \\ +K'(k-1)Z(k-1) \end{bmatrix} = \\ &= \Phi(k-1) \begin{bmatrix} (I - K'(k-1)C(k-1)) \Phi(k-2) \widehat{X}(k-2) \\ +K'(k-1)Z(k-1) \end{bmatrix} = \\ &= \left[ \prod_{i=1}^{N-1} \Phi(k-i) (I - K'(k-i)C(k-i)) \right] \Phi(s) \cdot \\ &\quad \cdot \left[ \prod_{i=1}^{N-1} \widehat{X}'(s, s-1) + K'(s) \widehat{X}'(s, s-1) \right] + \\ &+ \sum_{j=3}^N \left[ \prod_{i=1}^{j-2} \Phi(k-i) (I - K'(k-i)C(k-i)) \right. \\ &\quad \left. \cdot \Phi(k-j+1) K'(k-j+1) Z(k-j+1) \right] + \\ &\quad + \Phi(k-1) K'(k-1) Z(k-1). \end{aligned}$$

The above formula described the correspondence between one-step predictive state at time  $t_k$  and the estimation states among  $N$  Kalman filters.

When communication delays are considered, that is the measurement is unknown

at time  $t_s$ . Then the above formula can be rewritten as

$$\begin{aligned} \widehat{X}'(k, k-1) &= \left[ \prod_{i=1}^{N-1} \Phi(k-i)(I - K(k-i)C(k-i)) \right] \Phi(s) \widehat{X}(s, s-1) \\ &+ \sum_{j=3}^N \left[ \prod_{i=1}^{j-2} \Phi(k-i)(I - K(k-i)C(k-i)) \right. \\ &\quad \left. \cdot \Phi(k-j+1)K(k-j+1)Z(k-j+1) \right] \\ &+ \Phi(k-1)K(k-1)Z(k-1). \end{aligned} \tag{14}$$

Then the error compensation of one-step predictive state at time  $t_k$  can be obtained as follows:

$$\Delta \widehat{X}(k, k-1) = \widehat{X}'(k, k-1) - \widehat{X}(k, k-1). \tag{15}$$

Note that  $K$  in (14) is difference from  $K'$ , which is the filter gain without communication delays. The filter gain  $K$  depends on measurement matrix  $C(s)$  and the system measurement noise covariance matrix  $R(s)$ . At time  $t_s$ , the measurement matrix and the measurement noise covariance matrix can be calculated as  $C'(s)$  and  $R'(s)$ , then (15) can be rewritten as

$$\Delta \widehat{X}(k, k-1) = \left[ \prod_{i=1}^{N-1} \Phi(k-i)(I - K(k-i)C(k-i)) \right] \Phi(s)M(s), \tag{16}$$

where

$$M(s) = K(s) \left( Z(s) - C(s) \widehat{X}(s, s-1) \right). \tag{17}$$

So the error compensation formula of one-step predictive state at time  $t_k$  can be written as

$$X(k, k-1) = X'(k, k-1) + \Delta \widehat{X}(k, k-1). \tag{18}$$

Finally, the cooperative localization algorithm for multi-robot systems can be summarized as follows:

**3.1. Algorithm 1**

1. Initialize: Assume that each robot in the system initially knows its pose with respect to a given reference coordinate frame. As Fig.1 shows, consider at time  $t_k$ , the follower robot receive the pose information from the leader robot with time delay after  $N$  Kalman filters at time  $t_s$ .
2. State prediction and compensation: Give the one-step state prediction and covariance matrix:

$$\begin{aligned} \widehat{X}(k+1, k) &= \Phi(k) \widehat{X}(k) \\ P(k+1, k) &= \Phi(k)P(k)\Phi^T(k) + \Gamma(k)Q(k)\Gamma^T(k). \end{aligned}$$

Calculate the state estimation error compensation:

$$M(k) = \Phi(k)(I - K(k)C(k))M(k-1),$$

$$\Delta \widehat{X}(k+1, k) = M(k) \Phi(s) K(s) \left( Z(s) - C(s) \widehat{X}(s-1, s) \right).$$

Compute the filter gain:

$$K(k+1) = P(k+1, k) C^T(k) [C(k) P(k+1, k) C^T(k) + R(k)]^{-1}.$$

Construct the error-state propagation equation and the covariance propagation equation:

$$\begin{aligned} \widehat{X}(k+1, k) &= X'(k+1, k) + \Delta \widehat{X}(k+1, k), \\ \widehat{X}(k+1) &= \widehat{X}(k+1, k) + K(k+1) \left( Z(k+1) - C(k) \widehat{X}(k+1, k) \right) \\ P(k+1) &= (I - K(k+1) C(k+1)) P(k+1, k). \end{aligned}$$

With the cooperative localization algorithm proposed above, the extended Kalman filtering based on state estimation error compensation with communication delays is designed to improve the location accuracy.

## 4. Simulation results

### 4.1. Setup

In this section, the performance of the proposed algorithm was evaluated by a group of 2 robots with leader-follower structure as shown in Fig. 2. The group of robots moves in a rectangular area in indoor environment. Both robots carry an orientable range finder and wheel encoders for odometry. The range finder is used to compute the measurements aimed at the leader robot. Both the range measurements and the odometric measurements are supposed to be affected by a zero-mean white Gauss noises.



Fig. 2. Experimental setup used for testing the proposed algorithm

### 4.2. Results

In the simulations, it is assumed that the mean velocity of the robots is 1 m/s and the system noise and measurement noise covariance matrices are used as follow:

$$Q = \begin{bmatrix} (0.1 \text{ m/s})^2 & 0 \\ 0 & (3^0)^2 \end{bmatrix},$$

$$R = \begin{bmatrix} (0.5 \text{ m/s})^2 & 0 \\ 0 & (0.5^0)^2 \end{bmatrix}.$$

The communication delays are supposed to be time invariant, as 0.1 s. As shown in Fig. 3, the true trajectory for the leader follower robots team is compared to the trajectory estimated using the proposed cooperative localization algorithm.

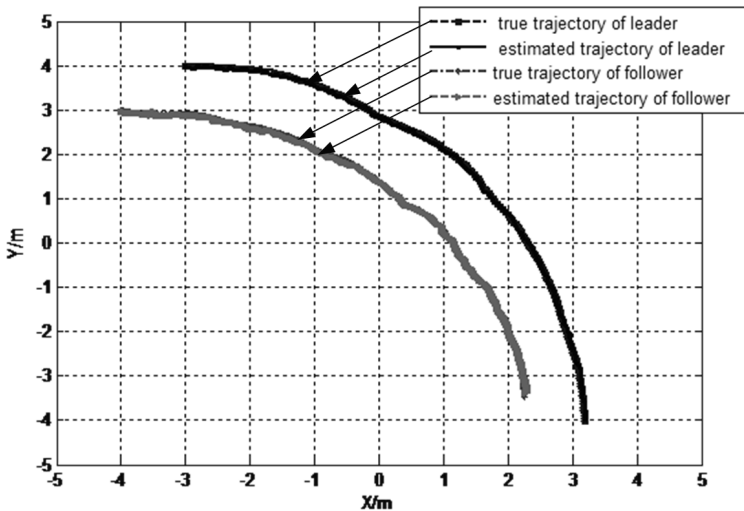


Fig. 3. True trajectory and estimated trajectory for the leader-follower robots team

Figure 4 shows the local enlarged drawing of true trajectory and estimated trajectory. From the above simulation results, the effectiveness of the proposed method were been verified.

Figures 5–7 illustrate the comparative error curves of the follower robot by using the traditional EKF method in the first 100 steps and the proposed method in the next 200 steps, respectively. It can be seen that the estimation errors of the proposed algorithm are bounded in smaller range when compared with the traditional EKF method.

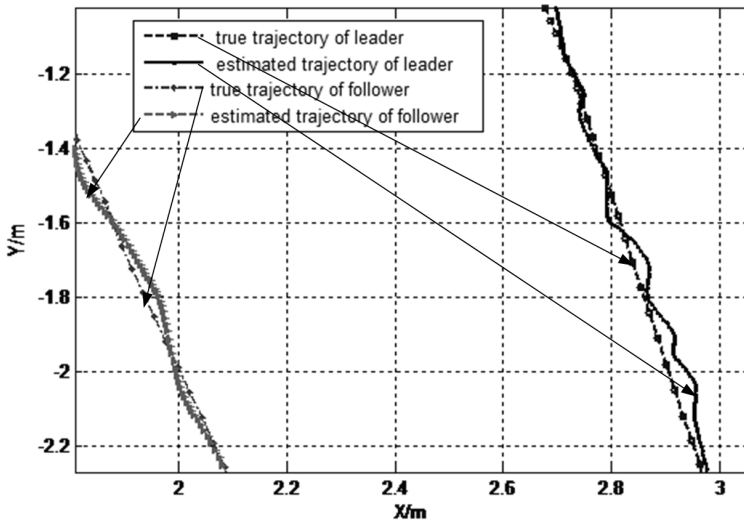


Fig. 4. Local enlarged true trajectory and estimated trajectory for the leader-follower robots team

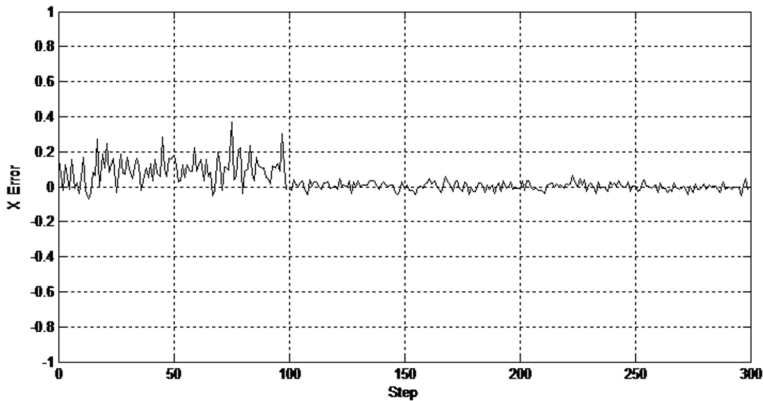


Fig. 5. X-position estimates (the first 100 steps using the EKF method without considering the communication delays, the next 200 steps using the proposed method)

## 5. Conclusion

In this paper, the delayed cooperative localization problem for leader-follower robot system was considered. An extended Kalman filter approach based on state estimation error compensation was proposed to keep positioning accuracy with communication delays. The simulation and experiment results demonstrate that the estimation accuracy of the proposed method is comparable with the traditional EKF localization method.

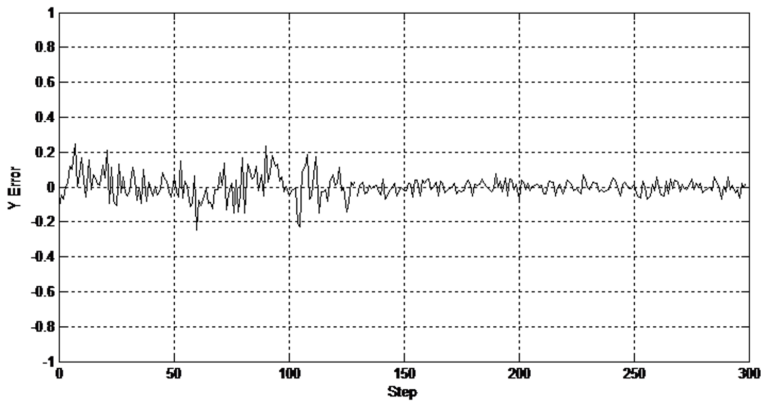


Fig. 6. Y-position estimates (the first 100 steps using the EKF method without considering the communication delays, the next 200 steps using the proposed method)

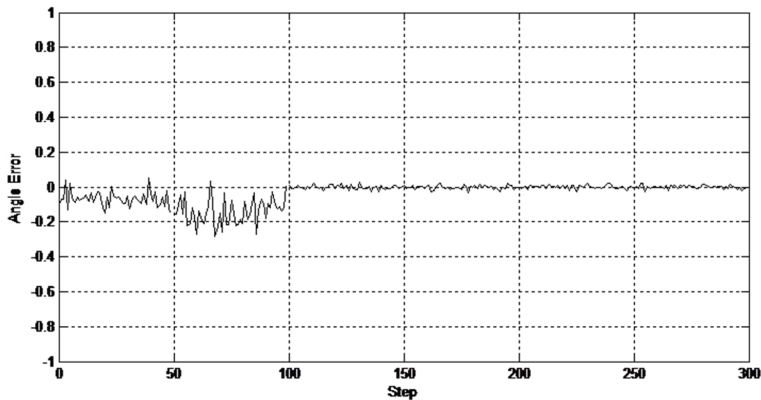


Fig. 7. Orientation estimates (the first 100 steps using the EKF method without considering the communication delays, the next 200 steps using the proposed method)

## References

- [1] A. W. STROUPE, M. C. MARTIN, T. BALCH: *Distributed sensor fusion for object position estimation by multi-robot systems*. IEEE International Conference on Robotics and Automation (Cat. No.01CH37164), 21–26 May 2001, Seoul, South Korea, Proceedings IEEE 2 (2001), 1092–1098.
- [2] C. SOTO, B. SONG, A. K ROY-CHOWDHURY: *Distributed multi-target tracking in a self-configuring camera network*. IEEE Conference on Computer Vision and Pattern Recognition, 20–25 June 2009, Miami, FL, USA, Proceedings IEEE (2015), 1486–1493.
- [3] J. OYEKAN, H. HU: *Ant robotic swarm for visualizing invisible hazardous substances*. Robotics 2 (2013), No. 1, 1–18.
- [4] L. E. PARKER: *Distributed algorithms for multi-robot observation of multiple moving targets*. Autonomous Robots 12 (2002), No. 3, 231–255.
- [5] F. M. DELLE FAVE, S. CANU, L. IOCCHI, .NARDI, V. A. ZIPARO: *Multi-objective*

- multi-robot surveillance*. IEEE International Conference on Autonomous Robots and Agents, 10–12 Februar 2009, Wellington, New Zealand, Proceedings IEEE (2009), 69–73.
- [6] M. KARAKAYA, H. QI: *Collaborative localization in visual sensor networks*. ACM Transactions on Sensor Networks (TOSN) 10 (2014), No. 2, 1-24.
- [7] W. DONG: *Tracking control of multiple-wheeled mobile robots with limited information of a desired trajectory*. IEEE Transactions on Robotics 28 (2012), No. 1, 262–268.
- [8] W. DONG, C. CHEN, Y. XING: *Distributed estimation-based tracking control of multiple uncertain non-linear systems*. International Journal of Systems Science 45 (2014), No. 10, 2088–2099.
- [9] X. WANG, Y. SEKERCIOGLU, T. DRUMMOND: *Vision-based cooperative pose estimation for localization in multi-robot systems equipped with RGB-D cameras*. Robotics 4 (2015), No. 1, 1–22.
- [10] R. KURAZUME, S. NAGATA, S. HIROSE: *Cooperative positioning with multiple robots*. IEEE International Conference on Robotics and Automation, 8–13 May 1994, San Diego, CA, USA, Proceedings IEEE 2 (1994), 1250–1257.
- [11] A. MARTINELLI: *Improving the precision on multi robot localization by using a series of filters hierarchically distributed*. International Conference on Intelligent Robots and Systems, 29 October–2 November 2007, San Diego, CA, USA, Proceedings IEEE/RSJ (2007), 1053–1058.
- [12] N. TRAWNY, T. BARFOOT: *Optimized motion strategies for cooperative localization of mobile robots*. International Conference on Robotics and Automation, 26 April–1 May 2004, New Orleans, LA, USA, Proceedings IEEE/ICRA 1 (2004), 1027–1032.
- [13] V. CAGLIOTI, A. CITTERIO, A. FOSSATI: *Cooperative, distributed localization in multi-robot systems: A minimum-entropy approach*. IEEE Workshop on Distributed Intelligent Systems: Collective Intelligence and Its Applications, 15–16 June 2006, Prague, Czech Republic, Proceedings IEEE (DIS'06), 25–30.
- [14] S. ROUMELIOTIS, I. REKLEITIS): *Propagation of uncertainty in cooperative multi-robot localization: Analysis and experimental results*. Autonomous Robots 17 (2004), No. 1, 41–45.
- [15] D. FOX, W. BURGARD, H. KRUPPA, S. THRUN: *A probabilistic approach to collaborative multi-robot localization*. Autonomous Robots 8 (2000), No. 3, 325–344.
- [16] S. THRUN, D. FOX, W. BURGARD: *Monte Carlo localization with mixture proposal distribution*. Proceedings of the Seventeenth National Conference on Artificial Intelligence and Twelfth Conference on Innovative Applications of Artificial Intelligence, 30 July–3 August 2000, Austin, TX, USA, Proceedings AAAI (2000), 859–865.
- [17] Y. YAO, D. XU, W. YAN, B. GAO: *Optimal decision making for cooperative localization of MAUVs*. International Conference on Mechatronics and Automation, 9–12 August 2009, Changchun, China, Proceedings IEEE (2009), 1134–1139.
- [18] Y. YAO, D. XU, W. YAN: *Cooperative localization with communication delays for MAUVs*. International Conference on Intelligent Computing and Intelligent Systems, 20–22 November 2009, Shanghai, China, Proceedings IEEE 8 (2009), 244–249.

Received October 12, 2017

# Raising reliability and reducing power loss of power distribution network by determining optimal location and size of capacitor banks

HOSSEIN SABZALI-JAMAAT<sup>1</sup>, YOUSEF  
ALINEJAD-BEROMI<sup>2</sup>, MOHAMMAD HAJIVAND<sup>3</sup>

**Abstract.** In this context, switching capacitor has been placed to improve reliability and reduce power loss in radial distribution system. The objective function has been formulated based on minimizing power loss and improving three reliability indices, which are: Cost of Energy Not-Supplied (CENS), System Average Interruption Frequency Index (SAIFI) and System Average Interruption Duration Index (SAIDI). This problem has been optimized by Group Search Optimization (GSO) algorithm. The GSO algorithm is one of the newest and most powerful swarm intelligence techniques. Simulation has been performed on IEEE standard test system by introducing several scenarios based on the number of capacitor banks.

**Key words.** Capacitor placement, reliability improvement, power loss reduction, group search optimization algorithm, distribution system.

## 1. Introduction

Capacitors are widely installed in distribution systems for reactive power compensation is done to indirectly reduce the real power loss, voltage regulation and system capacity release. And, the installation of shunt capacitors in primary distribution systems can also effectively reduce peak power and energy losses [1].

The published works have been categorized in four groups; which are: evolutionary algorithm, analytical-mathematical techniques, heuristic method and hybrid

---

<sup>1</sup>Department of Electrical and Computer Engineering, Semnan University, Semnan, Iran; e-mail: [h.jamaat@semnan.ac.ir](mailto:h.jamaat@semnan.ac.ir)

<sup>2</sup>Department of Electrical and Computer Engineering, Semnan University, Semnan, Iran; e-mail: [Yalinejad@semnan.ac.ir](mailto:Yalinejad@semnan.ac.ir)

<sup>3</sup>Islamic Azad University, Young Researchers and Elite Club, Boroujerd Branch, Boroujerd, Iran; e-mail: [Mohammadhajivand@ari.ac.ir](mailto:Mohammadhajivand@ari.ac.ir)

approach. In [2–5], evolutionary algorithms have been used to solve the problem. In [2], a new technique for finding the optimal values of the fixed and switched capacitors in the distribution networks with above properties based on the real coded genetic algorithm (RCGA) is presented. An efficient method for simultaneous allocation of fixed and switchable capacitors in radial distribution systems is presented with uncertainty and time varying loads in [3]. Ref. [4] presents an efficient methodology for the optimal location and sizing of fixed and switched shunt capacitors in radial distribution systems using GA. In [5], along with Differential Evolution (DE) Algorithm, Dimension Reducing Distribution Load Flow (DRDLF) is used to find optimal location and size of switching capacitor.

The analytical-mathematical techniques are second approach which authors in [6–10] these method have used. Ref. [6] describes two new approaches for the determination of the direction of switched capacitor banks as well as an efficient technique for estimating the distance of switched capacitors from the monitoring location in distribution systems. Ref. [7] describes two fundamental signatures of shunt capacitor bank switching transient phenomena from which one can accurately determine the relative location of an energized capacitor bank whether it is upstream or downstream from the monitoring location. Ref. [8] deals with the analysis of transients initiated by the switching of shunt capacitors in power networks. These transients will propagate through the network along the transmission elements and will, accordingly, be felt at other locations far from the capacitors, such as load terminals. Ref. [9] proposes a computationally efficient methodology for the optimal location and sizing of static and switched shunt capacitors in radial distribution systems. Similar work has been performed in [10].

Authors of [11–13] suggested heuristic methods to solve the problem. Heuristic search strategies are used to determine the optimum capacitor placement and ratings for distribution systems. In the heuristic approach proposed in [11]. Ref. [12] presents a practical solution technique to the capacitor placement problem that is easy to implement. The proposed approach uses a graph search algorithm. An efficient heuristic algorithm is presented in [13] in order to solve the optimal capacitor placement problem in radial distribution systems.

Finally, in [14–15], hybrid techniques have been employed to solve switching capacitor placement. Ref. [14] presents a fuzzy-reasoning method to optimum shunt capacitor placement and sizing for the radial distribution systems. Ref. [15] considers the problem of optimally placing fixed and switched type capacitors in a radial distribution network.

In this paper, optimal switching capacitor placement has been performed to improve reliability and reduce power loss by GSO algorithm. This paper consists of five sections. The objective function has been formulated in second section. Structure and concept of GSO algorithm has been presented in third section. Simulation results are visible in Section 4. This work has been concluded in Section 5.

## 2. Problem formulation

The proposed objective function OF consists of tree reliability indices have been considered in the objective function. Indices of System Average Interruption Duration Index (SAIFI) and System Average Interruption Frequency Index (SAIFI) are improvement indices from the viewpoint of costumers and Cost of Energy Not Supplied (CENS) is from the viewpoint of Distribution Company. Thus OF is formulated as

$$OF = \sum_{k=1}^{ny} \left\{ \frac{SAIFI_k}{SAIFI_0} + \frac{SAIDI_k}{SAIDI_0} + \frac{CENS_k}{CENS_0} + \frac{Loss_k}{Loss_0} \right\} \quad (1)$$

where  $ny$  is system lifetime,  $Loss_0$ ,  $SAIFI_0$ ,  $SAIDI_0$ , and  $CENS_0$  are the values of indices before placement. By this technique, values of four indices are normalized. To calculate reliability indices, SAIDI, SAIFI and CENS, analytical method based on error modes and their effects (FMEA) is used [16].

## 3. Group search optimization (GSO) algorithm

The population of the GSO algorithm [17–18] is called a group and each individual in the population is called a member. In an  $n$ -dimensional search space, the  $i$ th member at the  $k$ th searching bout (iteration) has a current position  $X_i^k \in R^n$ , a head angle  $\Phi_i^k = \Phi_{i1}^k, \dots, \Phi_{i(n-1)}^k \in R^{n-1}$ . The search direction of the  $i$ th member, which is a unit vector  $D_i^k(\Phi_i^k) = (d_{i1}^k, \dots, d_{i(n-1)}^k) \in R^n$  that can be calculated from  $\Phi_i^k$  via a transformation from polar to Cartesian coordinate system:

$$d_{i1}^k = \prod_{q=1} \cos(\Phi_{iq}^k), \quad (2)$$

$$d_{ij}^k = \sin(\Phi_{i(j-1)}^k) \cdot \prod_{q=1} \cos(\Phi_{iq}^k), \quad (j = 2, \dots, n - 1), \quad (3)$$

$$d_{i1}^k = \sin(\Phi_{i(j-1)}^k). \quad (4)$$

In GSO, a group consists of three types of members: producers and scroungers whose behaviors are based on the PS model; and dispersed members who perform random walk motions. For convenience of computation, we simplify the PS model by assuming that there is only one producer at each searching bout and the remaining members are scroungers and dispersed members. The simplest joining policy, which assumes all scroungers will join the resource found by the producer, is used. In optimization problems, unknown optima can be regarded as open patches randomly distributed in a search space. Group members therefore search for the patches by moving over the search space. It is also assumed that the producer and the scroungers do not differ in their relevant phenotypic characteristics. Therefore, they can switch between the two roles.

### 3.1. Producer

At the  $k$ -th iteration, let the producer's position be denoted as  $\mathbf{X}_p^k = (x_{p1}^k, \dots, x_{pn}^k)$ . It scans three points around it to find a better position. First, the producer scans a point in front of it:

$$X_F = X_P^k + r_1 l_{\max} D_p^k (\Phi^k) . \quad (5)$$

Second, it scans a point on its right-hand side:

$$X_F = X_P^k + r_1 l_{\max} D_p^k (\Phi^k + r_2 \theta_{\max}/2) . \quad (6)$$

Third, it scans a point on its left-hand side:

$$X_F = X_P^k + r_1 l_{\max} D_p^k (\Phi^k - r_2 \theta_{\max}/2) . \quad (7)$$

In (5)–(7),  $r_1$  is a random number normally distributed with mean 0 and standard deviation 1 and  $r_2$  is a random number uniformly distributed in  $[0, 1]$ . Symbol  $y_{\max}$  is the max-pursuit angle, and  $l_{\max}$  is the max-pursuit distance given by the formula

$$l_{\max} = \|U - L\| = \sqrt{\sum_{j=1}^n (U_j - L_j)^2} , \quad (8)$$

where,  $U_j$  and  $L_j$  are the upper bound and lower bound of the search range, respectively.

If the producer finds that the best position at the three points is better than its current position, it moves to the best position and change its head angle using (9), where  $\alpha_{\max}$  is the max-turning angle. Otherwise, it stays at original position. If the producer fails to find a better point in a iterations, it scans front again using eq. (10):

$$\Phi^{k+1} = \Phi^k + r_2 \alpha_{\max} , \quad (9)$$

$$\phi^{k+a} = \phi^k . \quad (10)$$

### 3.2. Scrounger

In the computation, most of the members are chosen as scroungers. If the  $i$ -th member is chosen as a scrounger at the  $k$ -th iteration, it moves toward the producer with a random distance

$$X_i^{k+1} = X_i^k + r_3 \cdot (X_p^k - X_i^k) , \quad (11)$$

where  $r_3$  is a random sequence uniformly distribution in  $[0, 1]$ .

### 3.3. Ranger

The rest members in the group are rangers. If the  $i$ -th is chosen as a ranger at the  $k$ -th iteration, it turns its head to a random angle as (9), and calculates the search direction using Eqs. (2–3), then moves to that direction with a random distance as follows:

$$l_i = ar_1 l_{\max} . \tag{12}$$

## 4. Solving the problem by the GSO algorithm

In Sections 2–3, concepts of optimal capacitor placement problem and GSO algorithm have been presented. In this section, the problem solution by GSO algorithm is discussed. The optimal capacitor placement problem solution by GSO algorithm, whose flowchart is depicted in Fig. 1, has been performed in nine steps:

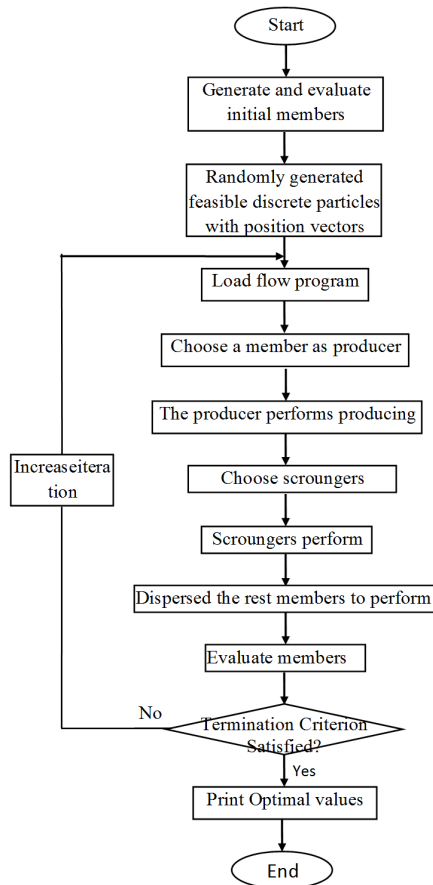


Fig. 1. Flowchart of the solving problem by the GSO algorithm

- Step 1. Generating initial members
- Step 2. Randomly generated feasible discrete particles with position vectors
- Step 3. Running load flow program
- Step 4. Choosing a member as producer
- Step 5. Performing the producer
- Step 6. Choosing scroungers
- Step 7. Performing the scroungers scrounging
- Step 8. Dispersing the rest members to perform ranging
- Step 9. Evaluating members

## 5. Simulation results

In this section, simulation has been performed on IEEE standard test system. For this, a capacitor bank based on 14 steps has been considered (see Table 1). We also divide the sample power system into ten load levels. The value and duration of each load level are shown in Table 2. In this process, the number of capacitive banks is selected according to the economic justification.

Table 1. Capacity and cost of each capacitor bank

Step	Capacity	Cost
1	25	57.73
2	50	81.64
3	100	115.47
4	125	129.10
5	150	141.42
6	200	163.30
7	250	182.57
8	300	200.00
9	400	230.94
10	500	258.19
11	650	294.39
12	800	326.59
13	1000	365.14
14	1200	400.00

### 5.1. Optimal values

Table 3 shows optimal values of capacitor placement in 34 bus IEEE distribution system. By considering results of Table 3, improving reliability from one to four capacitors is considerable while by installing fifth capacitor, the system parameters can be worse destruction. This trend continues in the presence of six capacitor banks. This indicates that the system is saturated in the presence of five banks and the reactive power capacitor capacitance is much more. In the presence of at least one capacitor bank, the aim of the network is reduced by more than half.

Table 2. Load level and its duration

Step	Capacity	Cost
1	0.1391	0.0486
2	0.1101	0.1692
3	0.0609	0.2584
4	0.1304	0.1979
5	0.1130	0.6057
6	0.1014	0.8237
7	0.0841	0.8106
8	0.0812	0.8022
9	0.1014	0.7081
10	0.0783	0.8594

Table 3. Optimal values of capacitor placement

No.	Power Loss	CENS	SAIDI	SAIFI	OF
0	221.4904	241784918	16.7245	23.9344	4.0000
1	68.8941	1173629	8.1684	11.6678	1.9488
2	62.4402	11406418	7.9234	11.3299	1.8922
3	59.1447	1140627	7.9059	11.3021	1.8888
4	63.6595	126575	7.8557	11.2410	1.8749
5	69.5618	1317411	8.7583	12.4030	2.1049
6	62.6449	1304123	9.4429	13.4716	2.2297

**5.2. Optimal location and size of the installed banks**

Fig. 2 shows optimal location and size of the placed capacitor banks on standard system. In each bank, first number is the number of capacitor bank and second is the size of capacitor bank.

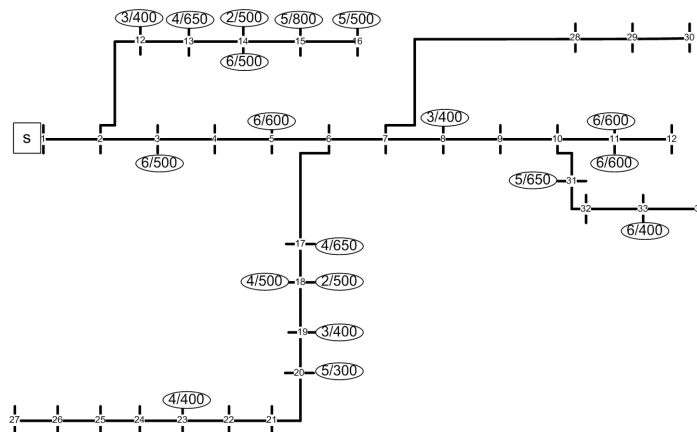


Fig. 2. Single line diagram of test system

Due to the Fig. 2, it can be claimed that buses 14 and 18 are the most likely location to install capacitor. In bus 11, in the presence of six capacitor banks, two banks have been installed, which is a weakness for six capacitors placement. Most capacitor bank capacity is 650 kVAr.

**5.3. Steps change of the placed capacitor banks**

The variation of the number of capacitive banks has been shown in Figs. 3–8. We start with one capacitor bank and increase their number, from which we can observe the maximum change by placing six capacitors.

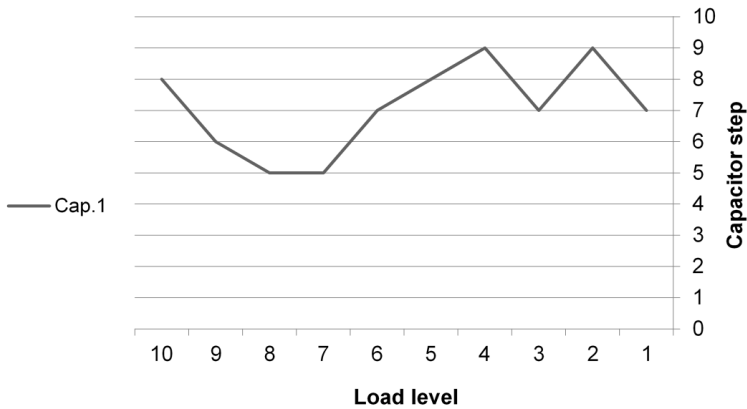


Fig. 3. Placement of one capacitor

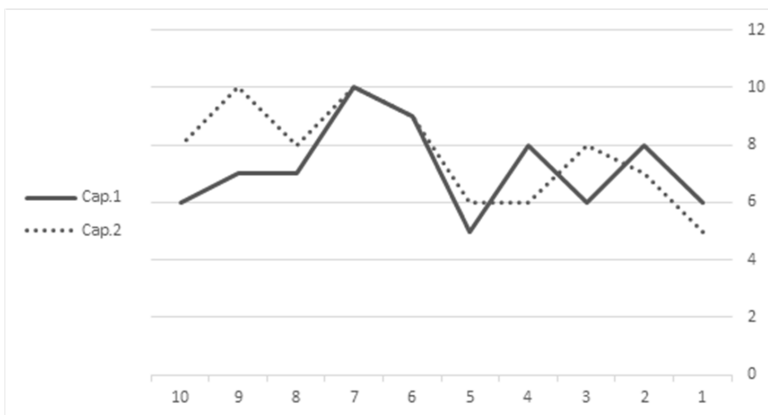


Fig. 4. Placement of two capacitors

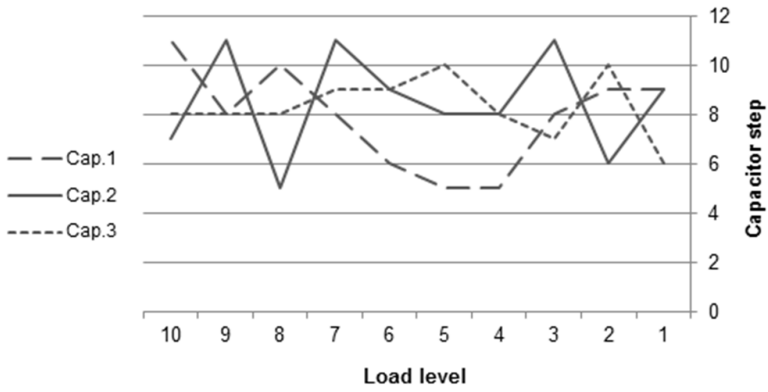


Fig. 5. Placement of three capacitors

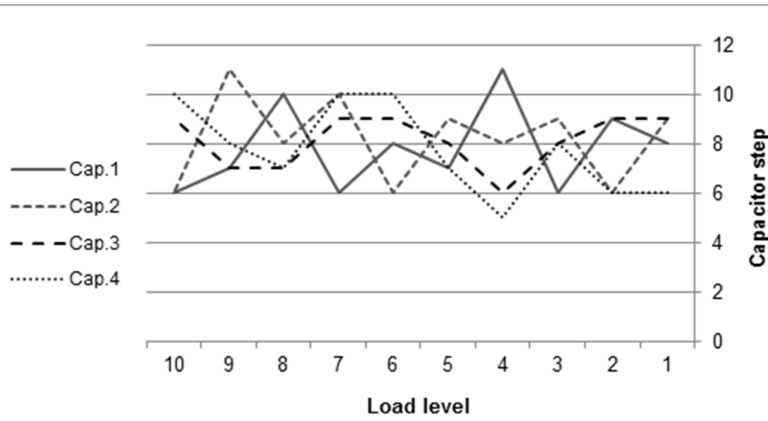


Fig. 6. Placement of four capacitors

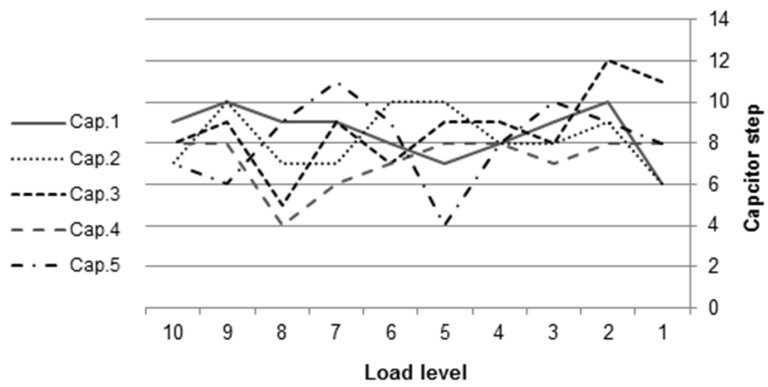


Fig. 7. Placement of five capacitors

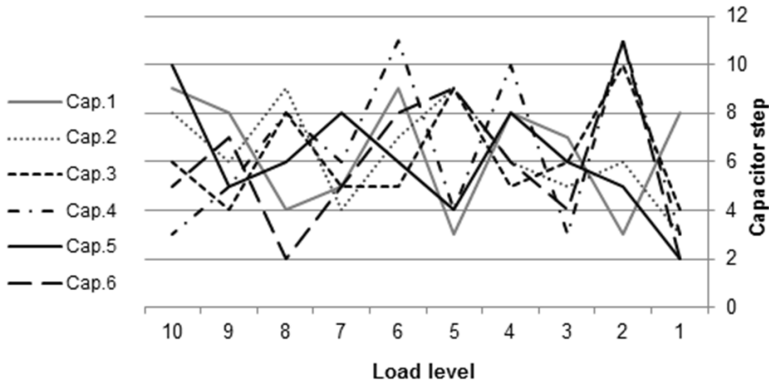


Fig. 8. Placement of six capacitors

## 6. Conclusion

In this paper, the raising reliability and reducing power loss of power distribution network by determining optimal location and size of capacitor banks was performed by the GSO algorithm.

By using the simulations, we can conclude that:

- The best case is placing four capacitor banks.
- The worst case is the installation of six capacitor banks on a bus.
- Most of the changes in the capacitor banks are observed at the worst output state.
- The number of banks has a direct impact on the network.
- An increase in the number of capacitor banks, in spite of reducing the capacity and cost associated with it, is not economically feasible.

## References

- [1] J. P. CHIOU, C. F. CHANG: *Development of a novel algorithm for optimal capacitor placement in distribution systems.*, *Electrical Power and Energy Systems* 73 (2015), 684–690.
- [2] R. A. HOOSHMAND, M. ATAIEI: *Optimal capacitor placement in actual configuration and operational conditions of distribution systems using RCGA.* *Journal of Electrical Engineering* 58 (2007), No. 4, 189–199.
- [3] M. R. HAGHIFAM, O. P. MALIK: *Genetic algorithm-based approach for fixed and switchable capacitors placement in distribution systems with uncertainty and time varying loads.* *IET Generation Transmission Distribution* 1 (2007), No. 2, 244–252.

- [4] A. SWARNKAR, N. GUPTA, K. R. NIAZI: *Optimal placement of fixed and switched shunt capacitors for large-scale distribution systems using genetic algorithms*. Proc. IEEE PES Innovative Smart Grid Technologies Conference Europe (ISGT Europe), 11–13 Oct. 2010, Gothenburg, Sweden, 1–8.
- [5] S. NEELIMA, P. S. SUBRAMANYAM: *Efficient optimal sizing and allocation of capacitors in radial distribution systems using Drdlf and differential evolution*. ACEEE International Journal on Electrical and Power Engineering 2 (2011), No. 3, 56–61.
- [6] H. KHANI, M. MOALLEM, S. SADRI, M. DOLATSHAHI: *A new method for online determination of the location of switched capacitor banks in distribution systems*. IEEE Transactions on Power Delivery 26 (2011), No. 1, 341–351.
- [7] K. HUR, S. SANTOSO: *On two fundamental signatures for determining the relative location of switched capacitor banks*. IEEE Transactions on Power Delivery 23 (2008), No. 2, 1105–1112.
- [8] M. M. SAIED: *Capacitor switching transients: analysis and proposed technique for identifying capacitor size and location*. IEEE Transactions on Power Delivery 19 (2004), No. 2, 759–765.
- [9] H. M. KHODR, Z. A. VALE, C. RAMOS: *Optimal cost-benefit for the location of capacitors in radial distribution systems*. IEEE Transactions on Power Delivery 24 (2009), No. 2, 787–797.
- [10] H. M. KHODR, F. G. OLSINA, P. M. DE OLIVEIRA-DE JESUS, J. M. YUSTA: *Maximum savings approach for location and sizing of capacitors in distribution systems*. Electric Power Systems Research 78 (2008), 1192–1203.
- [11] M. CHIS, M. M. A. SALAMA, S. JAYARAM: *Capacitor placement in distribution systems using heuristic search strategies*. IEE Proceedings - Generation, Transmission and Distribution 144 (1997), No. 3, 225–230.
- [12] J. C. CARLISLE, A. A. EL-KEIB: *A graph search algorithm for optimal placement of fixed and switched capacitors on radial distribution systems*. IEEE Transactions on Power Delivery 15 (2000), No. 1, 423–428.
- [13] S. SEGURA, R. ROMERO, M. J. RIDER: *Efficient heuristic algorithm used for optimal capacitor placement in distribution systems*. Electrical Power and Energy Systems 32 (2010), 71–78.
- [14] C. T. SU, C. C. TSAI: *A new fuzzy-reasoning approach to optimum capacitor allocation for primary distribution systems*. Proc. The IEEE International Conference on Industrial Technology (ICIT '96), 2–6 Dec. 1996, Shanghai, China, 237–341.
- [15] R. A. JABR: *Optimal placement of capacitors in a radial network using conic and mixed integer linear programming*. Electric Power Systems Research 78 (2008), 941–948.
- [16] A. PREGELJ, M. BEGOVIC, A. ROHATGI: *Recloser allocation for improved reliability of dg-enhanced distribution networks*. IEEE Transactions on Power Systems 21 (2006), No. 3, 1442–1449.
- [17] X. YAN, W. YANG, H. SHI: *A group search optimization based on improved small world and its application on neural network training in ammonia synthesis*. Neurocomputing, 97 (2012), 94–107.
- [18] S. HE, Q. H. WU, J. R. SAUNDERS: *An optimization algorithm inspired by animal searching behavior*. IEEE Transactions on Evolutionary Computation 13 (2009), No. 5, 973–990.

Received December 18, 2017



# Numerical investigation of the effect of nanoparticles on thermal efficiency of phase change materials

MOHSEN IRANI<sup>1,2</sup>, FARAMARZ SARHADDI<sup>1</sup>, AMIN BEHZADMEHR<sup>1</sup>

**Abstract.** In this study, in order to examine the thermal properties of different materials, the effect of different nanoparticles (Np) in phase change materials on the heat transfer rate in the melting and freezing processes of these materials has been numerically investigated. In the present study, carbon nanotubes and aluminum oxide as an enhancement nanoparticle as well as paraffin and a combination of hydrated salts as a phase-change material have been used. The finite difference method is used based on the enthalpy method for the phase change problem for numerical solution. The simulation results indicate an increase in the heat transfer rate due to the addition of nanoparticles to the phase change material. For both of the phase change materials considered in the present study, the results show the higher efficiency of carbon nanotubes compared to aluminum oxide to increase the heat transfer rate. The highest increase compared to the base state at the speed of the processes involved the addition of carbon nanotubes to paraffin, which according to the simulation is about 30%. The lowest increase is related to the state of aluminum oxide in the composition of hydrated salts (about 4.5%). The results of this study can be used to determine the heat transfer speed required for storing and releasing energy.

**Key words.** Energy storage, phase change material, nanoparticles, carbon nanotubes, enthalpy method, melting, freezing.

## 1. Introduction

Today, with increased demand for energy and reduction of fossil fuels, as well as the polluting and expensiveness of these fuels, the need for renewable energies has been felt more and more and this concerned researchers to this type of energy such as sun, geothermal energy, wind energy, and so on. In general, renewable energies need to be restrained, stored, and released in accordance with the need. In fact, materials can be used to store this low-energy depending on the need and at high speeds to

---

<sup>1</sup>Department of Mechanical Engineering, University of Sistan and Baluchestan, Zahedan, Iran

<sup>2</sup>Corresponding author; e-mail: [Mohsen.irani91@yahoo.com](mailto:Mohsen.irani91@yahoo.com)

prevent the loss of energy. One of the ways to increase the storage and release speed is to increase the thermal conductivity of materials that are stored and released in the process of energy storage and release, and due to the high thermal conductivity found in nanoparticles, and in particular carbon nanotubes, these materials is one of the best options.

In 2005, Pirkandi et al. [1] examined the process of phase change in a phase-change material in an energy storage device with two co-axial pipes. They used enthalpy method for the melting and freezing process in their work.

In 2018, Aldalbahi et al. [2], explored a variety of energy storage technologies based on phase-change materials and the use of nanotechnology. In 2011, Sebti et al. [3] investigated the numerical work of the heat transfer process during freezing inside two annular central cylinders by adding nanoparticles. With addition of nanoparticles, an increase in the rate of heat transfer was observed. In their work, they used finite volume method through enthalpy technique to find the boundaries of solid and liquid phases. Copper oxide was also used as a nanoparticle. In 2015, Mondragón et al. [4] investigated the numerical process of heat transfer in a cryogenic energy storage system. In 2014, Sharmat et al. [5] studied the process of freezing of nano-fluid containing water and copper oxide numerically. The effect of different volume fractions and temperature difference between two cold and hot walls in the freezing process was investigated and it was observed that the increase of nanoparticle volume fraction had the most effect on increasing the heat transfer.

Most studies have used copper oxide or other spherical nanoparticles. For this reason, we decided to examine the effect of carbon nanotubes and compare them with the results of other nanoparticles. In this study, the numerical study of the effect of nanoparticles to phase-change material on the speed of the melting and freezing process has been investigated, and a comparison has been made between different nanoparticles. The purpose of this study was to investigate the effect of nanoparticles on the efficiency of phase-change materials using enthalpy method for phase change process.

## 2. Problem geometry

The geometric model of the problem, as shown in Fig.1 consists of a layer containing a phase change material with dimensions of  $73 \times 5.2$  cm and two adjacent channels in which the air flows. On the right side of the air flows from the bottom to up, but on the left side the air is constant. In both channels, heat transfer is provided free of charge. Open channel dimensions are  $73 \times 5$  centimeters. The air in the left side has a constant temperature, which, at the time of the freezing and melting process, has a value of 0 and  $30^\circ\text{C}$ , respectively. The available air on the right side of the layer containing the phase change material at a temperature of  $20^\circ\text{C}$  entered the canal and is affected by the heat transfer process of the free movement in the channel and its temperature rises. Also, in the process of melting the constant thermal flux,  $200\text{ W/m}^2$ , from the left to the layer containing the phase change material is applied, and in the freezing process, the constant thermal flux  $-200\text{ W/m}^2$  is applied to the layer from the left.

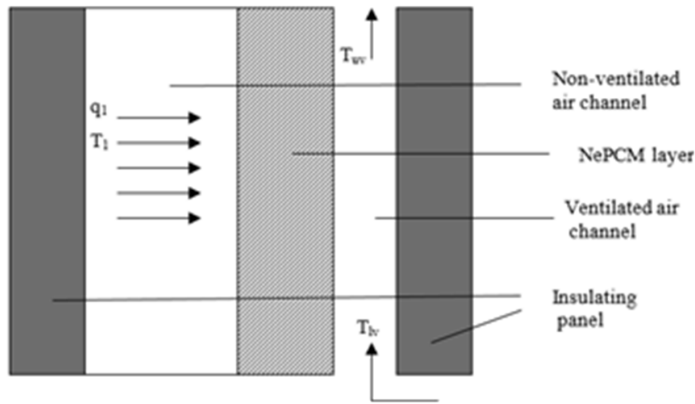


Fig. 1. Geometric model of the problem

In this study, the desired fluid was air, and among the phase change material, a combination of hydrated salts (water + calcium chloride ( $2CaCl$ ) + potassium chloride ( $KCl$ ) + other added substances) and paraffin as a phase change material were selected. among the various types of paraffin, Nano-Ocodacane was used for application and the properties are listed in the following Table 1. There were many options to choose for a nanoparticle in phase change material, among carbon nanotubes with regard to their unique properties we used. Aluminum oxide nanoparticles were also used to compare the results.

Table 1. Thermophysical properties of paraffin and carbon nanotubes

Material	Parameters				
	Density ( $kg/m^3$ ) (Solid/Liquid)	Specific heat capacity ( $J/(kg K)$ ) (Solid/Liquid)	Thermal conductivity ( $W/(m K)$ ) (Solid/Liquid)	Phase change temperature ( $^{\circ}C$ )	Latent heat ( $kJ/kg$ )
Paraffin ( <i>n</i> -octadecane)	(770/685)	(2196/1934)	(0.148/0.358)	27	243
Carbon nanotube	1350	600	K	-	-
Aluminum oxide	3600	765	36	-	-
Mixture of hydrates	1070	(2207/1832)	(0.58/0.82)	27	184.276

The prediction of thermophysical properties enhanced phase material in both solid and liquid phases depend on the phase change material and the volume fraction of the nanoparticles, is made to vary the density, specific heat capacity, and the latent heat of the theory combination has been used. The density  $\rho_{eff}$  of enhanced phase

material is given below:

$$\rho_{\text{eff}} = (1 - \Phi_{\text{vol}})\rho_{\text{PCM}} + \Phi_{\text{vol}}\rho_{\text{NP}}. \quad (1)$$

In this equation,  $\Phi_{\text{vol}}$  represents the volume fraction of nanoparticles,  $\rho_{\text{NP}}$  is their specific mass and  $\rho_{\text{PCM}}$  denotes the specific mass of phase-change material. The specific heat capacity of enhanced phase material is as follows:

$$(\rho C_p)_{\text{eff}} = (1 - \Phi_{\text{vol}})(\rho C_p)_{\text{PCM}} + \Phi_{\text{vol}}(\rho C_p)_{\text{NP}}, \quad (2)$$

where  $\rho C_p$  denotes the specific heat.

According to the assumptions, nanoparticles are not in latent heat, the effective latent heat  $L$  of enhanced phase material is obtained as follows:

$$(\rho L)_{\text{eff}} = (1 - \Phi_{\text{vol}})(\rho L)_{\text{PCM}}. \quad (3)$$

In order to predict the thermal conductivity enhanced phase material, the NANO model has been used for solid phase in the form

$$\frac{K_{\text{eff}}}{K_b} = \frac{3 + \Phi(B_x + B_z)}{3\Phi B_x}. \quad (4)$$

This model was modified by considering the effective length parameter by Sang et al. In the present work, the effective length is considered an average of one. It is defined as follows

$$\frac{K_{\text{eff}}}{K_b} = \frac{\frac{K_{p,m}}{K_b} + \alpha - \alpha\Phi_N \left[1 - \frac{K_{p,m}}{K_b}\right]}{\frac{K_{p,m}}{K_b} + \alpha + \alpha\Phi_N \left[1 - \frac{K_{p,m}}{K_b}\right]}. \quad (5)$$

In the above equations,  $K$  denotes the thermal conductivity,  $C_p$  denotes the specific heat,  $H$  denotes the enthalpy,  $Q_1$  represents the input energy to the energy storage layer,  $T$  is the temperature,

For the present study, the value  $2.1 \times 10^{-9} \text{ m}^2\text{K/W}$ , which has a great degree of magnitude compared to experimental work, is considered to be thermal resistance. Another nano-particle is aluminum oxide, which is a spherical nanoparticle. Apart from effective thermal conductivity, other thermo-physical properties of enhanced phase change material by this nanoparticle is the same as the status used by carbon nanotubes. In order to calculate the thermal conductivity of enhanced phase change material, the following equation is used:

$$k_{n-\text{pcm}} = \frac{k_{\text{np}} + 2k_{\text{pcm}} - 2(k_{\text{pcm}} - k_{\text{np}})\Phi_{\text{np}}}{k_{\text{np}} + 2k_{\text{pcm}} + (k_{\text{pcm}} - k_{\text{np}})\Phi_{\text{np}}} k_{\text{pcm}} + \beta k_1 \rho_{\text{pcm}} C_{p,\text{pcm}} \sqrt{\frac{KT}{\rho_{\text{np}} d_{\text{np}}}} f(T, \Phi_{\text{np}}). \quad (6)$$

The first part of this equation indicates the Maxwell model, and the second

part indicates Brownian motion, which indicates thermal dependence for effective thermal conductivity. Also, for calculating the conductivity of carbon nanotubes, the equation below has been used:

$$k = [3.7 \times 10^{-7}T + 9.7 \times 10^{-10}T^2 + 9.3 \left(1 + \frac{0.5}{L_{CNT}}\right) T^{-2}]^{-1}. \quad (7)$$

The parameters used in equation of thermal conductivity are listed in Table 2.

Table 2. Parameters used in the equations of thermal conductivity

Parameter	Value	Unit
$d_{np,Al_2O_3}, d_{np,CNT}, L_{np,CNT}$	$59 \times 10^{-9}, 1.7 \times 10^{-9}, 5 \times 10^{-6}$	m
$C_{1np,Al_2O_3}, C_{2np,Al_2O_3}, c_1$	$0.9830, 12.959, -3.91123 \times 10^{-3}$	-
$c_2, c_3, c_4$	$28.217 \times 10^{-3}, 3.917 \times 10^{-3}, -30.699 \times 10^{-3}$	-
$S_{1np,Al_2O_3}, S_{2np,Al_2O_3}$	$8.4407, -1.07304$	-
$T_{ref}$	298.15	$k$
$K$	$1.381 \times 10^{-23}$	J/K
$k_1$	$5 \times 10^4$	-

### 3. Results and discussion

A numerical simulation was performed for the conditions mentioned in the previous sections for storing and releasing energy. In the next step, the effect of adding different nanoparticles to phase change materials will be studied and compared at the speed of melting and freezing processes. The speed of melting and freezing processes for aluminum oxide nanoparticles and carbon nanotubes—enhanced phase change material (paraffin) with a volume fraction of 5 % has been investigated. The calculation of the melting and freezing process for paraffin and various nanoparticles is shown in Figs. 2 and 3.

Increasing the heat transfer rate due to the addition of nanoparticles due to the high thermal conductivity and thus the acceleration of the melting and freezing processes is predictable, which can be seen in Figs. 3 and 4. It should be noted, that the process of melting of aluminum oxide nanoparticles and carbon nanotubes—enhanced phase change material (paraffin) experienced an increase of 30 % and 16 % at execution. The values for the freezing process of this material are 14.5 % and 5.5 %. By doing the same for the other phase change material (a combination of hydrated salts), the results were similar to those given for paraffin. These results are shown in Figs 5 and 6, which are related to the melting and freezing processes.

In this study, for drawing the diagram of the duration of the melting and freezing processes, the time for these processes to be considered for the longest time, and the rest of the time is proportional to it. In Fig. 6, in order to sum up the contents, the rate of melting and freezing processes for all the materials is presented for comparison.

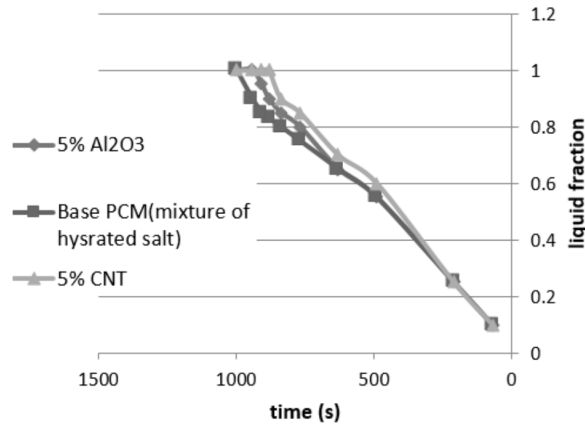


Fig. 2. Melting process of aluminum oxide nanoparticles and carbon nanotubes—enhanced phase change material (paraffin)

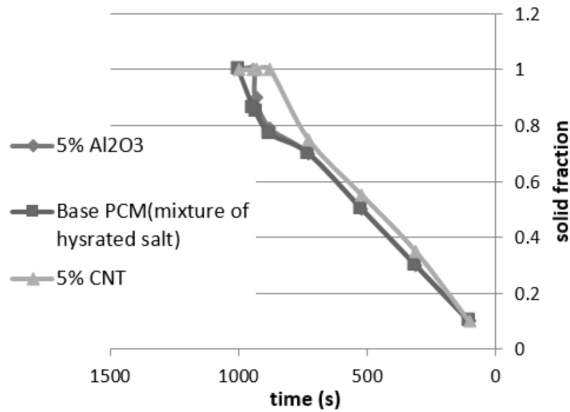


Fig. 3. Freezing process of aluminum oxide nanoparticles and carbon nanotubes—enhanced phase change material (paraffin)

As shown in Fig. 6, the greatest increase in the speed of the processes is related to the state of the carbon nanotubes added to paraffin. There are two main reasons for this. The first reason is that the thermal conductivity of paraffin as a base phase material is very low about  $0.15 \text{ W/mK}$ . The second reason is the high thermal conductivity of nanotube carbon fiber, about  $3000 \text{ W/mK}$ . Also, according to the results, the least increase in the speed of the processes in relation to the base state is the one used to combine aluminum oxide with hydrated salts.

#### 4. Conclusion

In the present study, a numerical study was carried out to estimate the effect of increasing the thermal conductivity through the addition of carbon nanotubes and

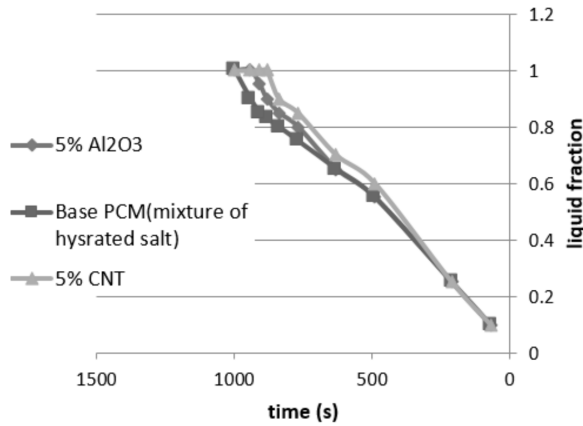


Fig. 4. Melting process of aluminum oxide nanoparticles and carbon nanotubes—enhanced phase change material (hydrate salts composition)

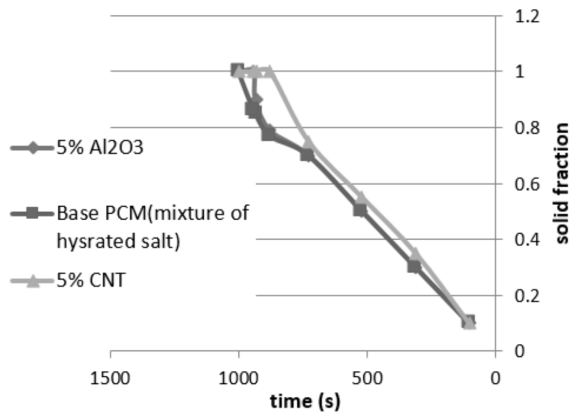


Fig. 5. Freezing process of aluminum oxide nanoparticles and carbon nanotubes—enhanced phase change material (hydrate salts composition)

aluminum oxide to various phase change materials on the thermal efficiency of the resulting material. Based on the present study, it can be noted that the thermal performance of the phase change material is enhanced by the addition of aluminum oxide nanoparticles and carbon nanotubes to these materials and, in fact, the heat transfer rate is controllable. For both nano particles, the thermal efficiency of the phase change material is better than the base state, but the use of carbon nanotubes results in better results than aluminum oxide. Generally, the use of nanoparticles increases the speed of melting and freezing processes. Of course, it is unlikely that the use of nanoparticles is now economically justifiable for energy storage processes that have so far been low.

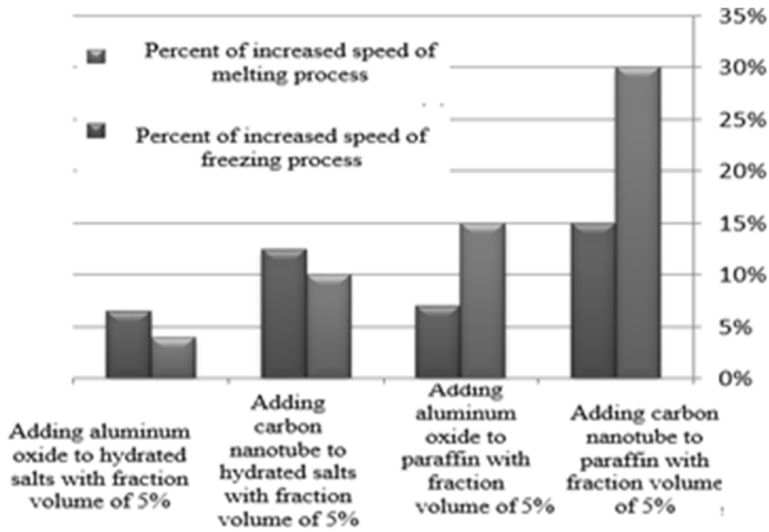


Fig. 6. Effect of adding nanoparticles too phase change materials on increasing the speed of melting and freezing processes thab base- phase change materials

## References

- [1] A. V. ARASU, A. P. SASMITO, A. S. MUJUMDAR: *Thermal performance enhancement of paraffin wax with  $Al_2O_3$  and  $CuO$  nanoparticles - a numerical study*. *Frontiers in Heat and Mass Transfer (FHMT)* (2011), No. 2, paper 043005.
- [2] A. ALDALBAHI, R. MOSTAFIZUR, M. ALMOIGLI, A. MERIEY, N. ALHARBI: *Improvement in electrode performance of novel SWCNT loaded three-dimensional porous RVC composite electrodes by electrochemical deposition method*. *Nanomaterials* 8 (2018), No. 1, 19.
- [3] J. HONE: *Carbon nanotubes: Thermal properties*. Dekker Encyclopedia of Nanoscience and Nanotechnology. Marcel Dekker, Inc., New York, USA (2004) 603–610.
- [4] R. MONDRAGÓN, R. MARTÍNEZ-CUENCA, L. HERNÁNDEZ, P. CABEDO, J. JULIÁ: *Handbook of clean energy systems*, John Wiley & Sons, Ltd., 2015.
- [5] K. PEIPPO, P. KAURANEN, P. D. LUND: *A multicomponent PCM wall optimized for passive solar heating*. *Energy and Buildings* 17 (1991), No. 4, 259–270.

Received May 7, 2017

# A method of reducing the interference of signals in MIMO technology

RAMIN SAYADI<sup>1,3</sup>, SAJAD NOSRATIAN<sup>2</sup>, ANITA HATAMIAN<sup>2</sup>

**Abstract.** To increase the operating power of a radio Link, multiple antenna are placed in both transceiver parts. This system is called multiple Input multiple output or MIMO. The point of signals interference is one of the important challenges in use of MIMO technology which in this article, was addressing to solve the problem of interference of these signals in MIMO tech through Beam forming clear and Decoding place in transceiver (sender & receiver) and eventually compare the results of both methods. The results of research showed that the mentioned decoding method leads to very much reduction in signal interference in MIMO tech. In addition to applying of this method with incorporation of more band width, obviate most of these interference problems somewhat. In this article, the method of beam forming clear Leads to decrease of signals interference in amount of 48%. The method of decoding place in transceiver leads to Decrease of signals interference in amount of 63% and the combined method of increase and decoding place in transceiver leads to decrease of signals interference in amount of 67%.

**Key words.** MIMO tech, interference, receiver, decoding place method.

## 1. Introduction

The phenomenon of signals interference is one of the major problems in wireless communications network. So it create several technology for decrease the effects of signals interference in these networks. The phenomenon of signals interference has negative effect on MIMO tech function and in some cases Lead to cancelling the sending information from transmitter to receiver. So several methods have designed and introduced for decrease interference of these signals including: Beam forming and decoding place in transceiver. Actually the beam forming is a radio signal transferring method. The function of beam forming in decreasing the signals

---

<sup>1</sup>Faculty of Islamic Azad University, Ilam, Electrical Field, and Telecommunication Trends College, Ilam, Iran

<sup>2</sup>Student of Electrical Engineering, Telecommunication Trends, Islamic Azad University, Arak, Iran

<sup>3</sup>Corresponding author; e-mail: sayadi@ilam-iau.ac.ir

interference in MIMO tech is like this, actually you control the output specifications of every antenna in during data transmission. The decoding place method is like this, areas that in them, the signals interference in MIMO tech, have most density, are identified [1]. To ensure the prevention from interference signals in MIMO tech, between the sender & receiver, Electronic equipment should be on both end of a physical medium, & this equipment need to a circuit to measure the time of sending and receiving the signals to prevent of interference of them, through time tuning [2]. Some of the flows of Beam forming clear method are SD waves deviation to up and down, late arrival of waves to receiver and being complicated process for simple receiver and some of flaws of linear coding methods are need to be carefully and sync of transmitter with receiver and Dispersion of waves in different directions that some of them are unwanted [3].

To describe the method that is used for prevention of signals interference, a series of signals are coded that is called linear coding [4]. We use the term of compression to Hint the method that decreases number of necessary signals in every second for prevention of signals interference in MIMO tech in appropriate level. In this case, two kinds of compression is introduced: With deleting signals some of signals are last during compression a without deleting signals—all signals remain in compressed version [5–7]. Compression without signals deletion keeps primitive data without any change [8].

In this article, a method based on combined of two above methods is presented, to decrease signals interference in MIMO tech. in the first part (introduction) an overview about signals interference in MIMO tech and selected methods separately, research theoretical, applying of Linear coding, Manchester coding, Differential Manchester coding, compression and coding methods for decrease signals interference in MIMO tech has described, while the kinds of beam forming methods & phenomenon of “variety” is describe too. The second’s part (suggested method) is about the description and explanation of the suggested method in this article. At third & fourth part, respectively, the suggested and combined methods are implemented, and at the last part, the results are raised.

## 2. Suggested method

In this article the decoding place method in transmitter and receiver compared with clear beam forming, to decrease the signals interference in MIMO tech is evaluated and then, it has combined with network bandwidth method. In use of beam forming method, at first several transmitter and receiver are considered in the same technology and the signals are send from transmitter to receivers through MIMO tech. the number of areas that signal interference happen in them and percent of their interference is reviewed. Then the same test with same signals through beam forming is repeated and again the number of areas that signals interference happen in them and percent of these interference is computed. Every interference area was assigned a code based of interference area space with transmitter and receiver. With encoding the mentioned areas, the amount of interference of these signals is decreased. The results of both methods are compared and in the following to recov-

ery the given results, the method that has most decrease in signals interference, is combined with network bandwidth method.

The objective function is

$$F = Ax + Bt + Cy, \quad (1)$$

where  $x$  is the percent of signals interference,  $t$  is the time of interference (seconds) and  $y$  is the place of interference (space from the transmitter to meter).  $F$  is also the measure of created interference in signals in MIMO tech.  $A$ ,  $B$  and  $C$  are constants that are obtained through try and error tests and, therefore, in some of references, including [7], these amounts are equal more amounts of  $x$ ,  $t$  and  $y$ . The effective parameter of designing are listed in Table 1.

Table 1. Effective parameters on designing

Parameter	Row
Time ( $t$ )	1
Percent of interference ( $x$ )	2
Place of interference ( $y$ )	3
Number of transmitter	4
Number of receiver	5
Kind of modulation	6

### 3. Results

#### *3.1. Implementation of beam forming and place decoding method in transceiver to decrease the signals interference in MIMO tech*

Implementation of beam forming method at first seven transmitters and receivers (overall 14 transceivers) is applied in mobile tech and signals through MIMO tech from transmitter to receiver, with discrete shifts modulation in frequency (FKS) are sended. To each area of signal interference is assigned a name. The number of areas and the time of the signal interference that happen there, is presented in Table 2.

According to the Table 2 the interference has created in 5 areas that most of these interferences in maximum a day after sending signal from transmitter to receiver, for the first time has created and the peak of them is about 8 to 9 am, 5 to 7 pm and 10 to 12 in the night. The intensity of each one of these interference has computed and presented in Table 3.

According to the Table 3, the areas that the amount of interference in them is more than 50%, are critical areas and they negatively effects on used MIMO tech function and surely it should take actions to remove or decrease these interferences. To decrease these interferences, the clear beam forming method is applied. In this case, the communication between the transmitter and receiver get stronger and the interferences are decreased. In this case also, the number of areas and the time that

signals interference happen in them are defined and the result of them has presented in Table 4.

Table 2. Number of areas and the time of signals interference in MIMO tech before applying of clear beam

The time of interference in a day	The time of interference	Name of signal interference area
Between 8 to 9 am	4 hours after sending signal from transmitter	A1
Between 5 to 7 pm	6 hours after sending signal from transmitter	A2
Between 5 to 7 pm	A day after sending signal from transmitter	A3
Between 10 to 12pm	A day after sending signal from transmitter	A4
Between 10 to 12pm	A day after sending signal from transmitter	A

Table 3. Name and percent of each one of interferences in MIMO tech before of applying the clear forming

The percent of created interference	The name of signal interference
32 %	A1
57 %	A2
61 %	A3
60 %	A4
85 %	A5

Table 4. The number of areas and the time of signal interference in MIMO tech after applying the clear beam

The time of interference in day	Time of interference	The name of signal interference
Between 5 to 7 pm	6 hours after sending the signal from transmitter	A2
Between 5 to 7 pm	One day after sending the signal from transmitter	A3
Between 10 to 12 night	One day after sending the signal from transmitter	A4
Between 10 to 12 night	One day after sending the signal from transmitter	A5

According to the Table 4, with applying the clear beam forming method, the number of interference areas decreased from five areas to four areas. These interference in maximum a day after sending signals from transmitter to receiver, for the first time has been created and the peak of them is at 5 to 7 pm and 10 to 12 night and the signals interference removed at 8 to 9 am. The percent (intensity) of each one of these interferences, computed again and it has presented in Table 5.

Table 6. Name and percent of each one of created interferences in MIMO tech after applying the clear beam forming

The percent of created interference	The name of signal interference
39 %	A2
45 %	A3
40 %	A4
49 %	A5

According to Table 5, with applying the clear beam forming method, the intensity of all the signals interference in MIMO tech, decreased under 50 % and all the interference areas became UN critical. The used MIMO tech function recovered and with applying the clear beam forming, overall 65 % of signals interference decreased. Implementing the place decoding method is also in this case, transceiver Like the clear beam forming method, apply seven transmitter and receiver (overall 14 transceiver) in mobile tech, and signal through MIMO tech from transmitter to receivers, with discrete shifts modulation in frequency (FKS), are send. Each area of signals interference are assigned a name. the number of areas and the time that signals interference happens in them, has presented in table (2) that according to this table, the signals interference has created in 5 areas which these interferences in maximum a day after sending the signals from transmitter to receiver, for the first time has created and peak of them is at 8 to 9 am, 5 to 7 pm and 10 to 12 night the percent (intensity) of each one of these interferences computed and it presented in table (3). In this case also the number of areas and the time that signals interference happen in them, are defined and the result of them has presented in following Table 6.

Table 6. The number of areas and the time of signals interference in MIMO tech after applying place decoding in transceiver

The time of interference in day	Time of interference	The name of signal interference
Between 5 to 7 pm	a day after sending the signal from transmitter	A3: 38 %
Between 10 to 12 night	a day after sending the signal from transmitter	A4: 25 %
Between 10 to 12 night	a day after sending the signal from transmitter	A5: 22 %

According to Table 6, with applying the place decoding method in transceiver, the number of interference areas decrease from 5 areas to 3 areas. These interferences in maximum a day after sending the signals from transmitter to receiver, for the first time has created and the peak of them is at 5 to 7 pm and 10 to 12 night and the signal interference at 8 to 9 am removed. The percent (intensity) of each one of these interferences, computed again and in has presented.

### ***3.2. Implementation of suggested method of the two selected methods to decrease the signals interference in MIMO tech***

The place decoding method in transceiver has more positive after on these interferences, in comparison to clear beam forming method. therefore, we combine this method with bandwidth and the result has presented in Fig. 1.

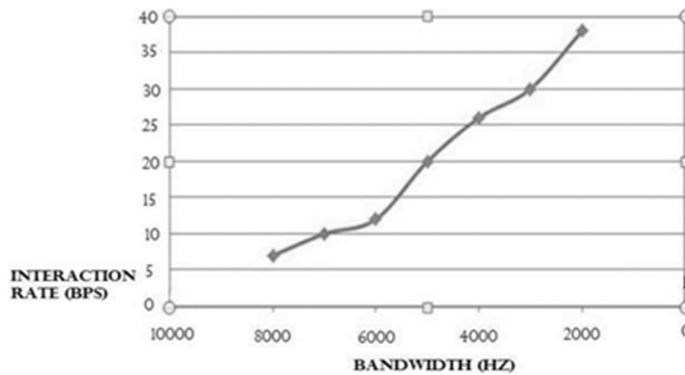


Fig. 1. Decreasing the signal interference in MIMO tech with combining the more band width method and place decoding in transceiver

According to Fig. 1, in combination the increasing band width method and place encoding method in transceiver, with increasing the band width, the signals interference in MIMO tech decreases and it can be said that this problem almost disappears because of that by increasing band width, the signals have more space for sending and receiving and so they have less conflict with each other. In the following the function of all three methods, the clear beam forming, place encoding in transceiver and the combination of more band width and place encoding in transceiver to decrease the signals interference in MIMO tech compares with each other. According to Fig. 2 all three methods of clear beam forming, place encoding in transceiver and the combination of more bandwidth and place encoding in transceiver, to decrease the signals interference in MIMO tech are effective methods. But among the three studied methods in this article, the clear beam forming method lead to decreasing the signals interference from 85 % to 37 %, the place encoding method in transceiver lead to decreasing the signals interference from 85 % to 18 %. So the mentioned combined method is the best method for decreasing the signals interference in MIMO tech.

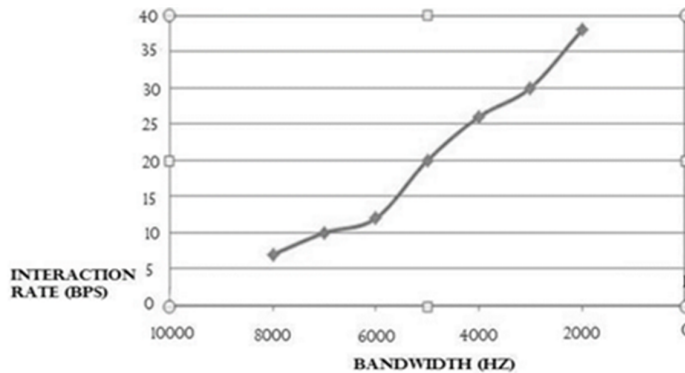


Fig. 2. The comparison of function of all three methods of beam forming, in MIMO tech

## 4. Conclusion

MIMO is a wave (Antenna) propagation tech for wireless telecommunication systems. MIMO tech by dramatic increase of data through put and distance of beneficial effect, it also needless to additional band width OD transmitter power, has a special place in wireless telecommunications. One of the basic problems in decreasing of MIMO tech function, is the signals interference that in this article, three scenario of clear beam forming, place encoding in transceiver and the combined method of more band width and place decoding in transceiver for decreasing the signals interference are suggested. All three methods of clear beam forming, place encoding in transceiver and the combines method of more band width and place encoding in transceiver for decreasing the signals interference in MIMO tech are the effective methods. But among three studied methods in this article, the clear beam forming method lead to decreasing the signals interference in amount of 48 %, the place encoding method in transceiver leas to decreasing the signals interference in amount of 63 % and the combined method of more bandwidth and place encoding in transceiver lead to decreasing the signals interference in amount of 67 %. So the mentioned combined method is the best method for decreasing the signals interference in MIMO tech. We can use clear beam forming method for decreasing the interference in available MIMO tech in small networks, that have less signal interference, combined method, can be used to solve the seven signal interference in MIMO tech. It is worth mentioning that increasing bandwidth in combined method has also flaws that as a challenge it can be checked in further studies.

## References

- [1] T. YOO, A. GOLDSMITH: *Capacity and power allocation for fading MIMO channels with channel estimation error*. IEEE Transactions on Information Theory 52 (2006), No. 5, 2203–2214.
- [2] D. GESBERT, M. SHAFI, D. S. SHIU, P. J. SMITH, A. NAGUIB: *From theory to prac-*

- tice: An overview of MIMO space-time coded wireless systems.* IEEE Journal on Selected Areas in Communications 21 (2003), No. 3, 281–302.
- [3] S. PLEVEL, T. JAVORNIK, G. KANDUS: *A recursive link adaptation algorithm for MIMO systems.* AEU - International Journal of Electronics and Communications 59 (2005), No. 1, 52–54.
  - [4] A. J. PAULRAJ, D. A. GORE, R. U. NABAR, H. BÖLCSKEI: *An overview of MIMO communications - a key to gigabit wireless.* Proceedings of the IEEE 92 (2004), No. 2, 198–218.
  - [5] A. B. GERSHMAN, N. D. SIDIROPOULUS: *Space-time processing for MIMO communications.* John Wiley & Sons Inc. (2015).
  - [6] G. J. FOSCHINI, M. J. GANS: *Layered space-time architecture for wireless communication in a fading environment when using multiple antennas.* Bell Labs Technical Journal 1 (1996), No. 2, 41–59.
  - [7] E. TELATAR: *Capacity of multi-antenna Gaussian channels.* Transactions on Emerging Telecommunications Technologies 10 (2008), No. 6, 585–596.
  - [8] M. SALEHIFAR, T. NANJUNDASWAMY, K. ROSE: *On scalable coding of hidden Markov sources.* IEEE International Conference on Acoustics, Speech and Signal Processing (ICASSP), 20–25 March 2016, Shanghai, China, IEEE Conferences (2016), 4024–4028.
  - [9] R. W. HEATH, A. J. PAULRAJ: *Switching between diversity and multiplexing in MIMO systems.* IEEE Transactions on Communications 53 (2005), No. 6, 926–968.
  - [10] M. SALEHIFAR, T. NANJUNDASWAMY, K. ROSE: *Quantizer design for exploiting common information in layered coding.* IEEE International Conference on Acoustics, Speech and Signal Processing (ICASSP), 20–25 March 2016, Shanghai, China, IEEE Conferences (2016), 4463–4467.

Received January 20, 2018